



5-2018

Power System Frequency Measurement Based Data Analytics and Situational Awareness

Ling Wu

University of Tennessee, lwu24@vols.utk.edu

Recommended Citation

Wu, Ling, "Power System Frequency Measurement Based Data Analytics and Situational Awareness." PhD diss., University of Tennessee, 2018.

https://trace.tennessee.edu/utk_graddiss/4897

This Dissertation is brought to you for free and open access by the Graduate School at Trace: Tennessee Research and Creative Exchange. It has been accepted for inclusion in Doctoral Dissertations by an authorized administrator of Trace: Tennessee Research and Creative Exchange. For more information, please contact trace@utk.edu.

To the Graduate Council:

I am submitting herewith a dissertation written by Ling Wu entitled "Power System Frequency Measurement Based Data Analytics and Situational Awareness." I have examined the final electronic copy of this dissertation for form and content and recommend that it be accepted in partial fulfillment of the requirements for the degree of Doctor of Philosophy, with a major in Electrical Engineering.

Yilu Liu, Major Professor

We have read this dissertation and recommend its acceptance:

Lee D. Han, Fangxing Li, Hairong Qi

Accepted for the Council:

Dixie L. Thompson

Vice Provost and Dean of the Graduate School

(Original signatures are on file with official student records.)

Power System Frequency Measurement Based Data Analytics and Situational Awareness

A Dissertation Presented for the

Doctor of Philosophy

Degree

The University of Tennessee, Knoxville

Ling Wu

May 2018

Copyright © 2018 by Ling Wu

All rights reserved.

DEDICATED

To my husband, Dr. Xuan Zhang and my son, Vincent Y. Zhang
whose endless love inspires me in every part of my life;

To my mother, Wugui Li
whose unconditional support encourages me to believe in myself;

In loving memory of my father, Tingliang Wu
whose intelligence still runs in my veins.

ACKNOWLEDGEMENTS

First and foremost, I would like to express my sincere appreciations to my advisor, Dr. Yilu Liu for her patient instructions, support and constant encouragement in both my academic and personal life. She really cares about her students. I cannot be more lucky and grateful to have Dr. Yilu Liu as my advisor.

Next, I would like to express my gratitude to Dr. Fangxing Li, Dr. Hairong Qi, Dr. Lee D. Han and Dr. Airton Kohls for their serving as my doctoral committee. I greatly appreciate their precious time and comments into this dissertation.

Moreover, I am very thankful to all my colleagues for their invaluable friendship and suggestions to my research, Dr. Yong Liu, Dr. Dao Zhou, Dr. Lin Zhu, Dr. Wenpeng Yu, Dr. Zhuohong Pan, Dr. Shutang You, Dr. Micah Till, Dr. Hesen Liu, Dr. Wenxuan Yao, Dr. Jiecheng Zhao, Xuemeng Zhang, Yu Su, Weikang Wang, Abigail Till, Lakshmi Sundaresh. In addition, I would also like to thank staff members in the CURENT center and EECS department, Ms. Judy Evans, Ms. Samantha White, and Ms. Dana Bryson for their generous help in many ways.

Finally, I would like to express my deepest appreciations to my family for their endless love, support and encouragement no matter what happens.

ABSTRACT

This dissertation presents several measurement-based research from power system wide-area dynamics data analytics to real-time situational awareness application development. All the research are grounded on the power system phasor measurements provided by wide-area Frequency Monitoring Network (FNET/GridEye), which collects the Global Positioning System (GPS) signal synchronized power system phasor measurements at distribution networks. The synchronized frequency measurement at FNET/GridEye enables real-time monitoring of bulk power systems (BPSs) and allows the dynamics interpretation of power system disturbances. Research on both the dynamic and ambient frequency measurements are conducted in this dissertation.

The dynamics refer to the frequency measurement when the system is experiencing sudden contingencies. This dissertation focuses on two types of contingency: generation trip and oscillation and conducts both data analytics and corresponding real-time applications. Historical generation trip events in North America are analyzed in purpose to develop a frequency measurement based indicator of power systems low inertia events. Then the frequency response study is extended to bulk power systems worldwide to derive its association with system capacity size. As an essential parameter involved in the frequency response, the magnitude of the power imbalances is estimated based on multiple linear regression for improved accuracy. With respect to situational awareness, a real-time FNET/GridEye generation trip detection tool is developed for PMU use at power utilities and ISOs, which overcomes several challenges brought by different data situations.

Regarding the oscillation dynamics, statistical analysis is accomplished on power system inter-area oscillations demonstrating the yearly trend of low-frequency oscillations and the

association with system load. A novel real-time application is developed to detect power systems sustained oscillation in large area. The application would significantly facilitate the power grid situational awareness enhancement and system resiliency improvement.

Furthermore, an additional project is executed on the ambient frequency measurement at FNET/GridEye. This project discloses the correlation between power system frequency and the electric clock time drift. In practice, this technique serves to track the time drifts in traffic signal systems.

TABLE OF CONTENTS

CHAPTER 1	Low Inertia Indicator of Bulk Power Systems Using Event Based Rate of Frequency Drop	1
1.1	Introduction	1
1.2	Theoretical background	2
1.3	Event-based rate of frequency drop	4
1.3.1	ROCOF calculation	4
1.3.2	Data pre-processing	5
1.4	ROCOF analysis by interconnection	6
1.5	Methodology for low inertia detection	8
1.6	Implementation of real-time low inertia alerts	14
1.7	Low inertia events analysis	16
1.8	Conclusion	19
CHAPTER 2	Observations of the Inertial Frequency Response of Main Power Grids Worldwide	23
2.1	Introduction	23
2.2	Frequency response	24
2.3	Data processing on frequency response	26
2.4	Observation results	28
2.4.1	Results of grids in North America	28
2.4.2	Results of oversea grids	32

2.5 Conclusion	36
CHAPTER 3 Multiple Linear Regression Based Disturbance Magnitude Estimations for Bulk Power Systems	37
3.1 Introduction.....	37
3.2 FNET/GridEye generation trip detection.....	38
3.3 Multiple linear regression	40
3.4 Model establishment	42
3.5 Model validation	46
3.6 Conclusion	49
CHAPTER 4 Development of Real-time Event Detection Application Package for Electric Utilities	50
4.1 Introduction.....	50
4.2 Application package design	51
4.3 Application modules	52
4.4 Challenges of the application package.....	53
4.4.1 Difference between FDR and PMU measurements	53
4.4.2 Challenges and opportunities in industry implementations	54
4.5 Successful implementation Stories	59
4.5.1 Southern Company.....	59
4.5.2 PJM Interconnection	61
4.5.3 GEIRI North America.....	62
4.6 Conclusion	64

CHAPTER 5	Inter-area Oscillation Statistical Analysis Of The U.S. Eastern Interconnection	65
5.1	Introduction.....	65
5.2	FNET/GridEye-detected inter-area oscillations.....	66
5.3	Analysis of oscillation occurrence	67
5.3.1	Hourly occurrence.....	68
5.3.2	Monthly occurrence	71
5.4	Analysis of oscillation mode.....	72
5.5	Analysis of oscillation types	75
5.6	Conclusion	76
CHAPTER 6	FNET/GridEye Real-time Sustained Oscillation Detection	78
6.1	Introduction.....	78
6.2	Frequency-based sustained oscillation detection	78
6.3	Theoretical background	81
6.4	Sustained oscillation signature.....	83
6.5	Detection of sustained oscillation	86
6.7	Verification of sustained oscillation detection.....	92
6.8	Conclusion	94
CHAPTER 7	Electric Clocks Time Synchronization Based on Grid Frequency	95
7.1	Introduction.....	95
7.2	Electric clocks.....	95
7.3	Time drift caused by power frequency	98
7.3.1	Time drift calculation.....	98

7.3.2 Analysis on FDR measurements	99
7.4 Time drift verification.....	100
7.5 Experiments	104
7.5.1 Continuous time drift estimation	104
7.5.2 Comparison of different FDR input signal performances.....	107
7.5.3 Long-term performance	110
7.6 Conclusion	112
CHAPTER 8 Conclusions and Future Work.....	113
8.1 Conclusions.....	113
8.2 Future Work.....	114
List of References	116
Vita	127

LIST OF TABLES

Table 1-1. Coefficient (k) in equation 1-5 for different interconnections.	8
Table 1-2. List of identified low inertia events.	17
Table 2-1. Rate of frequency decline quartiles for grids in North America.	31
Table 2-2. Estimation on oversea grids.	35
Table 3-1. Analyzed system variables.	41
Table 3-2. Parameter estimates for EI.	43
Table 3-3. Fitting summary comparison for EI.	43
Table 3-4. Parameter estimates for WECC.	45
Table 3-5. Fitting summary comparison for WECC.	46
Table 3-6. Parameter estimates for EI.	48
Table 3-7. Parameter estimates for WECC.	49
Table 4-1. GEIRI North America testing results.	63
Table 5-1. Dominate frequency of inter-area oscillations in EI.	75
Table 6-1. Effective applications hosted by FNET/GridEye.	79

LIST OF FIGURES

Figure 1-1. Frequency dynamics responding to the loss of power supply in WECC.	4
Figure 1-2. Typical frequency measurements responding to a generation trip event.	5
Figure 1-3. Scatter plot of ROCOF vs. amount of power loss of four interconnections in North America and their fitting lines.	7
Figure 1-4. Scatter plot of log(ROCOF) vs. log(power loss percentage) of four interconnections in North America and the overall fitting line.	9
Figure 1-5. A scatter plot of ROCOF vs. the amount of power loss based on actual generation trip events in the EI.	9
Figure 1-6. Distribution of historical generation trip events standard ROCOF.	11
Figure 1-7. Amount of identified low inertia events using different thresholds.	12
Figure 1-8. Marked low inertia events on scatter plot of historical events.	13
Figure 1-9. FNET/GridEye real-time low inertia detection implementation.	14
Figure 1-10. FNET/GridEye low inertia alert (The content has been modified due to confidential information).	15
Figure 1-11. A snapshot of FNET/GridEye event report (The content has been modified due to confidential information).	16
Figure 1-12. Frequency measurements of low inertia events.	20
Figure 2-1. Frequency response to a generation trip in WECC.	26
Figure 2-2. Frequency measurement white noise and the solution.	27
Figure 2-3. Frequency response oscillation and the solution.	28

Figure 2-4. FDRs deployment in North America.	29
Figure 2-5. Rate of frequency change distribution analysis of grids in North America.	30
Figure 2-6. Rate of frequency decline for grids in North America.	32
Figure 2-7. FDR coverage worldwide.	33
Figure 2-8. Estimation of the median rate during inertial frequency response.	35
Figure 3-1. Typical frequency response to a generation trip event.	39
Figure 3-2. Comparison of estimate errors distribution in EI.	47
Figure 3-3. Comparison of estimate errors distribution in WECC.	48
Figure 4-1. Diagram of FNET/GridEye event detection application package.	51
Figure 4-2. Distributed event detection system.	56
Figure 4-3. Voltage angle difference during a transmission line trip event.	58
Figure 4-4. Voltage angle difference during a transmission line reclosing event.	58
Figure 4-5. openPDC three user-defined layers structure.	60
Figure 4-6. Example of a detected event in openPDC.	60
Figure 4-7. Data interface interacting with PMU database and event detection tool.	62
Figure 5-1. Hourly occurrence of oscillations in EI.	68
Figure 5-2. 2013 hourly EI oscillation occurrence curve and PJM load profile.	70
Figure 5-3. 2014 hourly EI oscillation occurrence curve and PJM load profile.	70
Figure 5-4. 2015 hourly EI oscillation occurrence curve and PJM load profile.	70
Figure 5-5. Monthly occurrence of oscillations in EI.	71
Figure 5-6. Dominate frequency of inter-area oscillations in EI.	73
Figure 5-7. Hourly 80 percentile dominate frequency in EI.	74
Figure 5-8. Dominate frequency distribution of EI.	74

Figure 5-9. Occurrences of EI oscillations in different types.	76
Figure 6-1. Frequency response to the unit trip.	84
Figure 6-2. Sustained oscillation predominant mode @ 0.2739 Hz.	85
Figure 6-3. Sustained oscillation predominant mode @ 0.2524 Hz.	85
Figure 6-4. Sustained oscillation predominant mode @ 0.2695 Hz.	86
Figure 6-5. Sustained oscillation detection criteria.	87
Figure 6-6. Envelope band of phase angle measurements.	88
Figure 6-7. Calculation of threshold based on statistics of angle envelope bandwidth.	89
Figure 6-8. PSD of a sustained oscillation example.	89
Figure 6-9. Flowchart of the sustained oscillation detection at FNET/GridEye.	90
Figure 6-10. De-trending frequency of a sustained oscillation.	91
Figure 6-11. Raw frequency measurements from all FDRs for the testing case.	93
Figure 6-12. Processed frequency of the testing sustained oscillation.	93
Figure 6-13. Periodogram analysis of the testing sustained oscillation.	94
Figure 7-1. Block diagram of the synchronous clock.	96
Figure 7-2. Small synchronous motor from microwave ovens.	97
Figure 7-3. Time drift analyzer implementation.	99
Figure 7-4. Time drift analyzer example.	100
Figure 7-5. Connection and communication schematic diagram.	101
Figure 7-6. Example of implementation of querying device internal clock.	102
Figure 7-7. Query result example.	103
Figure 7-8. Time drift comparison implementation.	104
Figure 7-9. Long-term time drift comparison tool.	105

Figure 7-10. Output of time drift comparison.....	106
Figure 7-11. Time drift estimations based on FDRs from different states in WECC.....	108
Figure 7-12. Time drift estimations based on FDRs in Oregon.....	108
Figure 7-13. Time drift estimation based on average frequency.	109
Figure 7-14. Screenshot of time drift analyzer.	110
Figure 7-15. 09/01-09/07, 2015 weekly time drift analysis.....	112

CHAPTER 1 LOW INERTIA INDICATOR OF BULK POWER SYSTEMS USING EVENT BASED RATE OF FREQUENCY DROP

1.1 Introduction

The reduction of power systems inertia due to a shift from conventional power stations to renewables presents a range of planning and operational challenges for the transmission system and balancing authority operators. For example, power system inertia is one of the critical attributes of the systems to ensure frequency stability against contingencies [1] [2]. According to the swing function, the rate of change of frequency (ROCOF) following a contingency is determined by the system inertia at the moment of disturbance and the size of the imbalance [3] [4].

System inertia depends on the amount of kinetic energy of the rotating masses connected to the network at the time of the contingency. The greater the rotating mass, the greater the time constant, and the less the frequency deviation for a given load-generation imbalance. Current renewable resources have less or even no inertia, which undermines systems' ability to maintain the energy balance between generation and demand [5]. For instance, references [6]-[8] analyzed different scenarios taking into account the gradual integration of wind energy. As wind energy penetration increases, frequency inertial response of the system declines.

The recent large-scale deployment of phasor measurement units (PMUs), which measure system phasors synchronized with Global Positioning System (GPS) signal, provides great insights into the dynamics of power systems. Several research projects have proposed to estimate the system inertia using PMU data. For example, reference [1] and [9] estimated the inertia in the British and Iranian power grids. Similar research has also been done in ERCOT [10] and WECC [11]. However, for a large power system, the frequency responses to a specific disturbance at

different locations vary according to wave propagation [12], and PMUs installed within a small region are limited to observe the dynamics overall. Since the PMUs are generally owned by individual utilities, lack of a platform that collects information from all utilities impedes the knowledge of the system inertia at interconnection scale.

In this background, a real-time low inertia alarming system is proposed and implemented on FNET/GridEye[17], a wide area monitoring system that collects the synchrophasor measurements from globally deployed sensors [13]-[16]. FNET/GridEye allows the real-time monitoring of system frequency at an interconnection scale without PMUs accessibility constraints [17]. It detects power systems contingencies in real-time and sends out instant notifications to system operators [18]. This project allows the clients to receive an alarm if the contingency is considered to happen under low inertia conditions. By implementing the approach in FNET/GridEye, operators and planners across the interconnection could be alerted of the system low inertia situations.

1.2 Theoretical background

Power system frequency changes with the balance between power supply and demand. It drops when the power supply becomes insufficient due to loss of large power generation, or a tie line that import real power. The frequency change following a disturbance depends on the system inertia and the size of the power loss as presented in equation 1-1 [7].

$$\frac{df}{dt} = \frac{\Delta P}{2H} \times f_0 + \frac{D}{2H} \times \Delta f \quad \text{Equation 1-1}$$

where D is the load damping of the power system, f_0 is the system frequency at the start time of the disturbance ($t=0$), Δf is the frequency change, and ΔP is the power change percentage of the

system load base (MVA). Assuming the damping of load to be negligible, equation 1-1 can be reduced as equation 1-2 [9].

$$\frac{df}{dt} = \frac{\Delta P}{2H} \times f_0 \quad \text{Equation 1-2}$$

Since f_0 is normally around its nominal value (60Hz or 50Hz depending on the specific system), the ROCOF is generally proportional to the power imbalance and inversely proportional to the system inertia. Therefore, it can be inferred that the system inertia is strongly associated with ROCOF and power imbalance. The same amount of generation loss causes faster frequency change for lower inertia circumstances. This project proposes to evaluate the inertia status and identifies the relatively low inertia situations using synchronous measurements. By implementing the real time low inertia evaluation in a WAMS, a low-inertia detection and alarming system can assist operators and planners to be aware of low inertia status.

If the system inertia doesn't change much, the ROCOF should keep proportional to the power imbalance with a small range of variations. Figure 1-1 displays the frequency dynamics following power losses of different magnitudes in the Western Electricity Coordinating Council (WECC). It gives a comparison between two disturbances with different amounts of power deficiency, but similar inertia status. In Figure 1-1, event (a) was caused by a loss of generation about 1,465 MW occurred at 14:48:20 UTC time on September 3rd, 2015. The phasor measurements during the inertia response show frequency decline from 59.995 Hz to 59.852 Hz within 3.8 seconds. Event (b) was caused by a trip of generator at 14:25:12 UTC time on September 5th, 2015 carrying 750 MW before the contingency. Before the primary control completely delivered, the frequency decreased from 59.982 Hz to 59.913 Hz within 4.1 seconds. For these two events, the ROCOF is predominantly proportional to the power imbalance with

small variations. According to equation 1-2, their inertia should be similar although the frequency responses differ in terms of speed and deviation.

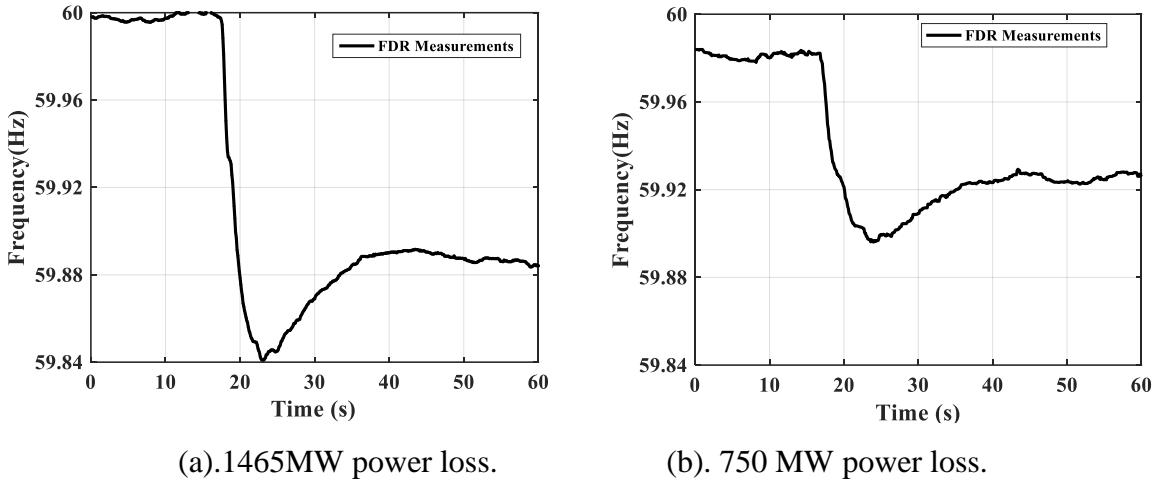


Figure 1-1. Frequency dynamics responding to the loss of power supply in WECC.

1.3 Event-based rate of frequency drop

1.3.1 ROCOF calculation

The inertial frequency response generally consists of a combination of immediate inertial response, primary frequency response, load response, and other slow responses. System frequency decays immediately following the onset of generation trip. The primary control would be activated within 1 or 2 seconds after, and fully delivered at the nadir within 12 to 14 seconds [10]. Typically the first 0.5 second of inertial frequency response can be considered to be purely contributed by the kinetic energy stored in rotating mass [19]. Therefore, in this project, the ROCOF is calculated according to the dynamics during the first 0.5 second as in equation 1-3, since no other responses are activated within this period.

$$ROCOF = 1000 * \frac{\Delta f_{0.5}}{0.5} \text{ (mHz/s)} \quad \text{Equation 1-3}$$

1.3.2 Data pre-processing

High time-resolution phasor measurements provide insight of dynamics, but it has to solve two major issues: white noise and oscillations. The white noise is unavoidable in real measurements. Typically, a low-pass filter can effectively reduce the noise [20]. The frequency deviation propagates throughout the entire interconnection due to the sudden generation trip. Some FDRs' measurements contain apparent oscillations, particularly during the initial frequency decline. The oscillation would distort the global frequency response. Most oscillations are recorded by FDRs near disturbance sources.

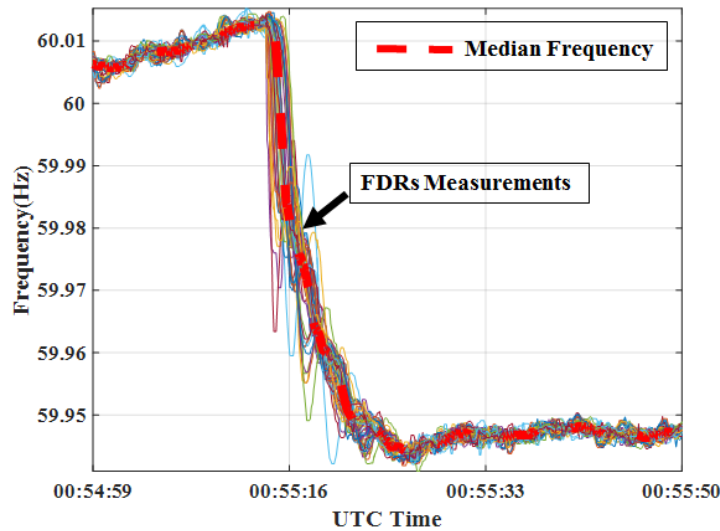


Figure 1-2. Typical frequency measurements responding to a generation trip event.

Figure 1-2 shows an example of the frequency dynamics of a generation trip disturbance happened in the Eastern Interconnection (EI). There are over 70 active FDRs installed and recording the dynamics in the EI [21]. All the measurements before and after the disturbance,

within one minute, are put together in this figure. It is difficult to label each measurement. In the frequency measurement plots hereinafter, the FDRs are displayed in various colors. In Figure 1-2, the colored curves are the raw measurements from FDRs, and the dashed curve is the median value. It can be seen that there are strong oscillations in some FDRs' measurement, which are usually near the event locations. However, the median frequency doesn't oscillate much during the inertial response. Therefore, ROCOF calculation in this project uses the median frequency of all FDRs measurements.

1.4 ROCOF analysis by interconnection

Due to different rotating masses in different interconnections, a ROCOF value may be acceptable in one interconnection but indicate low inertia in another. In this section, historical generation trip events happened in North America are analyzed and their ROCOFs are compared between different interconnections.

The four interconnections in North America operate asynchronously from each other. All of them are connected to at least one of the other via DC ties. The frequency is synchronous within each interconnection. According to the confirmed generation trip events list published by North American Electric Reliability Corporation (NERC) [22]. The ROCOF of a total of 881 generation trip events in North America from Jan 2012 to Feb. 2016 were calculated and displayed in Figure 1-3.

The lines in Figure 1-3 indicate the fitting results of ROCOF and the amount of power loss in different interconnections. They all present a positive correlation between ROCOF and the power loss amount, but with different slopes. The function of the fitted lines can be expressed as a proportional function as in equation 1-4, with its coefficient for each grid displayed in Table 1-1.

$$ROCOF = k * P_{loss}$$

Equation 1-4

According to the coefficient of each fitting line, it can be seen that for the same amount of power loss, the ROCOF value in a smaller power grid is higher than that in larger grids.

Different coefficients of fitting lines mainly due to system inertia difference. The fitting line with a greater slope indicates the same amount of power loss leads to faster frequency deviation.

According to the coefficients in Table 1-1, it is noticed that between the four interconnections, EI has the greatest inertia, followed by WECC, then ERCOT, QUEBEC in the end.

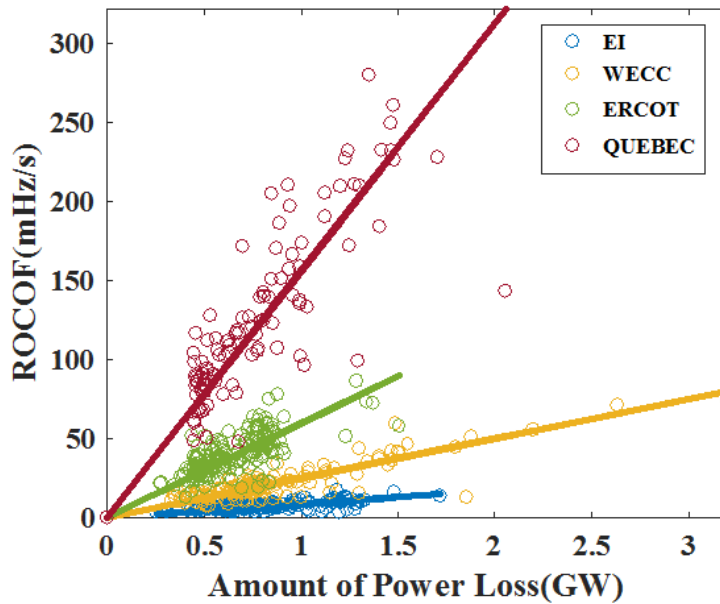


Figure 1-3. Scatter plot of ROCOF vs. amount of power loss of four interconnections in North America and their fitting lines.

The scatter plot of the same dataset in Figure 1-3 is replotted as in Figure 1-4. Scatter plot of $\log(\text{ROCOF})$ vs. $\log(\text{power loss percentage})$ of four interconnections in North America and the overall fitting line. Figure 1-4, where the horizontal axis is the natural logarithm of the

percentage of power loss over total capacity ($\log(\Delta P/P_{total})$) of the power grid. The vertical axis is the natural logarithm of the ROCOF value ($\log(ROCOF)$).

Table 1-1. Coefficient (k) in equation 1-5 for different interconnections.

Interconnection	Coefficient
EI	8.721
WECC	25.04
ERCOT	59.74
QUEBEC	156.1

It is noticed from Figure 1-4 that the events from four interconnections can be fitted by one straight line. It indicates that the frequency deviates at a similar speed when the same percentage of power generation is tripped in different interconnections. In Figure 1-4, the inertia constant fails to distinguish the generation trip events happened in different interconnections. In other words, the influences of the same amount of generation loss in different interconnections primarily depend on the percentage of capacity loss.

1.5 Methodology for low inertia detection

From the analysis above, it can be noticed that ROCOF is generally proportional to the size of power imbalance, and inversely proportional to the system inertia. These two factors directly influence the frequency change after the disturbance. Since low inertia event is of top concern of operators and planners, an approach is proposed to flag system low inertia events according to Figure 1-5, which depicts the scatter plot of ROCOF vs. the amount of power loss based on actual generation trip events that happened in the EI from 2012 to 2016.

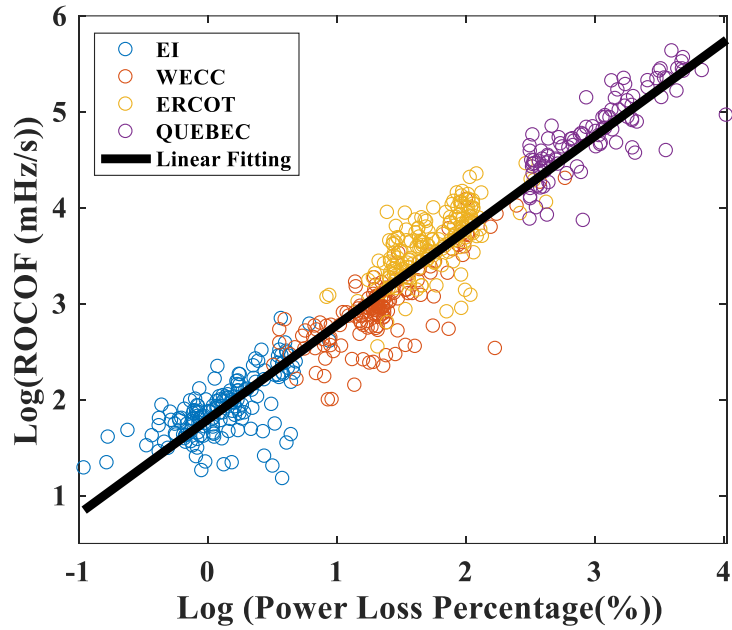


Figure 1-4. Scatter plot of log(ROCOF) vs. log(power loss percentage) of four interconnections in North America and the overall fitting line.

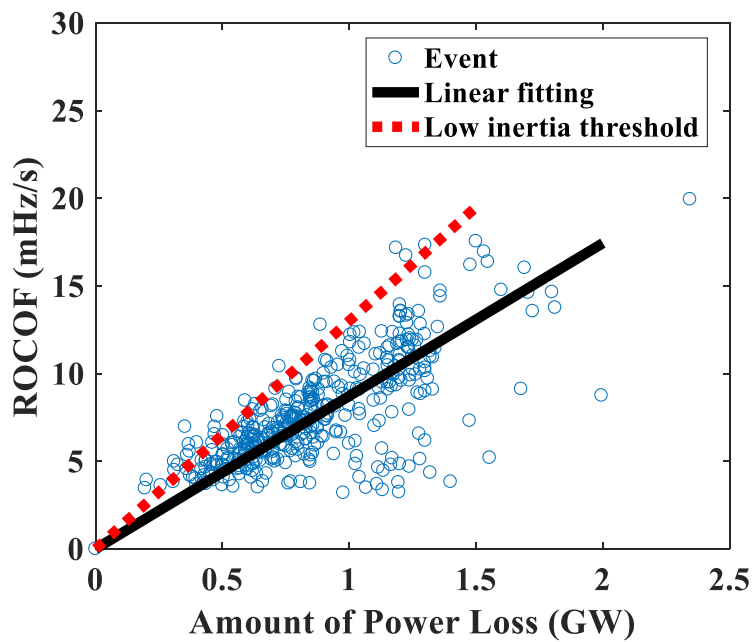


Figure 1-5. A scatter plot of ROCOF vs. the amount of power loss based on actual generation trip events in the EI.

In Figure 1-5, each event is marked as a blue circle. The straight line is the linear fitting of the dataset. A positive correlation between the two variables can be observed. The dashed line is the criterion indicating low inertia events by rotating the straight line counterclockwise. The events are collected from a real power system, so the power loss value is not as controllable as that in simulations. The dataset contains different inertia status. They are scattered on different lines crossing the origin with various slopes. Each line passes the coordinate origin because if there is no power loss, the ROCOF equals zero ideally.

By given system inertia, the frequency deviates faster due to a greater amount of power deficiency. In other words, the frequency drops slower by given power deficiency because of higher inertia. Therefore, each line can correspond to a certain inertia value. As the line rotates counterclockwise, the inertia decreases. By setting up a predefined line representing the low inertia threshold, it is able to distinguish low inertia events, which fall into the upper left area of the threshold. For example, if the predefined threshold is the dashed line in Figure 1-5, events at the upper left of the line can be recognized as low inertia. The threshold can be tailored for a specific bulk power system to find the relatively low inertia status based on statistic results of historical events.

To verify the above approach, function equation 1-2 is converted to be equation 1-5 by dividing the amount of power imbalance on both sides.

$$\frac{df}{dt*\Delta P} = \frac{f_0}{2H} \quad \text{Equation 1-5}$$

The left side indicates the ROCOF caused by each power imbalance unit, named as standard ROCOF in the project. Since the frequency before the disturbance is generally around the nominal value, standard ROCOF is inversely proportional to system inertia. According to

equation 1-5, the standard ROCOF of actual events happened in the EI from 2012 to 2015 are calculated.

Figure 1-6 presents the histogram of standard ROCOF values of the same group of historical generation trip events in EI. The curve shows the density approximation according to the histogram. It is noticed that the standard ROCOF distribution approximates the Gaussian distribution. Most values are between 5 and 15 mHz/s per GW. Less likely, it appears very big or very small. According to equation 1-5, the larger the standard ROCOF is, the lower inertia the system has. The events on the right tail of the distribution curve could reflect relatively low inertia status. Similarly, by setting up a maximum standard ROCOF, which is represented by the dashed line in Figure 1-6, events on the right side of the line can be categorized as low inertia events.

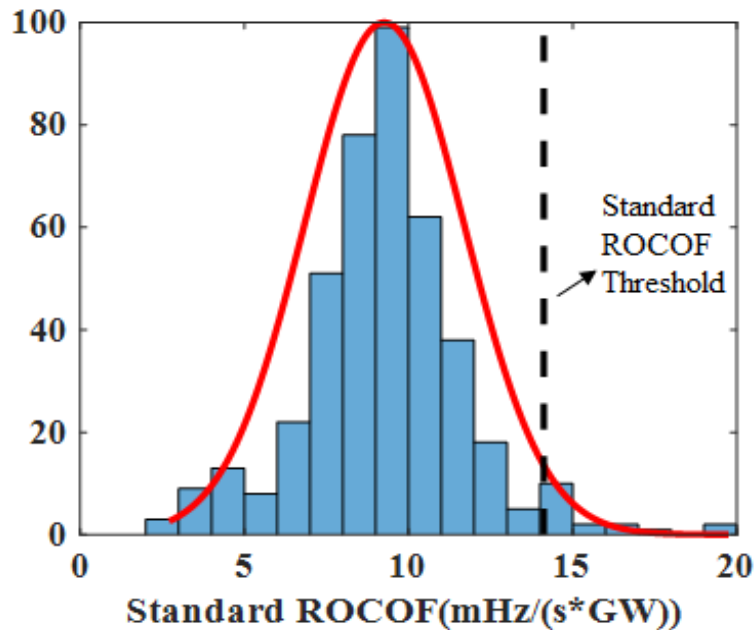
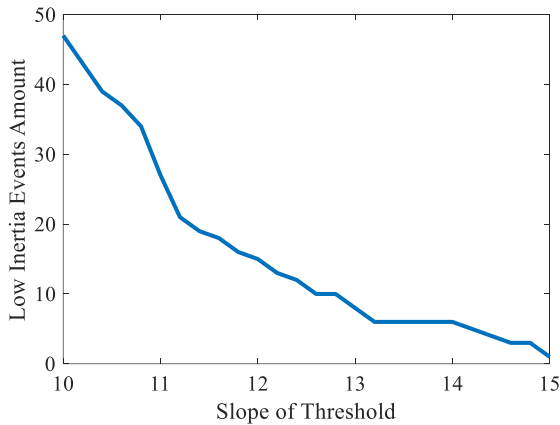


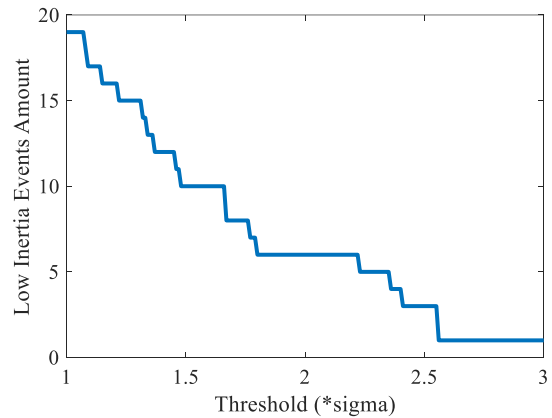
Figure 1-6. Distribution of historical generation trip events standard ROCOF.

Low inertia is a relative definition, which highly depends on the pre-defined threshold. Too low threshold brings in unnecessary concerns on regular disturbances; too high risks overlooking a security threatening system status. The operators and planners are willing to investigate the low inertia events for future operations. Proper threshold has to leverage the risk of missing true alerts and the vain work of dealing with false alarms.

Assuming the system condition doesn't change shortly, the selection of the threshold for low inertia identification can be based on the historical events in the previous year. Figure 1-7 displays the number of low inertia events identified by applying different thresholds to the historical events occurred in EI during the calendar year 2015. By changing the threshold, the slope of the dashed line in Figure 1-5 and the distance of the dashed line from the mean in Figure 1-6, the amount of identified low inertia events varies, as the curves shown in Figure 1-7. As a preliminary work, the decision of the threshold depends on the appropriate labor of low inertia events investigations.



a. Different thresholds in Figure 1-5.



b. Different thresholds in Figure 1-6.

Figure 1-7. Amount of identified low inertia events using different thresholds.

According to the confirmed generation trip event list published by North American Electric Reliability Corporation (NERC) [19], there are 165 generation trips happened in 2015, 13.75 occurrences each month on average. Assuming once per month event investigation is acceptable for system operators and planners, 1 out of 13.75 events happened under low inertia conditions. According to Figure 1-7, there would be 12 events identified as low inertia events if the slope of the threshold line in Figure 1-5 is 12.4, or 1.4 sigma from the mean value in Figure 1-6. In Figure 1-8, each circle represents individual generation trip event. The identified low inertia events are marked in black triangular, In order to validate the approach, some of the events, not all of them due to space limitation, are analyzed in section 1.7 to verify whether these events occurred under low inertia conditions.

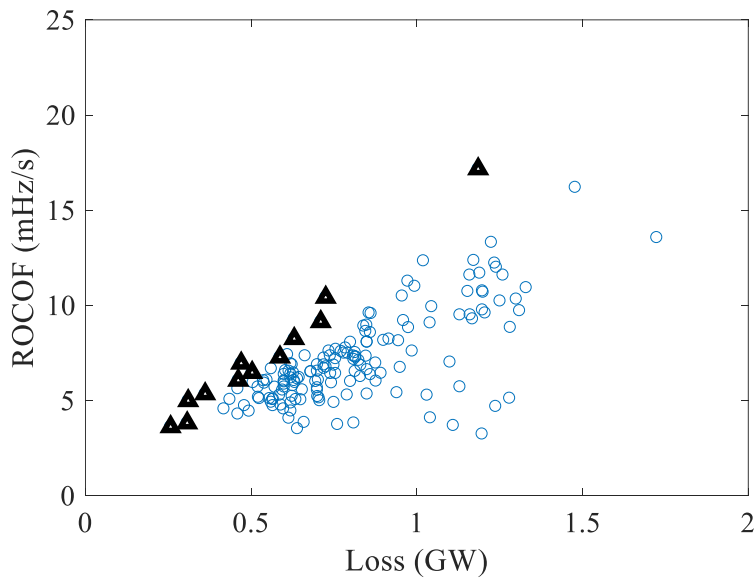


Figure 1-8. Marked low inertia events on scatter plot of historical events.

1.6 Implementation of real-time low inertia alerts

Based on the above analysis, disturbances under low inertia are of concern to system operators and planners. Real-time notifications of low inertia events would enhance system situation awareness. This section discusses the implementation of a real-time low inertia detection and alert system using the streaming data from FNET/GridEye. Figure 1-9 shows the main schema of implementation.

Prior to the implementation, a collection of sufficient generation trip events in given interconnections are required. The ROCOFs within the first 0.5 second following the disturbances are calculated, and the distribution of standard ROCOFs is analyzed. Since FNET/GridEye has been monitoring and archiving the dynamics of various bulk power systems for several years. The frequency responses of historical generation trip events are analyzed to select the low inertia criterion.



Figure 1-9. FNET/GridEye real-time low inertia detection implementation.

By implementing the low inertia detection approach on FNET/GridEye, events with standard ROCOFs higher than a specific threshold would be identified as low inertia status. According to the schema in Figure 1-9, the synchronous frequency measurements are transmitted from multiple FDRs to the data center, which monitors the system frequency and detects power imbalance events. Once an event is detected, the measurements are transmitted into the application immediately to do posterior analysis, including estimating the amount of power loss, event location, and event type, as well as the standard ROCOF. Comparison between the standard ROCOF and a given threshold determines whether the event occurred under low inertia condition or not. Once it is identified as a low inertia event, the system would send out notifications automatically via emails.

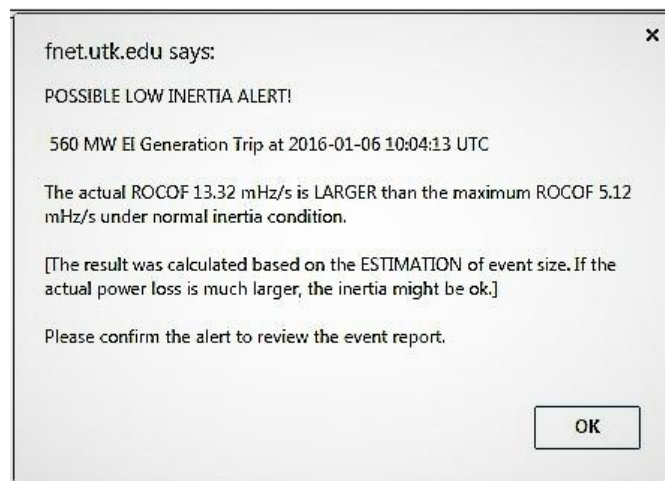


Figure 1-10. FNET/GridEye low inertia alert (The content has been modified due to confidential information).

Figure 1-10 and Figure 1-11 display an example of FNET/GridEye alert of possible low inertia and event analysis report. The possible low inertia alert pops up to warn the recipients of low inertia situations. Detailed event information will be displayed in the event report. By

implementing the low inertia indicator and alerting system at FNET/GridEye, system analyzers can take investigations on the low inertia events and actions can be taken by the operators and planners to put the systems in a safer status.

Basic Event Information					
Event Date	2016-01-06	Event Time	10:04:13 UTC	Event Type	Generation Trip
Point A	60.0124Hz	Point B	59.9437 Hz	Point C	59.8019 Hz
Interconnection	EI	ROCOF	13.32 mHz/s	Max Normal ROCOF	5.12 mHz/s
Estimated Amount	560 MW	Estimated Event Location	(35.9587, -83.9247)	Estimated Reliability Coordinator	TVA

Figure 1-11. A snapshot of FNET/GridEye event report (The content has been modified due to confidential information).

1.7 Low inertia events analysis

Reference [22] has published historical generation trip events happened in North America. According to the sorted standard ROCOF values of events in 2015, the top 12 events with highest standard ROCOFs identified in Figure 1-8 are listed in Table 1-2.

It can be seen that 10 out of 12 events happened during off-peak hours. Typically, during off-peak hours, less rotating generators are connected to the system due to lower demand. The system inertia could be relatively low. Also under heavy load conditions, the inertia could be reduced because of other factors, like the increasing penetration of renewables. The low inertia events predominately occur during off-peak hours. With increasing renewables, particularly solar, load patterns in the future will change and low inertia conditions could be seen mid-day. Due to space limitation in this section, the detailed information of four low inertia events is

presented. Figure 1-12 depicts the FDRs frequency measurements and the median frequency of all FDRs based on the measurements collected at FNET/GridEye. Each event is further explained as follows.

Table 1-2. List of identified low inertia events.

ID	Date & Time (UTC)	Amount of Power Loss (MW)	Peak/Off-peak Load
1	01/24/2015 15:31	503	Off peak
2	01/25/2015 00:10	307	Off peak
3	02/02/2015 14:33	257	Peak
4	04/12/2015 15:58	725	Off peak
5	05/25/2015 16:59	630	Off peak
6	08/10/2015 04:20	310	Off peak
7	10/01/2015 05:03	587	Off peak
8	10/04/2015 04:10	1185	Off peak
9	11/11 2015 18:26	470	Off peak
10	11/29/2015 17:17	710	Off peak
11	12/05/2015 22:52	461	Off peak
12	12/16/2015 16:55	361	Peak

Case 1: A conventional coal-based generator in North Dakota was disconnected on February 2nd, 2015 at 14:33:33 UTC time, which led to frequency deviation from 59.993Hz to 59.976Hz in less than 5 seconds. The frequency measurements of this event are displayed in Figure 1-12 (a). Prior to the trip, the generator was running at 257 MW. According to the statistical analysis of generation trip events in FNET/GridEye [23], EI has experienced many

more disturbances with greater power deficiency. However, this event could be of concern because it occurred under low inertia status in terms of standard ROCOF, which is up to 13.1 mHz/s per GW the during the inertia response. Therefore, even a small amount of power deficiency could lead to a fast frequency change, when the inertia is low enough.

Case 2: On December 16th, 2015 at 16:55:42 UTC time. The largest Iowa wind farm lost 361 MW power generation. FDRs' frequency measurements of this event are displayed in Figure 1-12 (b). The system frequency dropped from 60.001Hz to 59.961 Hz with a standard ROCOF at 14.2 mHz/s per GW due to a sudden loss of renewable resources. This is another low inertia event happened during peak hours, and the amount of power deficiency is relatively small.

Case 3: The event occurred on November 29th, 2015 at 17:17:32 UTC. The contingency was an Iowa coal-fueled electric generator tripped carrying 710 MW, slightly lower than the rated power output. The frequency dropped from 60.0065 Hz to 59.961 Hz. Each GW power loss leads to 12.3 mHz/s ROCOF during the inertial response. Heavy oscillations can be observed during the drop as shown in Figure 1-12 (c). This event happened during off-peak light load conditions. The system inertia would be reduced due to low system load and small rotating mass.

Case 4: On Jan 24th, 2015, a generator running at 503MW in Louisiana was tripped at 15:31:24 UTC time. The system frequency initiated at 59.992 Hz and decreased to 59.964 Hz. Each GW loss leads to 11.83 mHz/s ROCOF. The frequency measurements of this event are displayed in Figure 1-12 (d). This event occurred on Sunday when the load is smaller and thus the amount of system rotating mass is smaller than weekdays.

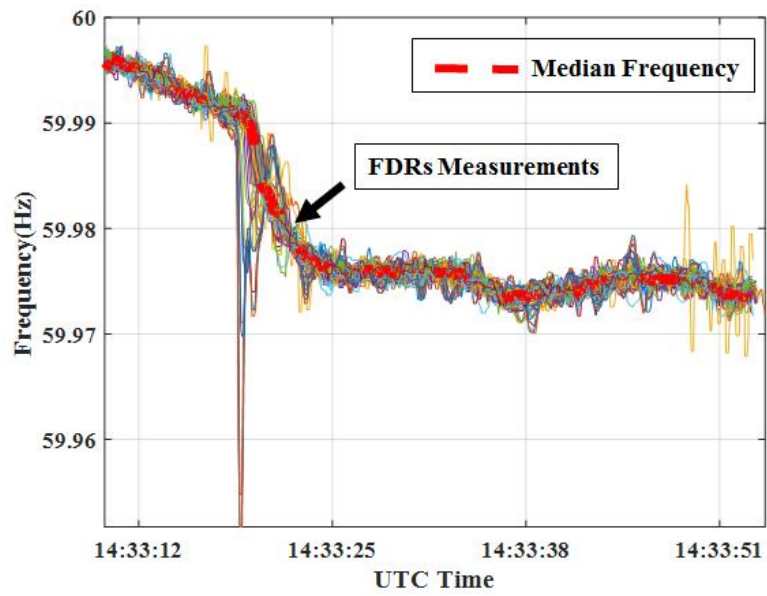
According to the event analysis above, most identified low inertia events occurred during off-peak hours, because the rotating mass is relatively reduced on account of low demand of power. However, during peak hour, there are some low inertia threats. A small amount of power

deficiency could lead to fast frequency decline. If a large amount of power generation is lost under this condition, it could lead to severe system stability problem.

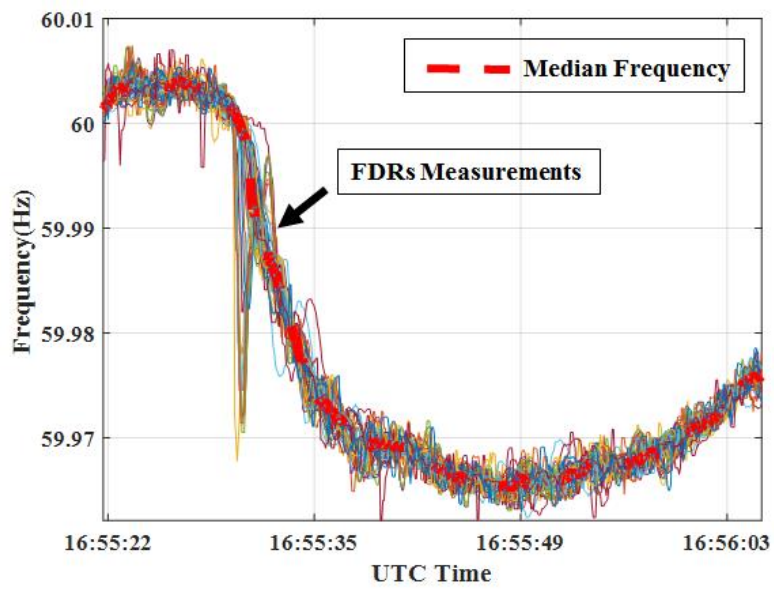
1.8 Conclusion

This project achieved the interpretations of system low inertia events and the implementation of an alerting system based on the high time-resolution synchronous measurements at FNET/GridEye. Analysis of historical generation trip events in North America illustrates the correlation of ROCOF vs. amount of power loss and the percentage of power loss. It discovers that the same percentage of generation imbalance influences the ROCOF in different power systems similarly. Inspired by this correlation, the standard ROCOF can be used as an inertia indicator. The indicator is applied to four major interconnections in North American, and it functions to identify events occurred under low inertia conditions. While low inertia is generally associated with off-peak conditions, it is expected that the increasing penetration of renewables will cause low inertia at different times of the day. The algorithm is implemented at FNET/GridEye automatically monitoring different power grids and alerting system operators and planners if the given systems experience low inertia conditions. Future research on the identified low inertia events will be committed for further valuable discoveries and benefits to power system situational awareness enhancements.

Figure 1-12. Frequency measurements of low inertia events.

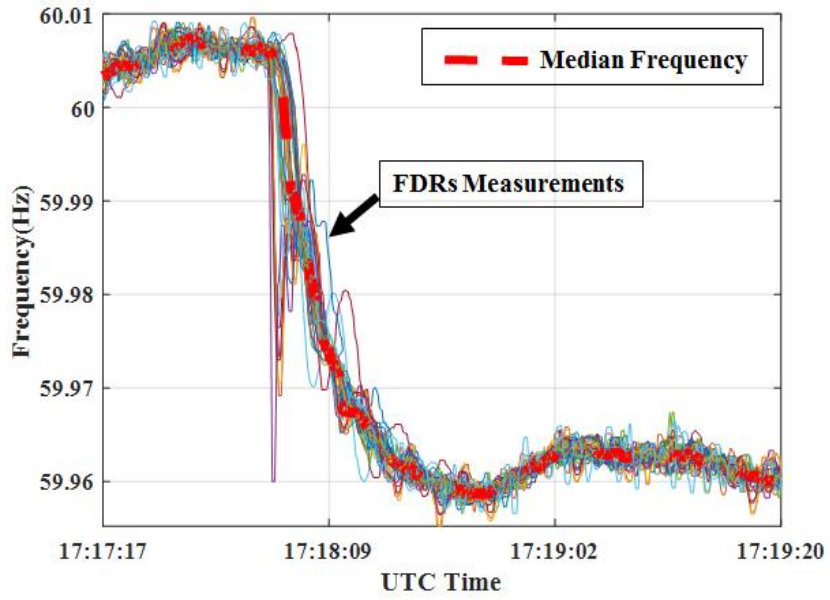


(a) Low inertia case 1.

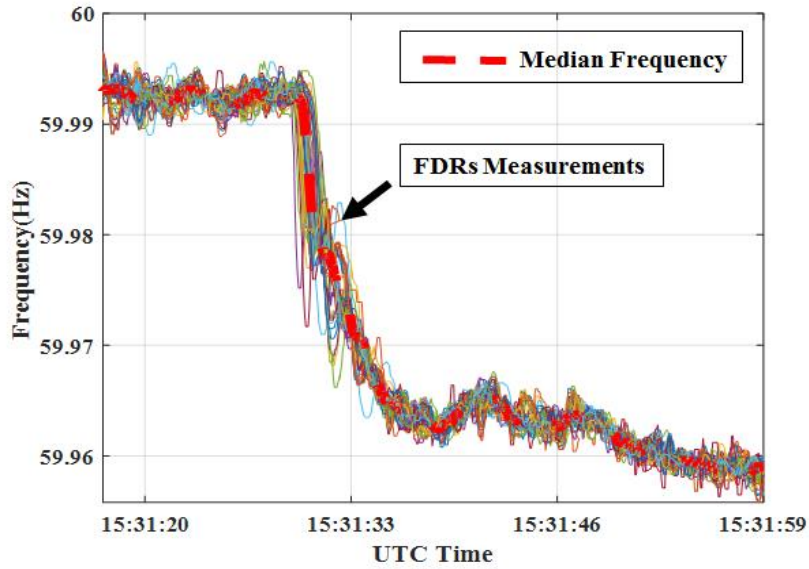


(b) Low inertia case 2.

Figure 1-12 Continued.



(c) Low inertia case 3.



(d) Low inertia case 4.

Figure 1-12 Continued.

CHAPTER 2 OBSERVATIONS OF THE INERTIAL FREQUENCY RESPONSE OF MAIN POWER GRIDS WORLDWIDE

2.1 Introduction

Frequency change in a large-scale power system reflects its generation-load balance and determines system stability [24]-[28]. For example, if a large generation plant is tripped, the frequency immediately drops. The period between the disturbance starting time and the governor completely arrests the decay is referred to as inertial frequency response. A dangerously low frequency nadir influences the system stability, because it might surpass the threshold of protection, and cause further customer outages, or even cascading blackouts [27]. Therefore, the inertial frequency responses have been obtaining the attention of system operators for years.

The rate of change of frequency during the inertial response reflects the system capability of deferring the frequency deviation under a certain size of power imbalance. It is impacted by multiple factors [29], such as the amount of power imbalance, governor reaction, and system inertia. It has been noticed from the real measurements that the ROCOFs of Electric Reliability Council of Texas (ERCOT) and Western Electricity Coordinating Council (WECC) are generally higher than those of Eastern Interconnection (EI). Considering the larger grid capacity of EI, it is interesting to know whether the ROCOFs of a specific interconnection are correlated to the grid generation capacity size. Hence, different power grids with various capacity sizes are analyzed in this project. FNET/GridEye has deployed hundreds of FDRs over the world, which have been collecting frequency measurement at high time resolution for more than ten years. Therefore, this project provided a statistic research based on the FNET/GridEye observations of historical generation trip events in different interconnections in order to disclose the potential correlation between ROCOF and capacity. With the understanding of such a relation, the typical ROCOFs of

a power grid with any amount of system capacity are able to be roughly estimated for further research.

2.2 Frequency response

Frequency response is one of the typical criteria reflecting the capability of maintaining the power system reliability. It is defined as the automatic corrective response of power system towards balancing the imparity between power supply and demand. As known that power electrical energy is a distinct commodity purchased without physical inventory [26]. In power grids, only rotational kinetic energy of the connected synchronous generators helps to balance the energy inequality, which is only enough to sustain the grid for cycles to seconds, depending on how much the gap is [30]. Even though the development of battery energy storage technology is expected to store energy efficiently mostly with the contribution of making utilization of renewable energy and advanced frequency regulation strategy [31]-[33], the main production and consumption of electricity must be matched continuously on account of its unique instantaneous trade characteristic. There is nowhere for extra product to go, either extra demand cannot be satisfied from anywhere. Nevertheless, the imbalance conflict actually happens all the time on either generation or load side, from small disturbance like residential usage resulting in stochastic fluctuations to large disturbance causing blackouts by tripping of generators or tie-lines [34] [35]. On the load side, various research are processed with the aspects of contribution to frequency regulations [36], like different optimization models of load control [37]-[40], intelligent controller applied on smart grids [41], investigation of available domestic and industrial load on regulation [9]. On the generation side, the influence on frequency response by energy loss essentially results from the mechanical motion principle of machines rotating in the grid, and the law of conservation of energy [3]. Proactive control strategies are applied on the

system side, on individual generator [42], or from the perspective of the whole system, which refers to the frequency control system. More explanation on this point will be presented in the following sections. In a nutshell, frequency is a crucial system metric responding to the energy balance condition between power supply and demand. According to the reports by the North American Reliability Corporation, frequency response [25], defined as the severity and recovery of the system frequency following large disturbances, especially trip of a large generator, has been the subject of considerably heightened concern.

The reliability of power system significantly depends on the frequency maintaining within certain predetermined limits around nominal operational frequency. The frequency increases while more generation than consumption, decreases on contrary condition as known as the fundamental of power system supported by rotating machines [43]. The system frequency response contains critical information about the system for maintaining reliable operation and determining effective control strategy. If the frequency decline or ascent following critical disturbance cannot be effectively stopped in a short time within certain stability range, protection would be triggered to cut off generator or load [44], even cascading events of grid failure could further cause large area blackout [45].

For a single disturbance, the rate of frequency change is considered to be invariant, which means the inertial frequency response is similar to a linear decline process [46]. This assumption is supported by the dynamic records of frequency responses monitored by FNET/GridEye. Figure 2-1 shows a typical frequency response to generation trip event happened in WECC which is recorded at FNET/GridEye. The red dash line is a straight line.

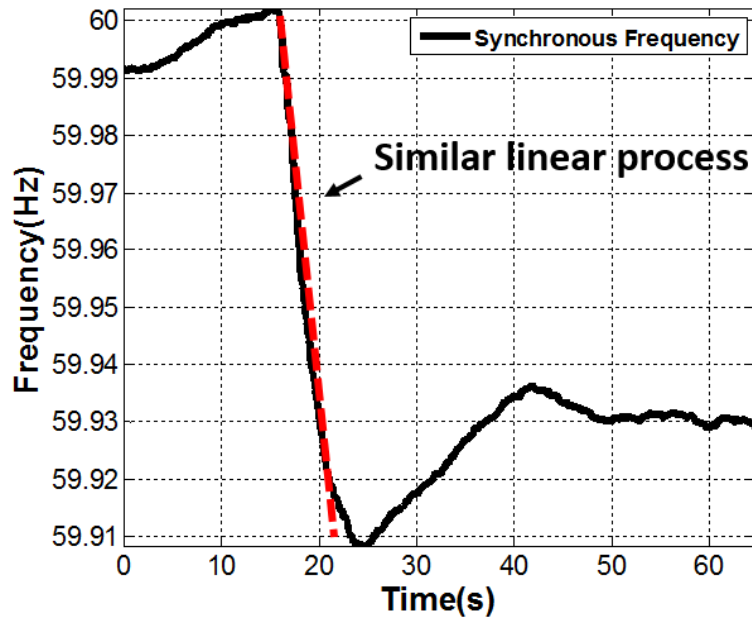


Figure 2-1. Frequency response to a generation trip in WECC.

From the moment that the frequency starts to drop to the point close to the nadir, the straight line overlaps a large portion of the frequency curve. During the short time close to the nadir, the frequency becomes nonlinear and declines slower. Therefore, the ROCOF during the inertial frequency response in this project is calculated as the slope between the starting point and the point where the frequency declines slower than a predetermined threshold.

2.3 Data processing on frequency response

All computations herein are based on the frequency measurement provided by FNET/GridEye. However, there are two major data quality issues in FDRs measurements: white noises and oscillations. These issues impact the frequency response slope calculations. Therefore, it is required to address these issues before the estimation.

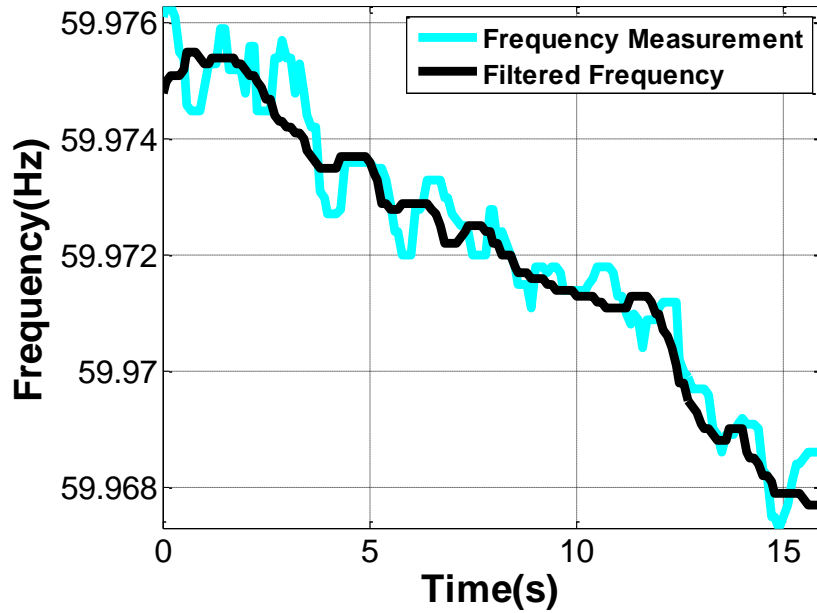


Figure 2-2. Frequency measurement white noise and the solution.

White noise generally exists, and it is unavoidable in realistic measurement. By using a traditional moving median filter, the white noise is mitigated effectively. For example, Figure 2-2 displays the comparison between the realistic frequency measurement and the corresponding data processed by moving median filter for the same frequency measurement. It is noticed that the frequency measurement curve contains irregular white noises, and the filtered curve successfully follows the measurement trend and moves smoothly.

After dealing with the white noise, the median value of the frequency measurements from all FDRs connected on the same grid is considered as the synchronous frequency of the specific grid. It is found that the synchronous frequency changes accompany with oscillations, and it may lead to overestimating the slope. In order to obtain precise ROCOF, high order polynomial curve is utilized to approximate the frequency decline and reduce the influence of oscillations [2]. The Figure 2-3 displays the comparison between the inertial frequency response containing obvious

oscillations and the approximating curve, which follows the decline trend well and remove the oscillations effectively. By using the moving median filter, and the high order polynomial approximation methods, a serial of historical generation trip events detected by FNET/GridEye are analyzed in this project, and their ROCOFs during the inertial frequency responses are estimated.

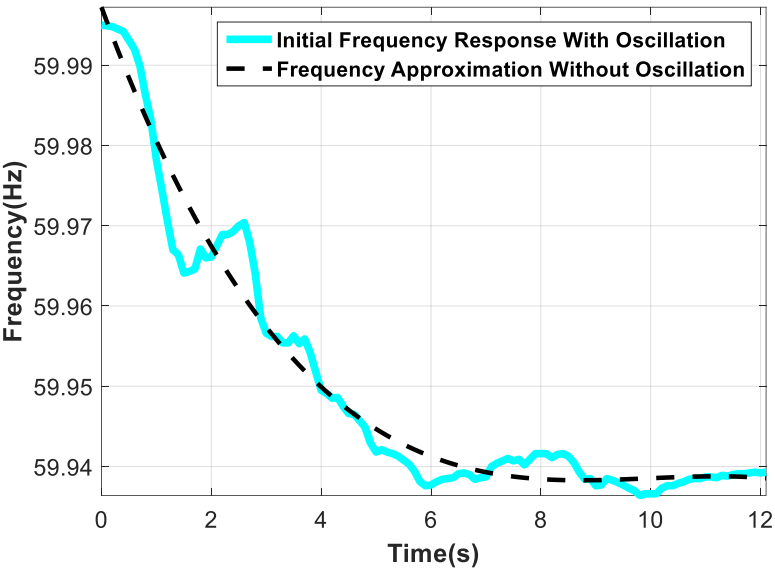


Figure 2-3. Frequency response oscillation and the solution.

2.4 Observation results

2.4.1 Results of grids in North America

Because the rate of the frequency change result is also dependent on the amount of power imbalance, and it is hard to guarantee that the historical disturbances cover every possible amount of power deficiency. Therefore, the distribution of the rate of frequency change is used to do a comparison between various power grids in this project. Several independent

interconnections in North America are analyzed in this project, including EI, WECC, ERCOT, Hydro-Quebec (Quebec), and Hawaiian Electric Industries (Hawaii). Over 200 FDRs are deployed in North America covering these grids as shown in Figure 2-4.

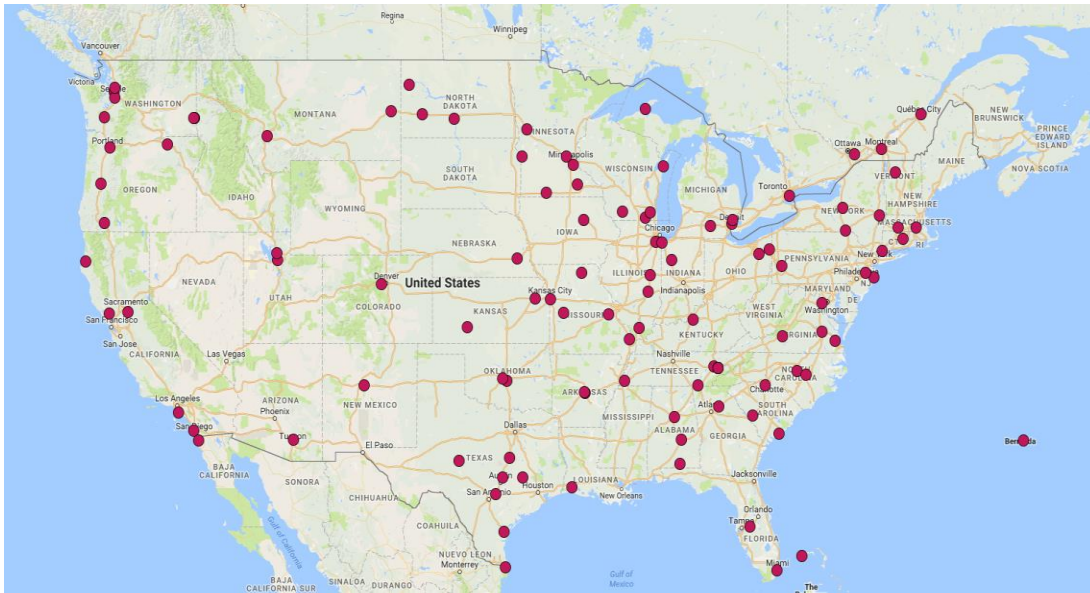
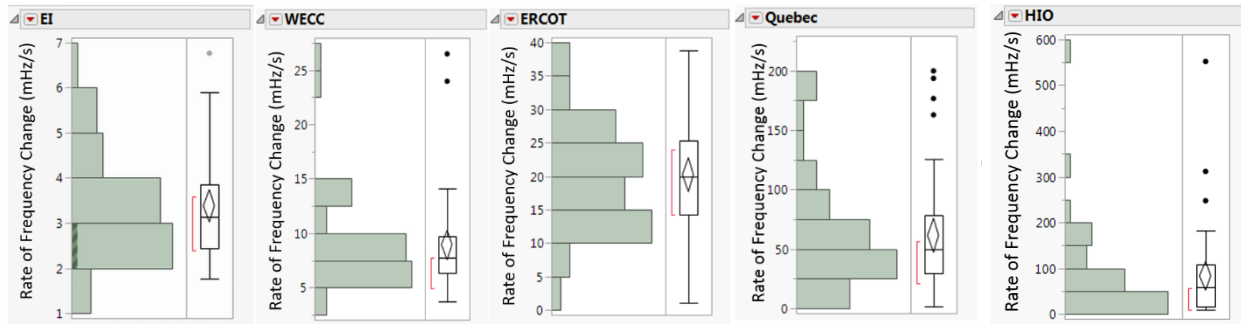


Figure 2-4. FDRs deployment in North America.

FNET/GridEye monitors their frequencies in real time, and detects generation trip and load shedding events automatically. There are a large number of dynamics records for each Interconnection. The date and time of each event are traceable in the database. By random selections, tens of event cases in each interconnection are used to evaluate the distribution of the rate of frequency change during inertial frequency responses.

By applying the approach described above to the selected events, the rate of frequency change of each event is estimated based on the FNET/GridEye measurement. For each interconnection, the distribution of frequency change rate is concluded and shown in Figure 2-5.



(a) EI. (b) WECC. (c) ERCOT. (d) QUEBEC. (e) Hawaii.

Figure 2-5. Rate of frequency change distribution analysis of grids in North America.

In Figure 2-5, it indicates the distributions and corresponding boxplots of the rates of frequency change estimates of interconnections in North America. In each plot, the vertical axis represents the rate of frequency change in mHz/s. it is separated into ordinal ranges. The horizontal length of each bar represents the percentage of occurrence in a specific range.

Taking the EI rate distribution as an example, it indicates that mostly, the rate of frequency change is larger than 2 mHz/s and less than 4 mHz/s. A very slight chance, the rate is larger than 6 mHz/s. Comparing with the distribution plots of other grids, it briefly tells the rate of frequency change mostly locates in the range between 2.0 and 6.0 mHz/s in EI, between 5.0 and 15.0 mHz in WECC, between 5.0 and 30.0 mHz/s in ERCOT, less than 100.0 mHz/s in Quebec, and less than 200 mHz/s in Hawaii. The boxplot on the right side of distribution plot displays its quartile range and outliers. In each boxplot, the 20%, 50%, 75% quartile values are represented by the bottom line, middle line, and top line of the box, respectively. The mean value corresponds the position of the center of diamond in the box. Outside of 1.5 times IQR (IQR= 75% quartile-25% quartile) shown as the short lines above and below the box, the outliers are represented as black dots if they exist. With respect to the frequency measurement archived in FNET/GridEye system, about 50 historical disturbances for each grid are analyzed in this project. It is noticed from

Figure 2-5 that for a certain power grid, the rate of frequency change during inertial frequency response mostly locates in a certain range. The position and length of the range differ in various grids. It is obvious the main range of rate of frequency change of Hawaii power grid is as far as 200 mHz/s, which is tremendously higher than the rate of EI, less than 10 mHz/s. The detailed quartile values of the distribution analysis results are listed in Table 2-1.

Table 2-1. Rate of frequency decline quartiles for grids in North America.

Interconnection in North America	Capacity (GW)	First Quartile (mHz/s)	Median (mHz/s)	Third Quartile (mHz/s)
EI	669	2.446	3.139	3.865
WECC	200	6.378	7.733	9.710
ERCOT	109	14.232	19.951	25.248
Quebec	37	29.860	50.009	78.225
Hawaii	1.8	16.229	58.124	107.178

In Table 2-1, the quartile variables of the five interconnections increases as the capacity decreasing, and the length of range increases as well. In larger grids which have higher generation capacities, the median rates and the interquartile ranges are apparently less than in smaller grids. It indicates that frequency in power grids with larger generation capacity declines slower. Therefore they are able to buy more time for governors to response and stabilize the frequency. The similar result is displayed in Figure 2-6.

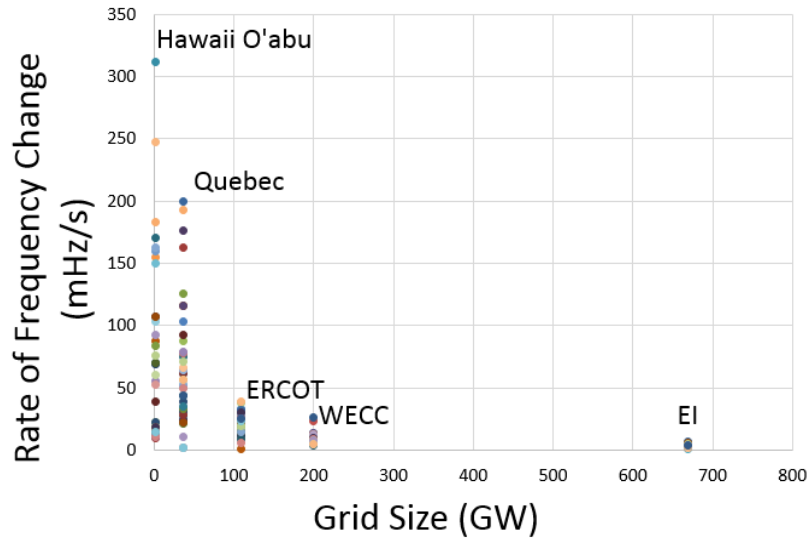


Figure 2-6. Rate of frequency decline for grids in North America.

Figure 2-6 displays the trend of rate of frequency change with respect to the grid size. Each column of dots stands for a specific interconnection. Each dot represents the rate of frequency change for a particular event happened in the system. Combined with the result in Table 2-1, it can be concluded that: firstly, during the inertial frequency response, the rate of frequency change in a larger capacity power grid is less than in smaller grids. For example, EI owns the biggest generation capacity in North America, about 669GW. Its range is much smaller than other interconnections; secondly, the distribution is more scattered in smaller grids. For instance, the Hawaii grid, as the first column from the left side, is able to generate at most 1.8 GW electricity in theory. Its rate of frequency change ranges over hundreds mHz/s width, which is over 50 times of the range of EI.

2.4.2 Results of oversea grids

The power grids in North America have been analyzed for years based on FNET/GirdEye real-time monitoring system. The event detection application has been applied to multiple grids

effectively, and it notices significant events timely and correctly. Based on the measurement data and detection reports, the attribute of grids in North America is described above, and it shows an obvious descending trend of rate as grid size grows. In order to enhance the credibility of the conclusion, the measurement collected by FDRs deployed overseas are used to supplement the research.



Figure 2-7. FDR coverage worldwide.

FNET/GridEye has deployed hundreds of FDRs in different countries worldwide, as shown in Figure 2-7 [17], it has been covering independent interconnections including the Regional Group Continental Europe, the Regional Group Nordic, United Kingdom, Ireland, Egypt, China, India, Japan, et.al. The approach of event detection is simplified to check threshold-crossing of the derivative of the frequency after a median filter reducing the impact of white noise.

By utilizing the simplified event detection method, when the frequency turns obviously out of the nominal frequency and gradually becomes stable at a lower level within 12 seconds, it is

identified as a potential transient that is attributed to system disturbance. Although it lacks real operation information in these overseas grids, it is believed that the reason for these transients is the loss of a large amount of power supply according to years of analysis experience of FNET/GridEye team. After solving the impact of white noise using moving median filter, the rates of frequency change during linear inertial frequency responses to potential disturbances are obtained.

By appropriate selection of tens of potential events in different grids, the estimate results of rate of frequency change for large power grids overseas are procured utilizing moving median filter and simplified event detection process. For each grid, the median rate of frequency change value of selected cases is used to represent its typical rate. In

Table 2-2, it lists different power grids' capacities and their typical rates of frequency change. It is noticed that the median rate tends to reduce as the grid size grows.

The results are also displayed as scattered dots in Figure 2-8 in order to visualize their relationship. In Figure 2-8, the x-axis is the size of power grid in GW, and the y-axis stands for the rate of frequency change in mHz/s. Each dot represents the median rate value for a specific power grid, including the power grids in North America. It is noticed that for power grids with smaller size, the median rates are generally higher than power grids with larger sizes. By utilizing the curve fitting toolbox in Matlab 2012a, the relation between the median rate and the grid capacity is approximated using a function: $y = a * x^{-b}$, as the cyan dashed line shown in Figure 2-8. In the function, x means the grid size, and y means the median rate. The coefficients a and b are both positive. At the same time, the curve supports the assumption in section III, that ROCOFs could be inversely proportional to the grid size under the same inertia and power imbalance condition.

Table 2-2. Estimation on overseas grids.

Grid(Country) Name	Grid Size(GW)	Median Rate (mHz/s)
Ireland	7.67	96.53
Chile	18.16	71.36
Egypt	59.45	34.81
Australia	63.25	47.83
Nordic	87.17	16.84
South Korea	94.35	19.58
United Kingdom	96.41	22.79
Brazil	121.68	74.27
Japan(50Hz)	146.66	15.44
Japan(60Hz)	146.66	11.2
Eastern Europe	260.02	13.87
Continental Europe	736.59	9.13
China (State Grid)	883.06	13.49

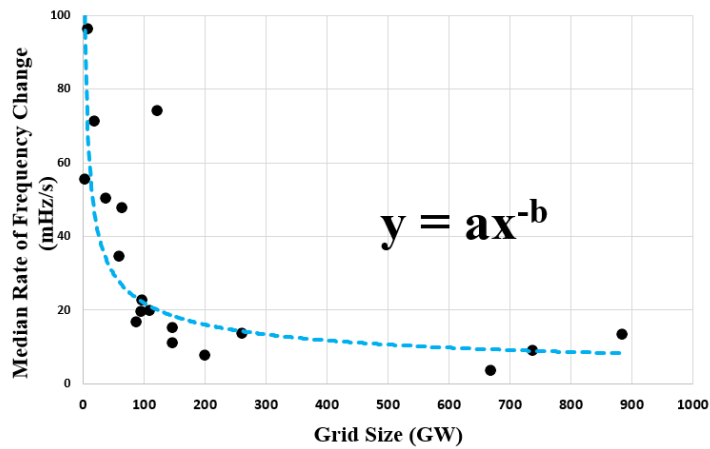


Figure 2-8. Estimation of the median rate during inertial frequency response.

2.5 Conclusion

In this project, the inertial frequency responses in various power grids over the world are studied based on the high time-resolution frequency measurement provided by FNET/GridEye. It is the first time to do such a research among realistic power grids worldwide. The North American grids analysis demonstrates that in a smaller power grid, the general ROCOFs are more scattered in a larger range with higher median value. Combining the analysis of historical events in oversea power grids with different capacity sizes, it reveals the relationship between the grid size and the median rate of frequency change during the inertial frequency response. It is disclosed that the median ROCOF is approximately inversely proportional to the grid size. With the understanding of the relation, the general ROCOFs for unobservable power grids can be roughly estimated. The discovery also inspires further research on the inertial frequency response analysis with respect to the ratio of power loss amount to total capacity.

CHAPTER 3 MULTIPLE LINEAR REGRESSION BASED DISTURBANCE MAGNITUDE ESTIMATIONS FOR BULK POWER SYSTEMS

3.1 Introduction

The sudden occurrence of power imbalance in power systems, like loss of generators or a large amount of load shedding, leads to instant frequency deviation from the nominal value. Analysis of generation trip events in a wide-area power grid is important for system operation. More specifically, system operators and power engineers are willing to know the details of every disturbance about when, where, what kind of disturbance, and then assess how it may influence system operation, etc. It also benefits pinpointing the source of any abnormal conditions quickly and takes preempt actions to prevent further damages as necessary. Besides, the disturbance magnitude is one of the fundamental parameters in system operation and control, such as frequency control [47], economic dispatching [48], under-frequency load shedding [49], demand response, islanding, etc. The accuracy of the analysis results influences other research results validity. In this project, it is proposed to estimate the magnitude of power imbalances based on multiple linear regression pursuing better accuracy than the traditional method.

With the increasing deployment of PMUs, which measure grid phasor attributes using Global Position System (GPS) signal, system dynamic information is available at a high-time resolution. Using synchrophasor measurements to analyze system disturbances becomes dominant [50]. Several approaches have been developed to estimate the disturbance magnitude. Preliminary, the method proposed by C.M. Laffoon and J.F. Calvert in 1927, is to measure the weight and the temperate rise of the cooling medium to determine the generator loss under actual operating conditions of a specific generator [51]. However, its applicability is limited to specific

generators and includes a time delay. More general methods for direct estimation using phasor measurements can be categorized into two groups: 1) using the rate of change of frequency; 2) using the frequency deviations before and after disturbances. However, they have several shortcomings [47]. By using the rate of change of frequency, the value of power deficiency can only be precisely estimated at the initial instant of the disturbance, but it is difficult to determine the exact initial moment of the disturbance in practice for a large system due to electromechanical wave propagation. In addition, determining the system frequency bias factor (i.e. system inertia) is subordinated to the combined inertia of online generators, which is not a handy parameter for a large power system, especially in de-regulated environments [52]. Therefore, the method is utilized mostly for small power systems rather than large interconnections such as the U.S. Eastern Interconnection (EI) system. Applying the second approach, which multiplies the frequency deviation by a coefficient, to a serial of real generation trip events happened in EI shown very low accuracy in disturbance magnitude estimation. The reason is that it excessively simplifies the relation and ignores many impact factors, such as the seasonal change of the system and the system load characteristics, etc. Considering these reasons that lead to inaccuracy, an adaptive approach based on multiple linear regression is proposed in this project to estimate the disturbance magnitude.

3.2 FNET/GridEye generation trip detection

At FNET/GridEye, frequency measurements collected from distributed sensors are utilized to detect trips of generations. Under normal operations, system frequency varies around the nominal value within an acceptable range. For interconnections in North America, the nominal frequency is 60 Hz. When there is a significant imbalance between power supply and demand, a series of system controls respond to the contingency immediately. The frequency deviates from

the nominal values after the disturbance and settles when the controls completely arrest the deviation. Figure 3-1 presents a typical frequency response to power supply loss.

It can be seen from Figure 3-1 that the frequency decreases right after a certain amount of power supply reduction caused by generation trip. This sudden frequency deviation activates the event trigger, which is triggered by a high rate of change of frequency. Operators will be informed both the occurrence of the contingency and basic information on the contingency such as how much generation is disconnected. Typically, the amount of power imbalance is estimated by simply assuming that the disturbance magnitude is proportional to the frequency deviation, leading to very poor accuracy. In this project, multiple impact factors are considered to investigate their significance in disturbance magnitude estimation and further improve the estimation accuracy.

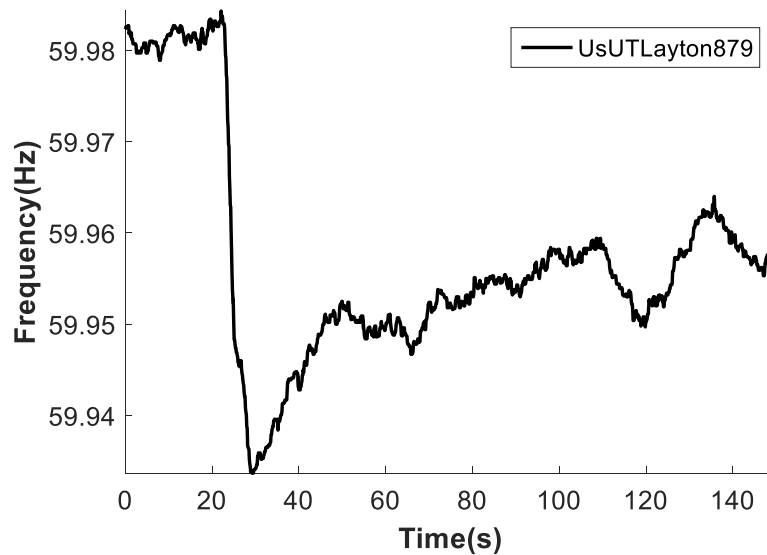


Figure 3-1. Typical frequency response to a generation trip event.

3.3 Multiple linear regression

Multiple Linear Regression (MLR), as a generally used predictive analysis, is used to explain the relationship between two or more variables by fitting a linear equation to the observed data. Besides, it is able to identify the principle variables which are strongly correlated with the dependent variable. The basic theory of MLR can be found in [53]-[54]. Here, it simply describes the basic approach for estimating the magnitude of power imbalance in disturbances as a linear combination of other variables according to the equation 3-1.

$$y = \beta_0 + \beta_1 x_1 + \beta_2 x_2 + \dots + \beta_k x_k + \varepsilon \quad \text{Equation 3-1}$$

The main idea of this method is to extract the relationships between power imbalance y and other variables $\{x_1, x_2, \dots, x_k\}$ from historical disturbances measurements, and utilize their relationships to estimate the power imbalances of future disturbances. The $\{x_1, x_2, \dots, x_k\}$ in equation 3-1 indicates several system variables when the disturbance occurs, which have linear relations with imbalance size, and are obtainable using present techniques, including but not limited to the following items: the season, time of day, day of week, peak hour, the pre-disturbance (referred as Point A) frequency, post-disturbance (referred as Point B) frequency, nadir frequency (referred as Point C), and slope of frequency changes.

$\{\beta_0, \beta_1, \dots, \beta_k\}$ are the coefficients for the regression line. They will be obtained through analysis on large amount of historical data points. ε indicates the residuals, which is normally subject to the normal distribution with mean value 0 and variance σ . By applying the MLR algorithms, the linear regression line is optimized with minimal sum of squares of the deviations, and the $\{\beta_0, \beta_1, \dots, \beta_k\}$ would be defined.

Besides the transient frequency during disturbances, the load is considered as one of the aspects that highly related to the power imbalance. However, for the realistic large power

systems, the system load condition is not always available for most of the research. Since the system load is known having seasonal and daily characteristics, in this project, several factors of the moments of disturbance occurrences are used to reflect the load, like the season, the peak hour, etc. As an example to explain the variables $x_i \ i \in (1 \sim k)$ in equation 3-1, Table 3-1 lists the available variables which may have correlations with the magnitude of power imbalance for establishing the MLR models.

Table 3-1. Analyzed system variables.

Date & Time	Summer	Winter	Off Peak	Day
1/5/2013 5:37	-1	1	1	Sat
4/25/2014 12:20	-1	-1	0	Fri
Initial Slope	Nadir Slope	Freq A	Freq B	Freq C
(mHz/s)	(mHz/s)	(Hz)	(Hz)	(Hz)
23.52	11.85	60.001	59.941	59.946
18.57	5.13	60.026	59.971	59.985

In Table 3-1. Analyzed system variables., the attributes “Summer”, “Winter”, “Off-Peak”, and “Day” columns describe different aspects of the disturbance occurrence time. If both “Summer” and “Winter” are both negative, the season is either “Spring” or “Autumn”. Because the system load in “Spring” and “Autumn” is lighter than that in “Summer” and “Winter”. “Initial Slope”, “Nadir slope”, “Freq A”, “Freq B”, and “Freq C” represent the characteristics of frequency response to the disturbance. These variables, directly or indirectly, determine the correspondence between disturbance magnitudes and the frequency deviation after a disturbance. In this project, these factors are analyzed to build an MLR model to estimate disturbance magnitudes.

3.4 Model establishment

According to the MLR method and the parameters depicted above, sufficient historical generation trip events happened in EI and WECC from January 2013 to March 2015 are analyzed, and the results are displayed below. The principal variables which are strongly correlated with the magnitude of power imbalance in EI are identified as the season, frequency values at point A and point C, the initial and nadir slopes of the frequency decline during inertial frequency response. The estimation of disturbance magnitude for EI is in terms of equation 3-2 below.

$$y = a_0 + a_1 * f_A + a_2 * f_C + a_3 * (Winter) + a_4 * (Summer) + a_5 * slope_{initial} + a_6 * slope_{nadir}$$

Equation 3-2

where a_i $i \in (0 \sim 6)$ are the coefficients, f_A is the frequency at point A, f_C is the frequency nadir, the $slope_{initial}$, $slope_{nadir}$ represent the initial and nadir slopes of frequency decline during inertial frequency response [56].

In an MLR model, the variables are analyzed and categorized into significant and non-significant. Adding a significant variable to a regression model makes the model more effective. While adding an unimportant variable would make the predictions worse.

A hypothesis test is conducted, which is used to test the validity of a claim that is made about a population [57]. The hypothesis test uses a p -value to weigh the strength of the evidence. The p -value is a number between 0 and 1 and interpreted in the following way:

- A small p -value (typically ≤ 0.05) indicates strong evidence against the null hypothesis.
- A large p -value (> 0.05) indicates weak evidence against the null hypothesis.
- p -values very close to the cutoff (0.05) are considered to be marginal (could go either way).

Table 3-2 lists the estimates of each coefficient and the corresponding significance test results. In Table 3-2, the p -value is listed in column “Prob>|t|” column. It can be told that the variables listed are all significant to establish MLR model for estimating the size of power imbalance. According to the least square principle, the performance of both proposed MLR-based approach and the typically used method are summarized for comparison in Table 3-3.

Table 3-2. Parameter estimates for EI.

Term	Coefficient	Prob> t
Intercept	294335.2	<0.0001
Freq A	18478.5	<0.0001
Freq C	-23382.8	<0.0001
Summer	65.1	0.0006
Winter	52.5	0.0008
Initial slope	69.1	0.0078
Nadir slope	-88.4	0.0097

Table 3-3. Fitting summary comparison for EI.

Index	MLR Method	Static Beta Method
RSquare	0.652	0.480
Root Mean Square Error	202.9	244.5
Mean of Response	885.0	950.5

It is mentioned previously that the traditional approach assumes a static proportional correlation between the size and the frequency deviation. Herein, the traditional method is referred

as “static beta method”. In contrast, the new approach is able to identify the adaptive relationships between the size and other factors. It is referred as the “MLR method”. The RSquare value tells how close the data are to the regression line. It is also known as the coefficient of determination for multiple regression. The higher the RSquare is, the better the model works. The root mean square error (RMSE) measures the differences between values estimated by the MLR model and actual observations. The mean of response is the mean of the analyzed power imbalance values. Combined with the significance test, the MLR model can be used to fit the observations for two general conditions: the RSquare value is as high as possible, and every variable is significant to the response.

Based on the same observations, the fitting indexes of the traditional static-beta method are calculated and presented in Table 3-3. Both RSquare and RMSE indicate that MLR model fits the training samples better than the static-beta method. By using the MLR model to EI system, the estimation RSquare is improved by 36%, and the RMSE is reduced by 17%.

With respect to the MLR regression line for EI, it is noticed that the size of power imbalance is significantly correlated with the frequency response, not just the frequency values at different points, but also the speeds of frequency changes after the disturbances. Besides, the size estimate is also strongly influenced by the seasons. The same frequency deviations can be caused by lower loss of generation when the load is relatively higher in summer and winter than in shoulder seasons.

The approach is applied to historical events of generation trip happened in WECC from January 2013 and March 2015. The same regression model is established as in equation 3-2, but the coefficients are different.

The corresponding coefficients and hypothesis test results of WECC model are listed in Table 3-4. The fitting summary is displayed in Table 3-5 comparing with the fitting indexes of traditional static-beta approach. Considering the higher RSquare value, and the hypothesis test results which are all less than 0.05 risk level, the MLR line is considered to be effectively fitting for the power imbalances of generation trip events in WECC. It is noticed that the characteristics of inertial frequency response and season are still the principal factors that can be used to estimate the magnitude of power imbalances. From the hypothesis testing results in Table 3-4, it can be seen that “Winter” shows a relatively poor correlation with the size of generation trip. It still satisfies the rule of strong correlation.

Table 3-4. Parameter estimates for WECC.

Term	Coefficient	Prob> t
Intercept	119799.3	<0.0001
Freq A	6965.8	<0.0001
Freq C	-8961.5	<0.0001
Summer	-117.4	<0.0001
Winter	-55.64	0.0353
Initial Slope	37.86	0.0001
Nadir Slope	-60.89	0.0014

Considering the high RSquare value, and the hypothesis test results which are all less than 0.05 risk level, the MLR line in equation 3-3 is considered to be effectively fitting for the power imbalances of generation trip events in WECC. It is noticed that the characteristics of inertial frequency response and season are still the significant factors determining the magnitude

of power imbalances. By using the MLR model to WECC system, the estimation RSquare is improved by 43%, and the RMSE is reduced by 35%.

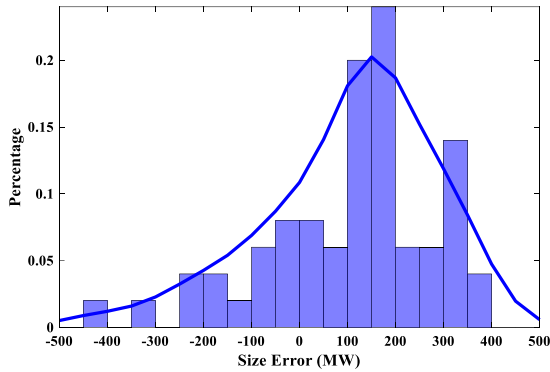
Table 3-5. Fitting summary comparison for WECC.

Index	MLR Method	Static Beta Method
RSquare	0.837	0.584
Root Mean Square Error	191.9	297.5
Mean of Response	878.8	746.1

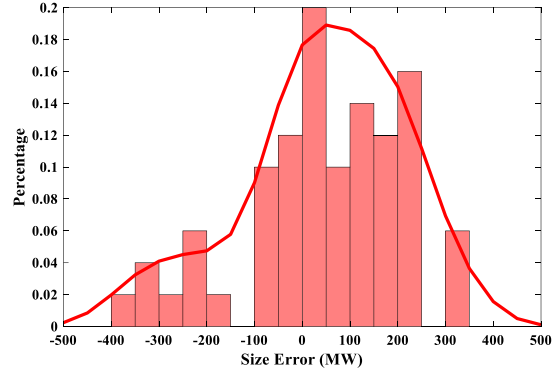
3.5 Model validation

Historical generation trip events from Jan. 2013 to Mar. 2015 are used to establish the MLR models for estimating power imbalance magnitudes of EI and WECC. In this section, different groups of real generation trip events happened from April 2015 to September 2015 are used to verify the models. It is mentioned above that the traditional approach assumes the static proportional correlation between the size and the frequency deviation. Therefore, this traditional approach is named as static beta approach here. The new approach is able to identify the adaptive relationships between the size and other factors. It is named as adaptive approach here. Two approaches are applied to the same testing events in EI and WECC to verify the improvement of the adaptive estimation approach.

From April 2015 and September 2015, 58 large amount of generation trip events happened in EI are processed using the two approaches. The error distribution plots for each approach are shown in Figure 3-2 and the comparing parameters are displayed in Table 3-6.



a. Static beta estimation error distribution.



b. MLR based estimation error distribution.

Figure 3-2. Comparison of estimate errors distribution in EI.

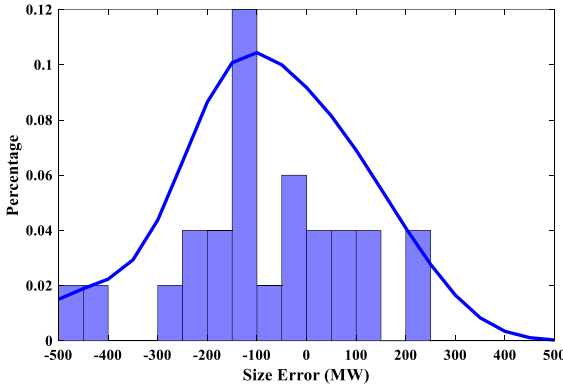
It is noticed from the error distribution in Figure 3-2, the static beta approach results in error mostly around 100 to 200 MW. 22 out of 58 events falls within this range. Also, the errors spread in a large range between plus and minus 400 MW. However, the errors of adaptive estimates are distributed between plus and minus 100 MW. For the analyzed 58 events, 26 cases are estimated with errors in this range. The errors spread within a smaller range in plus and minus 350 MW compared with the traditional approach.

Table 3-6 shows the distribution analysis results of these two groups of errors, including the mean error, standard deviation, etc. The lower mean value stands for a smaller central error, the lower standard deviation, and standard error mean the narrower the error variation. In the comparison, the adaptive estimation errors reveal higher estimation accuracy with smaller values at each item. Therefore, the adaptive estimate considering more factors is believed to be capable of reducing the general estimate error effectively.

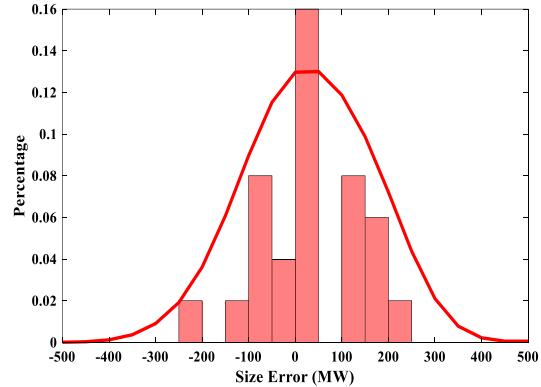
The same comparison is applied to 24 generation trip events happened in WECC from April 2015 to Sep 2015. The distributions of the two groups of estimates errors displayed in Figure 3-3.

Table 3-6. Parameter estimates for EI.

Statistics	Static Beta Method	MLR Method
	Estimation Error	Estimation Error
Mean	103.8	45.4
Std Deviation	174.4	165.5
Std Error Mean	22.9	21.7
Observations	58	58



a. Static beta estimation error distribution.



b. MLR based estimation error distribution.

Figure 3-3. Comparison of estimate errors distribution in WECC.

From Figure 3-3, it is noticed that the errors are more centralized around -100 to -150 MW by using the traditional method, which means the method mostly underestimates the power loss. Nevertheless, the errors in adaptive estimation are mostly gathered within 50 MW and spread out evenly in both directions. The chance to have very large errors occurred in the adaptive method is also less than in the static beta approach. The corresponding distribution parameters are concluded in Table 3-7.

The parameters in Table 3-7 are the same as those in Table 3-6. Similarly, with less error mean value and smaller variation, the adaptive approach is proved to be more effective in estimating the size of tripped generation in WECC.

Table 3-7. Parameter estimates for WECC.

Statistics	Static Beta Method Estimation Error	MLR Method Estimation Error
Mean	-86.9	29.3
Std Deviation	173.0	109.1
Std Error Mean	35.3	22.3
Observations	24	24

3.6 Conclusion

This project successfully accomplishes an adaptive approach to estimate the magnitude of power imbalance using multiple linear regression models on the basis of dynamic phasor measurements with improved estimation accuracy. According to the analysis on sufficient actual generation trip disturbances happened in large power systems, it discovers several significant variables which are strongly associated with the magnitude for specific systems, including the frequency values before the disturbance and at the nadir, the initial and nadir frequency decline slopes during inertial frequency responses, the season of disturbance occurrences. Eventually, the adaptive estimations are verified to reduce the estimation errors effectively using different actual generation trip disturbances.

CHAPTER 4 DEVELOPMENT OF REAL-TIME EVENT DETECTION APPLICATION PACKAGE FOR ELECTRIC UTILITIES

4.1 Introduction

FNET/GridEye has earned years' experience and success stories in monitoring power systems in large area and detecting types of disturbance in real time. The applications utilize the phasor measurements from distributed Frequency Disturbance Recorders (FDRs) sampling rate at 10 fps. This project breaks through the limit of FDRs usages and develops a real-time event detection application using PMUs phasor measurements considering its growing popularity and wide deployment in utilities. PMUs are the phasor sensors mostly installed by individual utilities on their transmission networks. It would significantly facilitate utilities explorations on PMUs based applications. Since the applications running at FNET/GridEye have been demonstrated of capability by years' service experience, it is proposed to apply these applications to PMUs measurements in utilities. As a pilot practice, the event detection and triangulation applications are firstly rebuilt for PMUs use at the current stage. The project establishes an individual application package which is able to be plugged into different data source interfaces. It not just widens the knowledge and research experience of the real-time synchrophasor based application development, but also benefits to power systems situational awareness enhancement and system resiliency improvement. A utility with PMUs installation covering its own territory is able to observe events initiated outside of its footprint. Because of the data confidentiality, the PMUs measurements between utilities are not allowed to be shared. If the event notifications generated by different utilities' are able to be shared, it would significantly increase the stability and reliability of the entire interconnection.

4.2 Application package design

As a pilot application package, this project targets to install the real-time event detection, localization algorithms with event notification tool for PMUs measurements. Figure 4-1 shows the blocks of this package at the current stage.

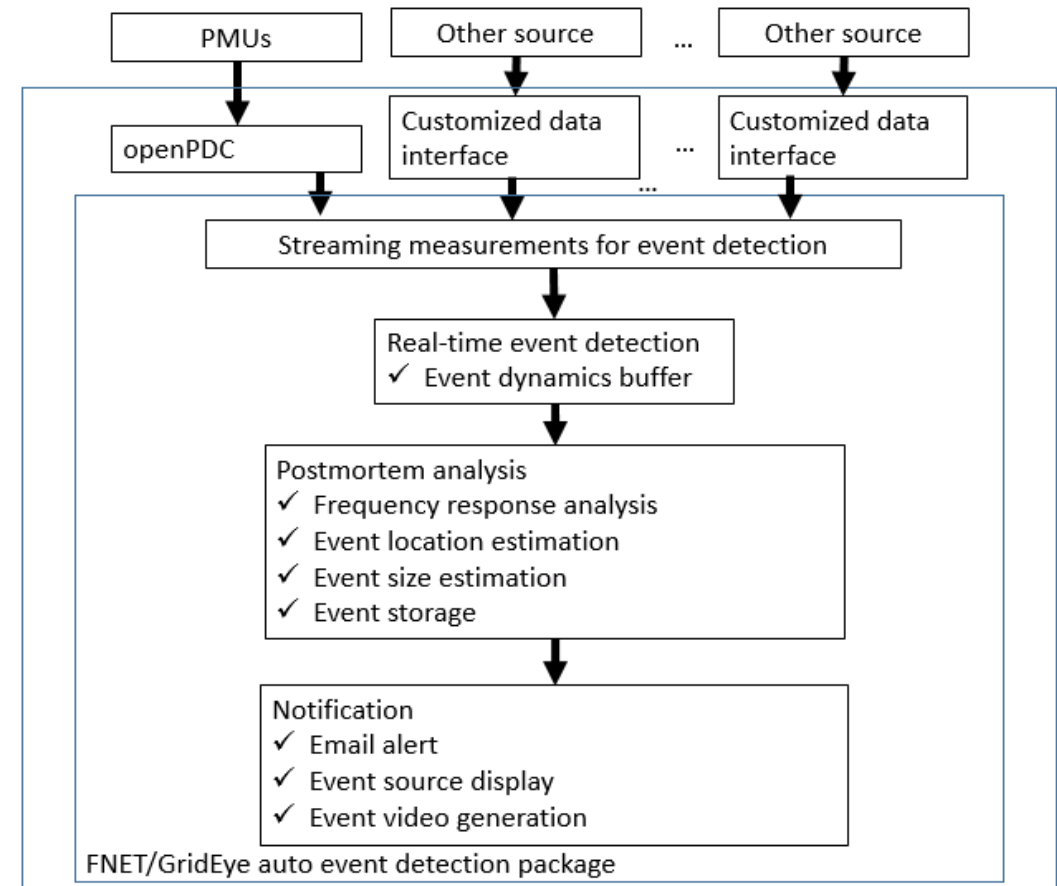


Figure 4-1. Diagram of FNET/GridEye event detection application package.

It consists of three main functions: real-time event detection, postmortem event analysis, and event notifications. Between the main functions and the field PMUs measurements, it is designed to use customized data interfaces to connect them. Since PMU measurements are

synchronized with GPS single, the data is streamed into the detection module according to the time stamp. As shown in the diagram, openPDC is one of the data interfaces connecting field PMUs measurement and the applications. Since openPDC is an open source tool to process time-series data, it is widely used in utilities in North America. However, when it is unavailable, the PMUs measurements need a customized interface to interact with the event detection package.

4.3 Application modules

It can be seen from Figure 4-1, the package consists of three modules: event detection, event analysis, and notification. The data interfaces collect real-time PMUs measurements and export the data to the package in a common format. Then the data will be streamed to the detection module according to the time tags. In the event detection module, it searches for large values of the rate of change of frequency (ROCOF). When a sudden deficiency of either power supply or demand encounters, the machine rotating will be withdrawn or speeded up on account of the imbalance between the mechanical energy input and electrical energy consumption. The machines responding to a sudden loss of power generation results in frequency declines immediately. On the contrary, the frequency increases when a large amount of system load is tripped until the primary control is fully delivered and has arrested the frequency deviations. After a candidate event is triggered, the posterior analysis is necessary to tell when and where, what kind of disturbance is detected, which is the function of the analysis module.

The Time delay of arrival (TDOA) based triangulation of event source is a patent-filed technology developed at FNET/GridEye [58]. It assumes even electromagnetic propagation in all directions and neglects the difference between the electric distance and geographic distance. It produces the coordinates of the disturbance source by solving the electromagnetic propagation equations in equation 4-1.

$$\begin{aligned}
(x_1 - x_e)^2 + (y_1 - y_e)^2 &= V^2(t_1 - t_e)^2 \\
(x_2 - x_e)^2 + (y_2 - y_e)^2 &= V^2(t_2 - t_e)^2 \\
&\dots \\
(x_n - x_e)^2 + (y_n - y_e)^2 &= V^2(t_n - t_e)^2
\end{aligned}
\tag{Equation 4-1}$$

where (x_e, y_e) is the coordinates of the disturbance source. (x_i, y_i) , $i = 1, 2, \dots, n$ refer to the coordinates of PMUs. t_e stands for the moment of the disturbance and t_i , $i = 1, 2, \dots, n$ indicates the moment when individual PMUs sense the disturbance.

Besides, the magnitude of disturbance will be estimated according to the system frequency response dynamics. The frequency deviation is considered as proportional to the amount of power imbalance ignoring the system inertia variations. Eventually, the estimation results of the detect disturbances will be archived in a database.

The event notification module achieves the functions of prompting instant alerts, normally via email and event visualizations. The email body contains the posterior analysis results and optional visualizations. For the sake of independent operations, the modules are encapsulated individually. In the case realistic installations in utilities, there will be minor modifications on each module in terms of the regulations of specific companies.

4.4 Challenges of the application package

4.4.1 Difference between FDR and PMU measurements

There are some differences between FDR and PMU. FDR is one kind of single-phase power systems phasor sensor installed at the distribution networks. It is normally plugged into the wall outlets to measure voltage phase magnitude, angle, and frequency at 10 samples per second. PMU mostly refers to the three-phase phasor sensor installed at the transmission networks. PMU collects three-phase bus voltage and line current magnitude, angle, and local

frequency measurement too. It is able to provide the active power and reactive power through specific transmission lines according to the voltage and current measurements.

FDR measurements are transmitted to the data center located at the University of Tennessee, Knoxville (UTK) and Oak Ridge National Laboratory (ORNL) for management and application. FNET/GridEye is able to monitor bulk power systems (BPSs) dynamics in large area. PMUs measurements are typically managed by individual utilities. For example, the EI transmission network in North America is supported and interconnected by several utilities. There is not a master center to coll. Therefore, the monitoring systems built on PMUs are usually limited to regional dynamics. Due to these differences, the applications for PMU use present several challenges and opportunities for further research.

4.4.2 Challenges and opportunities in industry implementations

During the implementations of the applications in multiple industries, including utilities and ISOs, it encountered several challenges and opportunities for PMU use.

4.4.2.1 Data size challenge

The data size of PMU measurements is much larger than FDR during the same time period, which becomes a challenge for the machine. PMU reports phasor measurements typically 30 to 120 samples per second, which is much higher than FDR at 10 samples per second. Besides the sample rate, the number of PMU aggravates the data size on another dimension. Currently in North America, there are about tens of PMUs installed in individual utilities. In ISOs or RTOs, the amount of available PMUs reaches several hundred. The number keeps increasing rapidly. As new measurements keep coming in for real-time applications, the machine is required to be capable of processing a large amount of data quickly.

Regarding the data size issue, it is designed to select partial informative PMUs for the application. Sometimes, there are multiple PMUs installed in one substation to monitor different

buses. There is slight measurement difference from PMUs in the same substation, which doesn't impact the application significantly. The responses at different substations contribute to the disturbance localization algorithm well. Therefore, it is effective to select one PMU from each station for the application. Besides, due to the monotonicity of the frequency response to power imbalance event, low sample rate doesn't impair the algorithm which searches for continuous and large rates of frequency change. Therefore, in the detection module, the PMU measurements are examined at an adjustable interval, which could relieve the pressure of machine processing capability.

4.4.2.2 Data quality checking

There are several data quality issues existing in PMU measurements, such as measurement spikes, periodical recurrences, missing data, etc. Bad data is possible to pull a false alarm when the system is operating right. Therefore, it requires examining the data quality in real-time and processes the bad data as necessary. These patterns of bad data are similarly existing in FDR measurements. The same methods can be used to deal with bad quality data. However, PMU measurement interval is very short, the regular data quality checking process would occupy a lot of machine resources and lead to obvious latency. Therefore, the data quality testing is conducted at a lower frequency than the PMU sample rate. Besides, further research on PMU measurement quality are ongoing in industries.

4.4.2.3 Regional monitoring

The transmission networks managed by different utilities sometimes are interconnected. The application can be triggered by disturbances outside of the utility footprint. Based on the measurements of internal PMUs, the triangulation algorithm would lead to a wrong result of the

disturbance location [59]. Regarding the regional monitoring drawback, it is designed to build a distributed detection system as shown in Figure 4-2.

In the system, the event detection application is installed in individual utilities. There is a master control center collecting the regional alarm from utilities. In the control center, it identifies internal and external disturbance and determines the source of the event using the PMU data from a specific utility. By distributed installations of the application, each application works based on internal PMUs from individual utilities. It mitigates the pressure of processing data in large size and saves resources for the data transmission and archive in ISOs or RTOs.

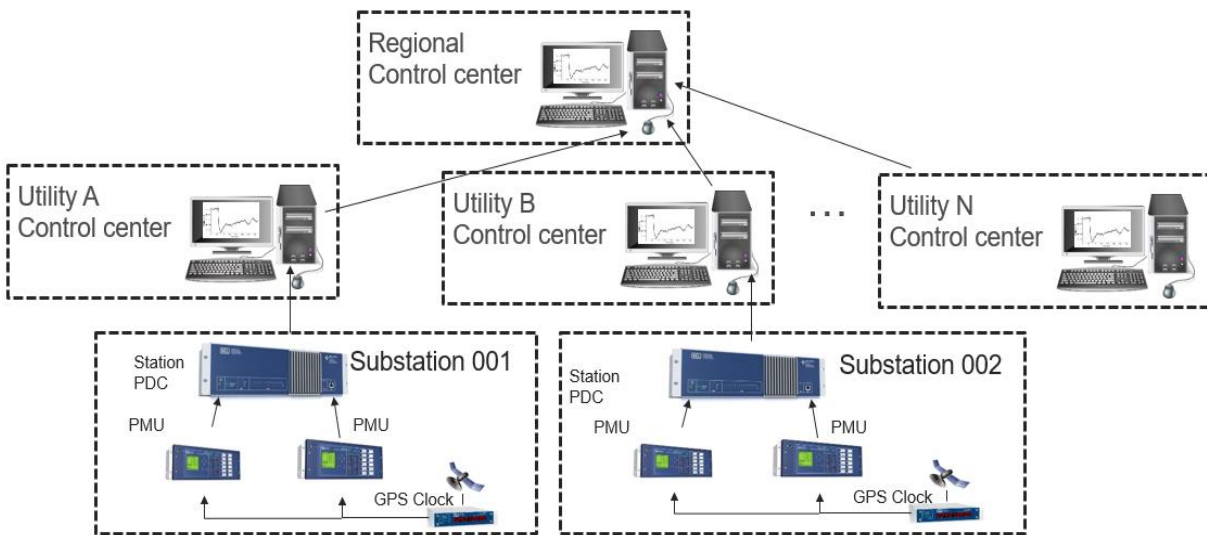


Figure 4-2. Distributed event detection system.

4.4.2.4 Application exploration

PMU allows detailed interpretation of the dynamics due to the high sample rate, and other types of measurements regarding the transmission networks, which bring in opportunities for exploring improved and novel applications for situation awareness enhancement. For example,

The PMU ROCOF measurement reflects the change of system frequency in high time resolution. Therefore, the event detection algorithm can be improved directly based on the ROCOF measurement without calculating ROCOF using frequency measurement. It searches for sudden change and great value of ROCOF measurements on multiple PMUs. Combining with the frequency measurement, which indicates the direction of frequency deviation, the sudden loss of a generation and a large amount of load can be detected instantly.

PMU enables different types of measurement, and the measurements contain information directly indicating from transmission networks. New applications can be developed using PMUs measurements. One of the exploration is the real-time detection of transmission line switching operations. The frequency responses to transmission line opening and reclosing events are similar. Therefore, the application searches for sudden changes in ROCOF measurement and the frequency deviations in two directions at the same time. Some PMUs at the receiving end sense the loss of power supply, and some others sense the loss of power load at the sending end. The voltage angle difference between the sending end and the receiving end is increased when the transmission line is opened like shown in Figure 4-3. Vice versa, it becomes smaller if the line is recovered back to service, as shown in Figure 4-4.

It is proposed to detect transmission line switching operations according to PMU frequency measurement. Combined with the voltage angle measurements, the status change of the line can be recognized. The detailed information regarding the detection and identification methods are described in [60].

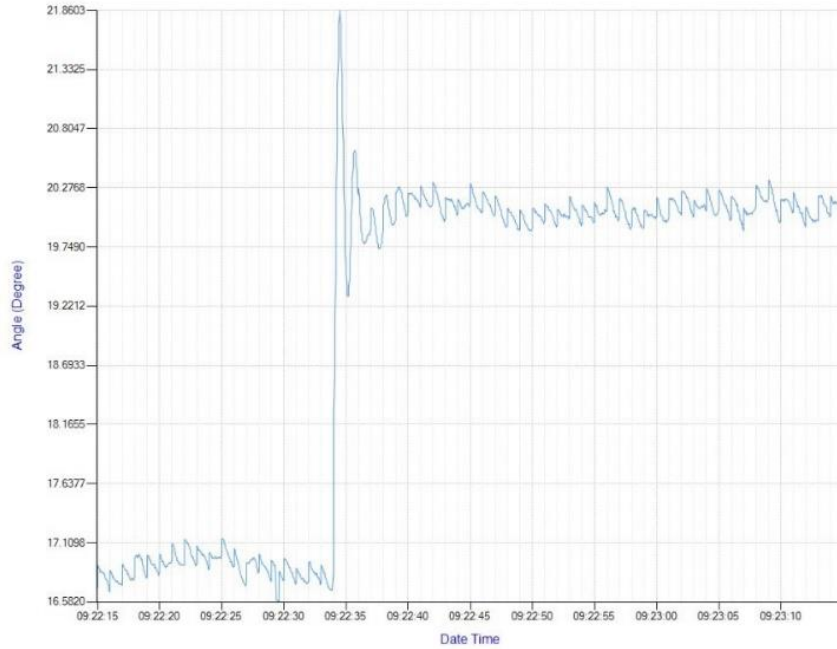


Figure 4-3. Voltage angle difference during a transmission line trip event.

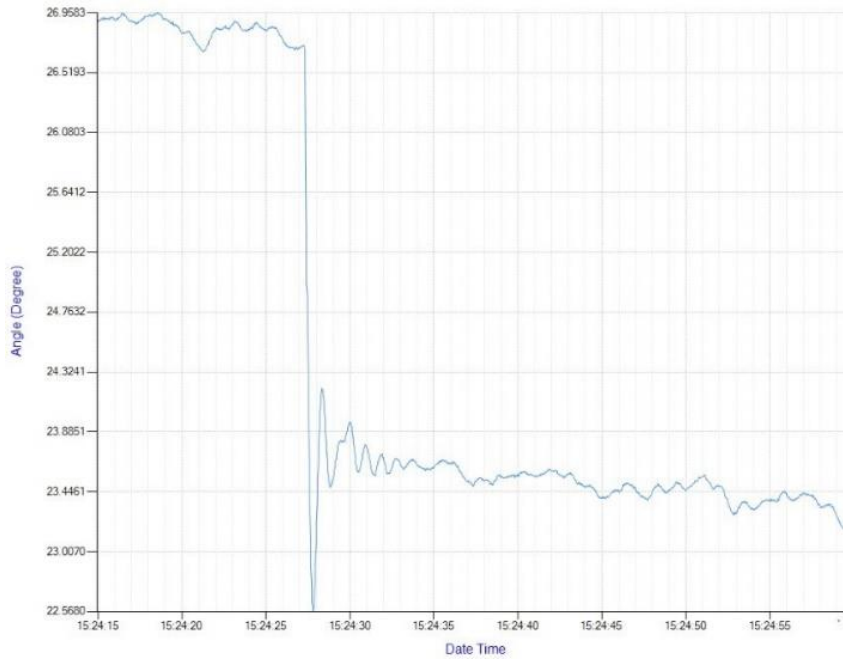


Figure 4-4. Voltage angle difference during a transmission line reclosing event.

4.5 Successful implementation Stories

The FNET/GridEye generation trip and load shedding detection and triangulation application are packaged according to the design in Figure 4-1 for a field test. Either in openPDC or in customized interfaces, the detection module runs in 24/7 to search any sudden disturbance in real-time. Once it is triggered, it will call the triangulation module to do the posterior analysis. After that, the visualization tools will be executed. Customized data interfaces need to be developed for other types of data source when openPDC is unavailable. Until now, it has been installed or accomplished the first testing phase in several utilities and ISO in Eastern Interconnection. This section presents the success stories of three companies. Due to the data confidentiality requirement, some experimental data and results are not allowed to be included in this dissertation.

4.5.1 Southern Company

Southern Company (SOCO) is the gas and electric utility in the southern United States. It serves about 9 million gas and electric customers in Alabama, Georgia, Mississippi and Florida etc. There are about 65 PMUs installed in SOCO footprint. The PMUs measurements are collected by openPDC. As shown in

Figure 4-5. There are three layers in openPDC: input, action, and output. The input layer is normally used to process non-real-time data and streams them into openPDC as an independent input. Likewise, the output layer transforms data available for openPDC output.

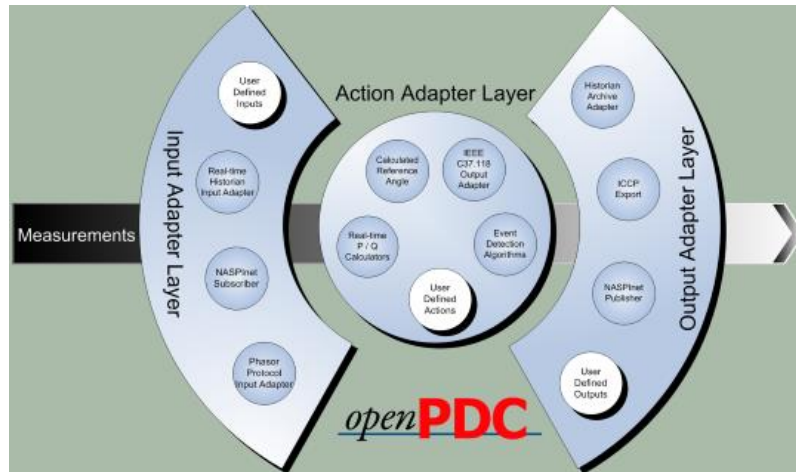


Figure 4-5. openPDC three user-defined layers structure.

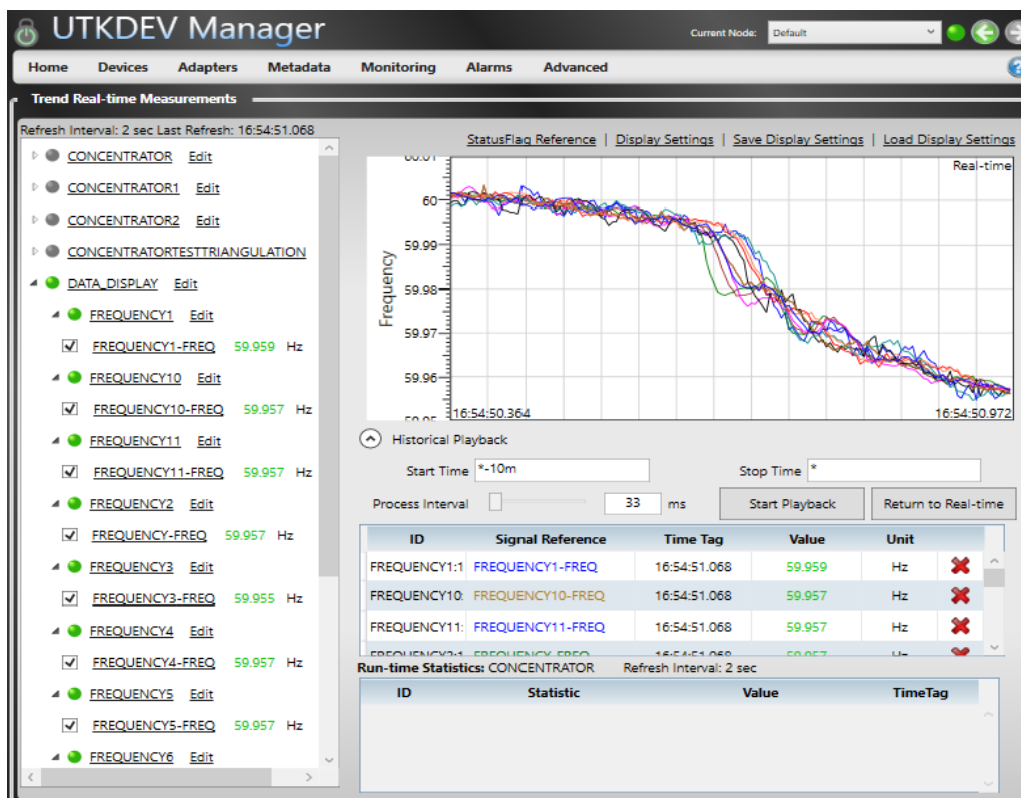


Figure 4-6. Example of a detected event in openPDC.

Since the PMUs data are collected by openPDC according to standard IEEE C37.118, and it doesn't need output in openPDC, the event detection module can be assembled in an action adapter, which does the process and calculation on given measurements. Time-series measurements like the chunk of data shown in Figure 4-6 will trigger the detection tool. Figure 4-6 shows a typical GUI of openPDC. UTKDEV Manager is a customized openPDC user interface. Instead of installing openPDC and run the service, GPA provides a complete software application template for developers to build self-designed GUI. The UTKDEV is a customized openPDC for SOCO.

4.5.2 PJM Interconnection

PJM Interconnection, termed as PJM, is a Regional Transmission Organization (RTO) operating an electric transmission system in Eastern Interconnection and serving all or parts of Delaware, Illinois, Indiana, Kentucky, Maryland, Michigan, New Jersey, North Carolina, Ohio, Pennsylvania, Tennessee, Virginia and the District of Columbia. The PMUs measurements are also collected by openPDC. Therefore, the same package as installed in SOCO can be used for PJM Interconnection.

There are over 400 PMUs measurements streaming to PJM data center rating at 30 samples per second in real-time. The big data size issue becomes one of the primary problems during the implementation. Therefore, not all PMUs measurements are processed into the event detection action adapter. Often there are multiple PMUs in one substation or power plant. If any disturbance encounters, the synchrophasor response within station should be similar. Another FNET/GridEye application, the trip of transmission line detection is also installed at PJM. Additionally, a novel application regarding sudden transmission line switching operations is developed using the PMU voltage angle measurements.

4.5.3 GEIRI North America

GEIRI is abbreviated for Global Energy Interconnection Research Institute. The project at this company is to install the FNET/GridEye event detection package for Jiangsu Electric Grid Company in China. Jiangsu Electric Power Company, terms as Jiangsu Company constructs, operates and manages power grids in Jiangsu province as the largest subsidiary of State Grid Corporation of China. There are over 100 PMUs installed and collecting system phasors as 25fps rate. However, the PMUs measurements are unavailable to stream into any open source tools like openPDC on account of the regulation of cybersecurity. Therefore, a specific data interface is developed for Jiangsu Company in this condition.

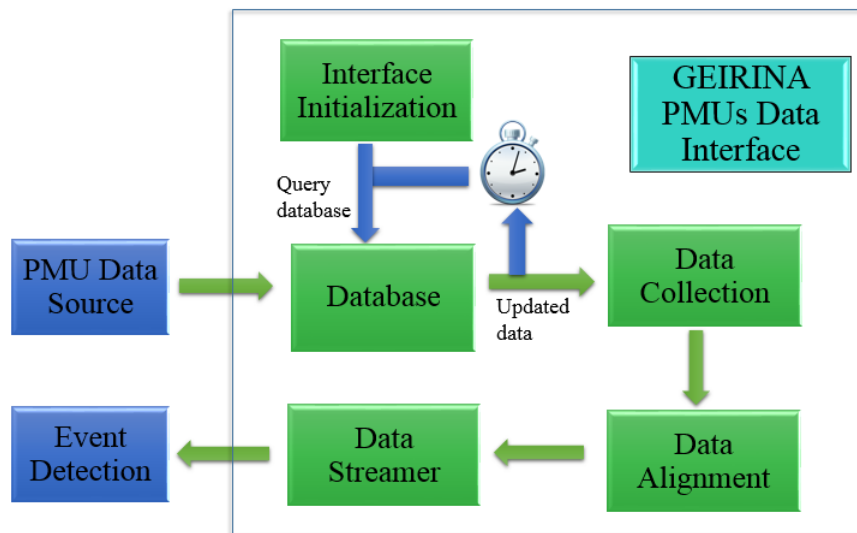


Figure 4-7. Data interface interacting with PMU database and event detection tool.

As shown in Figure 4-7. The PMUs data are archived in a given database every 1 minute. Once completing initialization, the GEIRINA PMUs data interface keeps refreshing and the database in a shorter interval than 1 minute. If the database is updated, there is new data written. The new measurements for each PMU are collected and aligned according to the timestamp for

the streamer. The streamer actions to stream the PMUs measurements to the event detection tool by frame. In each frame, it contains all the measurements from PMUs tagged with the same timestamps. In this condition, the detected event would have less than 1-minute latency because of the frequency to write PMUs measurements to the database. Currently, this program is completed with simulation measurements test.

Table 4-1. GEIRI North America testing results.

Case ID	Size (MW)	Truth		Estimation		Distance (Miles)
		Latitude	Longitude	Latitude	Longitude	
1	677	35.4792	112.5763	35.3792	112.6763	8.91
2	1167	31.7574	120.9782	31.8574	120.9782	6.89
3	412	32.0527	120.8062	32.0408	120.7681	2.38
4	728	32.2953	119.4118	32.1953	119.3118	9.04
5	1145	34.5958	119.1519	34.5958	119.0519	5.07
6	1000	32.2953	119.4118	32.1953	119.3118	9.04
7	1000	32.1726	119.5812	32.0726	119.5812	6.89
8	1000	32.2389	119.9298	32.2477	120.0341	6.14
9	660	34.0329	119.8586	34.0292	119.9906	7.58

Table 4-1 shows the detection and triangulation results of the testing cases. The simulation measurements of 9 trips of generation and system load are archived in the data for testing. Since the database is static, it reads all measurements data once and analyzes the measurements. All testing cases are successfully detected, and the event source estimations are listed in Table 4-1. It

can be seen the FNET/GridEye triangulation application functions to locate the disturbances with distance error from the truth less than 10 miles.

4.6 Conclusion

The extension of FNET/GridEye real-time power system monitoring applications benefits to improve regional situational awareness at utilities and ISOs. It is popularly welcomed by individual power utilities exploring the PMU measurement potentials. The package design of the applications facilitates to install at utilities using different data source conditions conveniently. Mostly it will run as an action adapter in openPDC if openPDC is available to collect streaming data from PMUs. Otherwise, it is necessary to develop individual data interface to fit in the application. The generation trip and load shedding detection and triangulation have performed well. Based on the platform, other applications will be further available for convenient installation, such as line trip detection, oscillation detection, etc.

During the implementations in several utilities and ISO for PMU use, it encountered some unprecedented challenges and discovered a wide range of opportunities available on PMU measurements. The applications can be further improved in terms of correctness and timeliness. Besides, new applications are explored to enhance power system situational awareness and operational resiliency.

CHAPTER 5 INTER-AREA OSCILLATION STATISTICAL ANALYSIS OF THE U.S. EASTERN INTERCONNECTION

5.1 Introduction

The inter-area oscillations in power systems have direct impacts on secure operation and reliability. Normally it involves two groups of generators swinging against each other at a low frequency, which can be observed over a large part of the power grids with non-linear dynamic behaviors. The inter-area oscillations can lead to severe system separations in the presence of a lightly damping mode. As renewables such as wind and solar are growing in power grids, several literatures have demonstrated that the penetration of renewables brings in unpredictable system disturbances, and has inelible impacts on the damping of existing electromechanical modes [61]-[64]. Further development of mixed generation resources involving more renewables would induce severer inter-area oscillations than before. Therefore, it is of significance to understand the changes of historical inter-area oscillations and take preemptive action to reduce the risk of equipment damage and system separation.

The inter-area oscillations threaten the stability of power systems. Timely detection can improve operators' situational awareness. A real-time inter-area oscillation detection tool has been developed and applied to the interconnections in North America at FNET/GridEye. With growing amount of disturbance sensors -- Frequency Disturbance Recorders (FDRs) installed in recent years, FNET/GridEye observes dynamic disturbance propagations [60]-[69]. This project aims at statistical analysis on the historical inter-area oscillations in Eastern Interconnection (EI) from 2013 to 2015 to discover the features of these oscillations. Since there are the most FDRs installed to provide comprehensive dynamics, EI is chosen for this study. Considering the FDRs

deployment in the recent three years is relative stable, the historical data during this time period is considered to be fair enough for comparison.

5.2 FNET/GridEye-detected inter-area oscillations

FNET/GridEye has been monitoring the interconnections in North America for more than ten years. It takes advantage of the low-cost, GPS-synchronized, and easy-installed FDRs to measure system phasors including frequency, voltage angle and voltage magnitude. The FDRs continuously capture system dynamics and transmit the data to the information center for storage and further applications [70]-[76]. Since the inter-area oscillations have a unique signature on phasors, FNET/GridEye is able to detect them by checking the phasor traces and analyze the oscillation modes according to the dynamics [77]-[80]. The detailed approach used to identify inter-area oscillation and modal analysis at FNET/GridEye is described in [81]. Once an oscillation is detected, it automatically alerts subscribers with a report of basic modal analysis results, including different oscillation mode, occurrence time, etc.

The dynamic stability of large interconnections is challenged now since the mixed generations and growing demand coupled with insufficiency transmission system investment. It leads to increasing unpredictability in power transfer. Secure system operation requires fast control responding to the oscillations according to system operations at particular hours and seasons. If the oscillations have a seasonal or hourly pattern, it is necessary to integrate the features with operation planning. Therefore, the hourly and monthly oscillation occurrence are analyzed in this project.

The basic approach of oscillation modal analysis decomposes the analog signal in time domain into frequency domain. According to the spectral information, each signal contains the components all over the frequency domain. However, the dominant mode is usually recognized

as the signal with the strongest spectrum power. The function equation 5-1 indicates the sum of cosine components fitted to the signal.

$$y(k) = \sum_{i=1}^n R_i Z_i^k \quad \text{Equation 5-1}$$

where the discrete signal $y(k)$ equals to the sum of the products of the residues or complex amplitudes R and the poles z . The parameter n denotes the number of sinusoids or modes to be estimated. The mode with maximum spectrum energy represented by the maximum residue value is considered as the predominating mode in the oscillation, because its damping and frequency determine the evolution of the oscillation. From components fitted to the signal, the damping and frequency estimates of the signal can be extracted from each z_i as shown in equation 5-2 and equation 5-3.

$$z_i = e^{\lambda_i \Delta t} \quad \text{Equation 5-1}$$

$$\lambda_i = \sigma_i \pm j\omega_i \quad \text{Equation 5-2}$$

The damping ratio σ_i and frequency ω_i are the main attributes of oscillation mode. In this project, the dominate mode frequency of captured inter-area oscillations at FNET/GridEye are analyzed. It is expected to work on the damping ratio in future work.

Usually, inter-area oscillations are accompanied by the occurrences of system disturbances. To some extent, it is able to identify some of the causes from the perspective of the phasor measurements. At FNET/GridEye, the captured inter-area oscillations are categorized into four major types, which are analyzed in this project.

5.3 Analysis of oscillation occurrence

This section mainly displays the occurrence of the captured inter-area oscillations by FNET/GridEye in EI from 2013 to 2015.

5.3.1 Hourly occurrence

The historical oscillations in each year are grouped into 24 hours according to their occurrence UTC time. Figure 5-1 shows the hourly occurrences of each year.

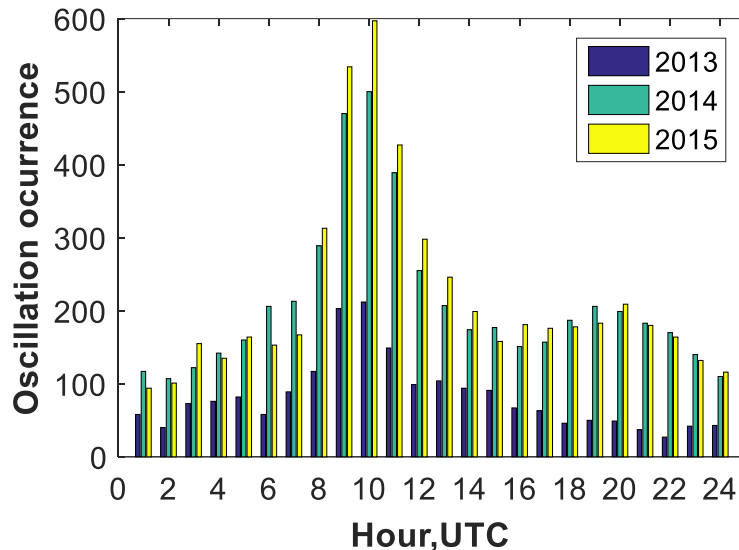


Figure 5-1. Hourly occurrence of oscillations in EI.

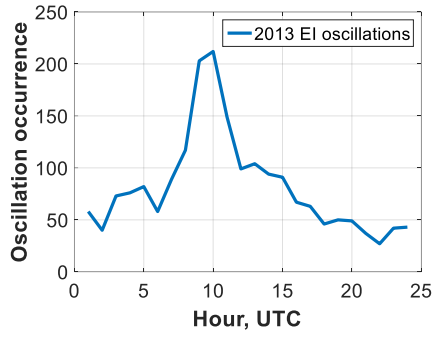
From the chart, it is noticed that from 2013 to 2015, there is an increasing trend in the number of oscillations. From 2013 to 2014, the total amount of oscillations increases from 1969 to 5031, then it slightly increases to 5260 in 2015. It is possible that there was significant change occurred in the system in 2013, like a large amount of renewable penetration, large area of network reconstruction, or other changes which made the system more vulnerable to oscillation disturbances [82]. However, it is just a suspicion according to the oscillation observations, and still needs evidence support from the power utilities.

Besides the increasing trend, it can be told from Figure 5-1 that during 8 am to 11 am UTC time, there are more oscillations detected using the same tool. The phenomenon is similar in

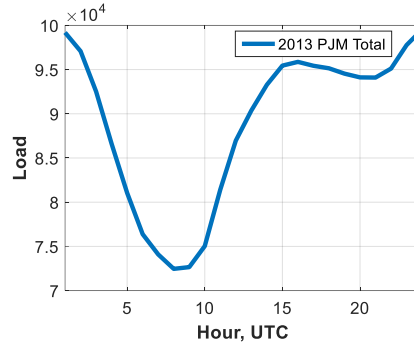
these three years. The oscillation occurrence envelope of each year in Figure 5-1 is compared with the daily load profile since the system load hourly pattern is commonly known. However, the daily load information of EI system is not available from public resources. Considering PJM is one of the biggest load centers in EI, the hourly oscillation occurrence is compared with the PJM daily load. The historical PJM daily load information is available at <http://www.pjm.com/markets-and-operations/ops-analysis/historical-load-data.aspx>. Because system load profile has seasonal characteristics, like summer peak, winter peak. The load value in each hour differs every day. Therefore, for each hour, the median value of the metered load through the year is used to compare with the cumulative oscillations happened in the same year. The results are displayed in Figure 5-2 to Figure 5-4.

The oscillation occurrences in Figure 5-1 are separated into three individual plots as shown in Figure 5-2 (a), Figure 5-3 (a), and Figure 5-4 (a). The corresponding PJM median load profile of each year are displayed in Figure 5-2 (b), Figure 5-3 (b), and Figure 5-4 (b), respectively. In each load profile plot, the time is converted to UTC time. From Figure 5-2, more than 100 oscillations are detected during 8 am to 11 am, which coincides with the load valley from the corresponding load profile, which is generally lower than 750MW. A similar phenomenon has also been found in 2014 and 2015. The small difference between the specific hour of minimum PJM load and the maximum EI oscillation occurrence possibly due to different systems.

The comparison indicates inter-area oscillation is highly associated with the system load. More inter-area oscillations are detected during the time periods when the system load is relatively lower. The phenomenon can also be explained that a disturbance can potentially cause more severe frequency deviations under light-load conditions.

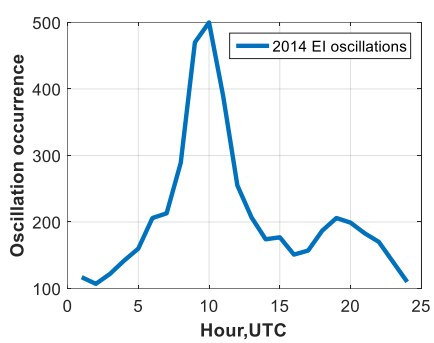


(a). oscillation occurrence.

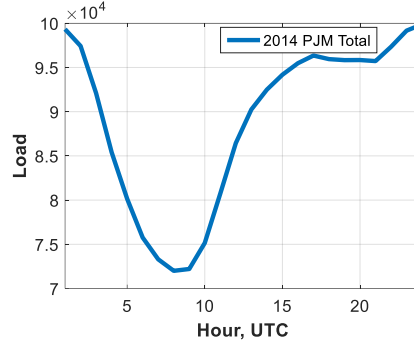


(b). PJM hourly load profile.

Figure 5-2. 2013 hourly EI oscillation occurrence curve and PJM load profile.

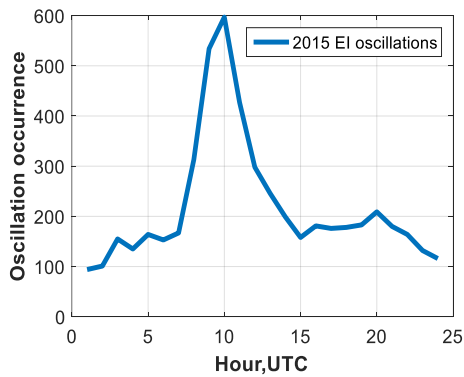


(a). oscillation occurrence.

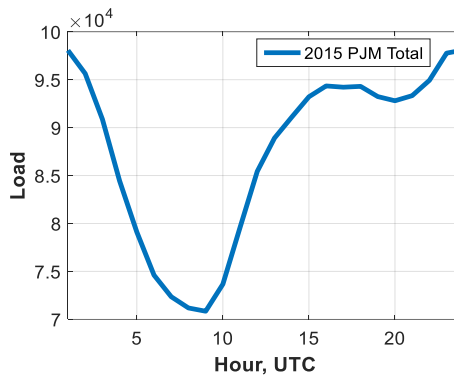


(b). PJM hourly load profile.

Figure 5-3. 2014 hourly EI oscillation occurrence curve and PJM load profile.



(a). oscillation occurrence.



(b). PJM hourly load profile.

Figure 5-4. 2015 hourly EI oscillation occurrence curve and PJM load profile.

5.3.2 Monthly occurrence

Likewise, the EI inter-area oscillations are grouped into 12 months according to their occurrence time. From Figure 5-5, it can be seen that the monthly occurrence in 2014 and 2015 are quite similar, and they are obviously different from 2013. In 2013, more oscillations happened in February, and the occurrences in other months become less than 200 times. In 2014 and 2015, the occurrences of oscillation in February are significantly decreased. The system is more vulnerable in October. Assuming the big system change took place in 2013 as suspected from the hourly occurrence analysis, it could explain the big difference between 2013 and 2014. After that, the system became steady and the oscillations occurred similarly between 2014 and 2015.

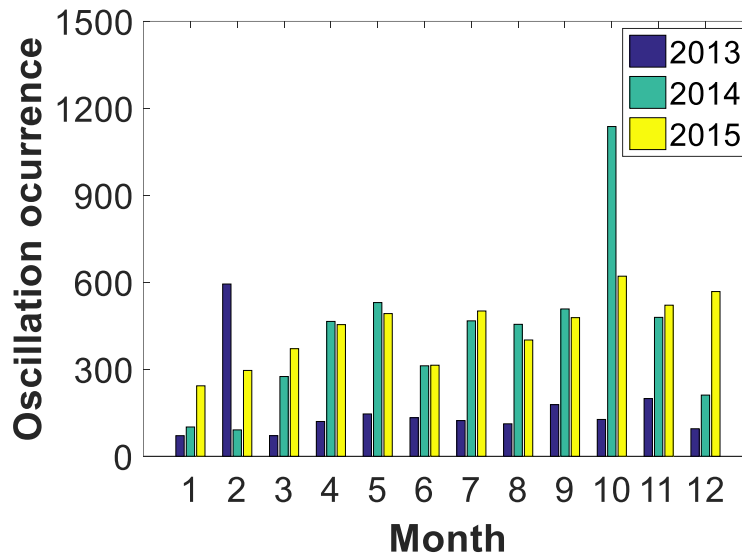


Figure 5-5. Monthly occurrence of oscillations in EI.

Comparing the occurrences of 2014 and 2015, it is noticed that during winter and summer peaks, the amount of oscillations is less than that in shoulder seasons, and there are more

oscillations in summer than in winter. It could be associated with the system load again. Because during peak months, the system load is relatively heavy. The same disturbance leads to less severe oscillations in winter and summer peaks than in shoulder seasons. Besides, the typical system demand in winter is higher than that in summer [83], so the system operates at lower risk of inter-area oscillations in winter than in summer. For now, the reason for the big change in October is unclear from the oscillation observations. The result has been reported to NERC to help find the reason.

5.4 Analysis of oscillation mode

According to the function in equation 5-1, an analog signal is composed of different modes over the frequency spectrum, each mode points to a cosine signal at one specific frequency. The dominant mode which contains the most energy is of general interest because it decides the evolution of the signal predominately. If the frequency of the dominant mode is close to the system natural frequency, the disturbance may lead to severe damages on both the generators and the system stability. Normally the frequency of inter-area oscillations in power systems ranges from 0.1 Hz to 1.2 Hz. FNET/GridEye detects inter-area oscillations in real time and analyzes the dominant mode using Matrix pencil method. The dominant frequencies of the captured inter-area oscillations are analyzed in this section.

In

Figure 5-6, the oscillations of each year are grouped into 24 hours according to their occurrence UTC time. The dominant frequency value of each oscillation is marked as a cross. It can be told from the plots that in each hour, the majority mode is less than 0.4 Hz. Most of them are overlapped around 0.2Hz. The appearance is less likely in high modes. Assuming 80% stands

for the majority of the oscillations, the 80 percentile frequency value describes the upper limit of the majority dominate mode. Therefore, Figure 5-7 displays the bar chart of the majority modes.

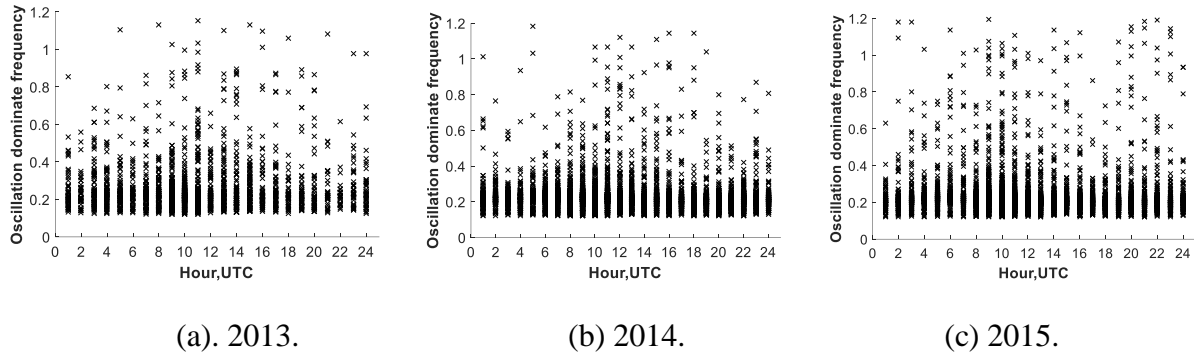


Figure 5-6. Dominate frequency of inter-area oscillations in EI.

The height of each bar means that 80% of the oscillations happened in the specific hour are in modes less than the corresponding frequency. It is noticed that in different hours, the upper limit of the majority oscillation modes in 2013 varies widely from 0.25 Hz to 0.42 Hz. However, in 2014 and 2015, the envelope of 80 percentile became steady and decreased. 80% of the oscillations are in the modes lower than 0.25 Hz. The difference between 2013 and 2014, and similarity between 2014 and 2015 support the suspicion made previously that big system change occurred in 2013, which made the system oscillation performs differently.

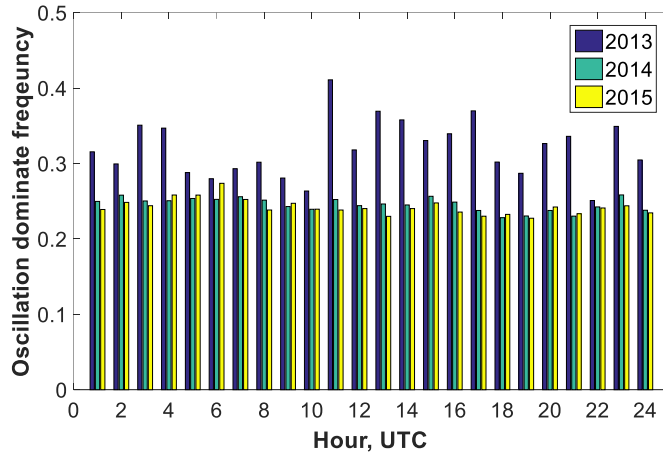


Figure 5-7. Hourly 80 percentile dominate frequency in EI.

The dominant frequency is further analyzed from another perspective by considering all the oscillations happened in the same year as a whole. Figure 5-8 presents the dominate frequency distributions of the same objects.

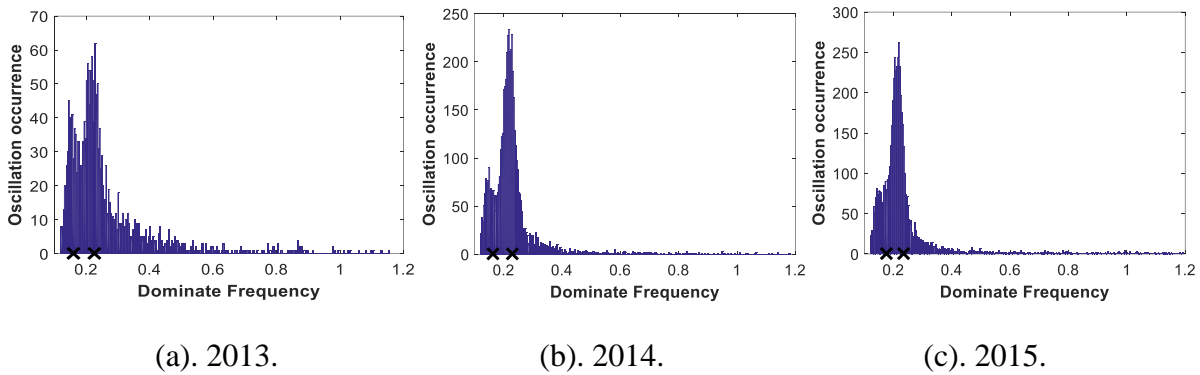


Figure 5-8. Dominate frequency distribution of EI.

Each plot shows the distribution of the dominant frequency in one year. The x-axis is the frequency, and the y-axis is the oscillation occurrence. It is easy to find that there are two obvious peaks in each plot, which indicates that mostly the oscillations in this year are in these modes. By using clustering technique, the centroids of the peaks are discovered, and listed in

Table 5-1. Recent years, the most often oscillation modes in EI are around 0.16~0.17Hz and 0.22~0.23 Hz, and they have been gradually increasing.

5.5 Analysis of oscillation types

There are all kinds of reasons inducing inter-area oscillations across the entire power system. They could be sudden event like the trip of generator or tie line, or common power system operations. Some of the causes are easy to be recognized, while some are not. By comparing the frequency before and after the disturbance, the oscillations captured at FNET/Grid are grouped into four categories according to the possible reasons: generation trip, load shedding, line trip, and non-obvious reasons, which includes other reasons not belonging to previous three. The non-obvious reasons are usually hard to be interpreted from phasor measurements. The dynamics of oscillations caused by the 4 types are described in detail in [69] [84]. Here, this chapter focuses on the statistical analysis of the oscillation occurrence of the four types. Figure 5-9 shows the oscillation occurrences of different types happened in 24 hours in each year.

Table 5-1. Dominate frequency of inter-area oscillations in EI.

EI oscillations (year)	Dominant Frequency Centroid 1 (Hz)	Dominant Frequency Centroid 2 (Hz)
2013	0.1604	0.2257
2014	0.1636	0.2299
2015	0.1739	0.2343

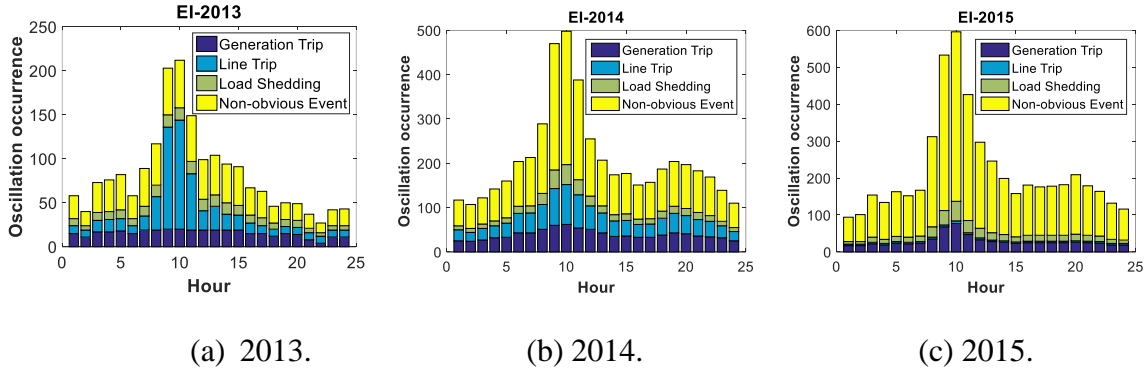


Figure 5-9. Occurrences of EI oscillations in different types.

In Figure 5-9 (a), it shows that in 2013, during light load hours, from 8 am to 11 am, more oscillations are caused by line trips. Comparing Figure 5-9 (a) with Figure 5-9 (b) and Figure 5-9 (c), it is noticed that in 2014 and 2015, the number of oscillations caused by non-obvious reasons is significantly increased, especially during the light-load hours. The significant difference supports the suspicion that great changes took place in EI in 2013. On the other hand, the portion of line trip caused oscillations is decreased gradually. The system may have better reaction to stabilize disturbances caused by line trips. Since a large portion of the oscillations are the non-obvious type, which means the reasons are not clear using current algorithms. Further research has been prompted to discover the reasons for these oscillations.

5.6 Conclusion

This project achieves a preliminary statistical analysis on the inter-area oscillations occurred in EI system from 2013 to 2015 according to the observations at FNET/GridEye. The major analysis is conducted on the oscillation occurrence, the dominant frequency, and the oscillation type. According to the results, large system change, possible network reconstruction, or high penetration of renewables took place in EI during 2013, which led to the significant

changes on different aspects of the oscillations between 2013 and 2014: The number of oscillations significantly increased; the pattern of the oscillation mode frequency distribution changed obviously; and the predominating reason of inter-area oscillations is shifted from line trip events to other reasons except for generation trip, load shedding. The association between inter-area oscillation and the system load is discovered that the system running with a light load is more vulnerable to inter-area oscillation than under high load conditions. Two most often dominate modes in EI are found around 0.16~0.17 Hz and 0.22~0.23 Hz, and they have been gradually increasing in recent years.

It is inspired by the benefits of this study to conduct the research on other large interconnections. Besides, it prompts some new questions that are potential to make some valuable discoveries. For example, besides the line trip, generation trip, and load shedding, what is the major reason for the oscillations in EI system?

CHAPTER 6 FNET/GRIDEYE REAL-TIME SUSTAINED OSCILLATION DETECTION

6.1 Introduction

FNET/GridEye has been collecting real-time phasor measurements for over ten years, and several applications have been developed and implemented to detect various system disturbances in real time, such as sudden loss of power supply, large load shedding, inter-area low-frequency oscillations, and system islanding events, etc. Table 6-1 lists the current effective applications at FNET/GridEye. At the end of the list, the sustained oscillation trigger is a newly developed application. It functions to detect inter-area sustained oscillations. This chapter elaborates the methodology and implementation of the application at FNET/GridEye.

6.2 Frequency-based sustained oscillation detection

Modern power systems are progressively more interconnected on transmission networks and more interactive with distributed renewable generations in distribution networks due to increasing power demand. The situation creates more technical challenges in the context of oscillations. Sustained oscillations have emerged in power grids worldwide threatening secure operations [84]. Besides the conventional poorly or negatively damped oscillations caused by insufficient system damping, there are forced oscillations caused by small and periodic external faults. The properties and behaviors of these two oscillations are well described in [85] [86]. This chapter proposes a situational awareness application for fast real-time detection of sustained oscillations, which broadly refers to conditions including the poorly damped natural oscillations, forced oscillations caused by cyclic inputs, and the resonance between poorly damped system mode and small cyclic mode.

Table 6-1. Effective applications hosted by FNET/GridEye.

ID	Application	Description
1	Event Trigger	Detects generator trip and load shedding by continuously monitoring the ROCOF of the incoming frequency data
2	Inter-area Oscillation Trigger	Detects inter-area oscillation by monitoring the relative phasor angle
3	Islanding Trigger	Detects the situation in which a part of the grid becomes electrically isolated from the remainder of the power system
4	Line Trip Trigger	Detects a line outage event by monitoring sudden change but quickly damped frequency feature on local units
5	Ambient Mode Analysis	Continuously analyzes system ambient oscillation frequency and damping ratio in real-time
6	Real-time Data Visualization	Web-based real-time data display in table, trend, and map format
7	Event Location	Estimates generation trip or load shedding event location using TDOA algorithm
8	Frequency Response Analysis	Analyzes frequency excursion during events, estimates events MW amount, point A,B,C frequency etc.
9	Oscillation Mode Analysis	Estimates inter-area oscillation frequency, magnitude and damping ratio for dominate modes
10	Online Report	Generates web-based online analytics reports for detected disturbances
11	Email Alert	Sends Email alert messages to registered customers about detected disturbances in real-time
12	Event Video Replay	Automatically generates animation video for disturbances
13	Sustained oscillation trigger	Detects a sustained oscillation across the entire interconnection using phasor measurements

If the electromechanical eigenvalues of the system are stable, the conventional oscillations will damp and the system will converge to a new stable status. We term these “natural oscillation”. Actions can be taken to suppress the natural oscillations, such as installing Power System Stabilizer (PSS), constructing new transmission lines, reducing gains of exciters on strongly related generators, etc. On the other hand, “forced oscillation” refers to a type of system response to cyclic inputs often brought about by prime mover pressure pulsation, malfunction of PSS, periodic load disturbances, etc. Forced oscillations response to the disturbances quickly, and terminate immediately once the disturbances are withdrawn. Besides zero or negative damping natural oscillations and large magnitude forced oscillations, small cyclic input coincidentally at the mode nearby a weakly damped system mode results in the resonance of generation output at a much larger magnitude than the input, which is also of paramount concern to secure operations. Due to their common sustainability property, These situations are termed as sustained oscillation.

Several approaches are proposed to detect and analyze the sustained oscillations [87]-[93]. Reference [87] distinguishes the features of lightly-damped natural oscillations from forced oscillations using spectral analysis on the frequency responses. The forced oscillation would influence the estimation accuracy of the natural mode [88]. It requires separation of the sinusoid and noise responses. Forced oscillation responses of a multi-machine power system are expressed in [89]. The resonance between forced oscillations and inter-area oscillatory modes are discussed in [90], which affect the mode analysis of some measurements based methods. It is proposed in [91] to detect forced oscillations with mode analysis and time localization methods using PMUs measurements. The periodograms of PMU measurements are compared with thresholds, which are selected corresponding to the probabilities of detection and false alarms.

The forced oscillations perform high energy at a certain mode in the periodograms [92]. Forced oscillation frequency in mixed responses to multiple events. It is limited to detection of forced oscillations with frequencies distinct from natural electromechanical oscillations. Reference [93] proposed self-coherence, which terms the coherence spectrum between a signal and its time-delayed signal, method to detect forced oscillations in the power systems.

Above mentioned typical detection and localization approaches are based on PMU active/reactive power measurements. However, the PMU measurements from transmission networks are usually highly confidential for the sake of system security. In the context of FNET/GridEye, the active power measurement is not available since the frequency is measured at distribution networks. Therefore, the approach proposes another way using distribution networks synchrophasor measurement to detect inter-area sustained oscillations.

6.3 Theoretical background

A power system response could be typically separated into three components: ambient, transient, and forced responses [89]. Excited by normal low-amplitude stochastic variations, such as random load variations, the response is named as ambient response. The transient response is typically caused by a sudden trip, as the loss of power supply or demand, or fault, as a short circuit of the transmission line. Forced response corresponds to a cyclic input and is superimposed with the other two. The dynamics properties are typically analyzed by linearization of the operation dynamics. The linearized state equation of a power system can be described as in equation 6-1.

$$\dot{x}(t) = Ax(t) + b_1f(t) + \sum_{k=1}^M b_{2k}q_k(t) \quad \text{Equation 6-1}$$

where A is the state matrix, t means time, $x(t)$ represents the system state vector and N is the number of system states. Normally the system state vector refers to the velocity and angle of machine rotors. $Ax(t)$ is the response to zero-state. $f(t)$ is a periodical input exciting a forced

oscillation. $q_k(t)$ is a random zero-mean Gaussian input which is typically considered as noise produced by random load variations. The overall system response has three components: 1) the transient response caused by the system original operation; 2) the forced response due to $f(t)$; 3) ambient response caused by white noises.

Let's assume the forced input $f(t)$ is sinusoidal at frequency w_0 as equation 6-2.

$$f(t) = \sum_{m=1}^{\infty} 2|A_m| \cos(mw_0t + \angle A_m) \quad \text{Equation 6-2}$$

where $A_m = A_{-m}^*$ and $A_0 = 0$. If $f(t)$ is plugged into equation 6-1, the solution becomes equation 6-3.

$$x(t) = \left[\sum_{i=0}^N u_i v_i x(0) e^{\lambda_i t} \right] + \sum_{m=-\infty}^{\infty} \left[\left[\sum_{i=1}^N u_i v_i b_1 e^{\lambda_i t} \right] \otimes A_m e^{jm w_0 t} \right] + \sum_{k=1}^M \left[\sum_{i=1}^N u_i v_i b_{2k} e^{\lambda_i t} \right] \otimes q_k(t) \quad \text{Equation 6-3}$$

where λ_i is the i th eigenvalue ($i = 1, \dots, N$); u_i is the i th right eigenvector; v_i is the i th left eigenvector; \otimes is convolution operator and $j = \sqrt{-1}$. The first term is the transient response, the second term is the forced response, and the third is the noise response. If the forced input $f(t)$ is zero and a given system mode is zero or weakly damped, the natural oscillation is sustained. If the cyclic input is non-zero, and the system is asymptotically stable, the response is a forced oscillation.

Furthermore, when an inter-area mode is poorly damped, meanwhile a forced disturbance is injected at a frequency close to the system mode at a location where the inter-area mode is strongly involved, a resonance can happen to lead to a sustained oscillation that has much larger magnitude than the input [90]. No matter of forced oscillations driven by cyclic disturbances, or resonance between system mode and external disturbances, or poorly damped low-frequency oscillation, their frequency responses have the same characteristics: 1) weak or negative damping; 2) long-lasting;

3) large oscillation magnitude. The generators are sustained oscillatory. The sustained oscillatory power output threatens the stable operations.

Periodical signals usually present a couple of distinct characteristics in Power spectral density (PSD) [92]. PSD answers how much energy a signal is distributed in the frequency domain. A stationary time-series signal with white noises typically has PSD evenly distributed. If the PSD shows significantly high energy located at a specific frequency, it means the signal is periodically repeated at this frequency. Of course, a signal could be composed of multiple periodical signals. In that case, multiple spikes could be conspicuous in the PSD curve. PSD is often used to detect deterministic sinusoids in time-series signals [94]. In this project, the PSD of time-series synchrophasor measurements is used to indicate the paramount energy at the oscillation dominant mode.

6.4 Sustained oscillation signature

In a real-time application, it searches for the measurement satisfying all signature characteristics of the objective disturbance. With understanding sustained oscillation in theory, this section further studies the response dynamics to sustained oscillations in simulation result and practical measurement in order to disclose the signature.

A library of simulation cases is developed by the authors of [95], who intentionally designed poorly damped oscillations and forced oscillations in a reduced WECC 179-bus, 29-machine system. Detailed model information, simulation results are available at [96]. The system has a natural mode at 0.86Hz. According to simulation results, it is noticeable after the oscillation is completely formed, multiple bus voltage angles change in a clear sinusoidal shape with 1) large magnitude; 2) poor damping ratio, and 3) long durations. The primary concern of sustained oscillation is its long-lasting and poor damping. Furthermore, the practical

measurements of real sustained oscillation dynamics are used to illustrate the signature characteristics.

A nuclear unit in Eastern Interconnection was running at 700 MW prior to its trip around 08:00 am UTC time on June 17th, 2016. According to the synchrophasor measurements at FNET/GridEye, the frequency response to this disturbance is presented in Figure 6-1.

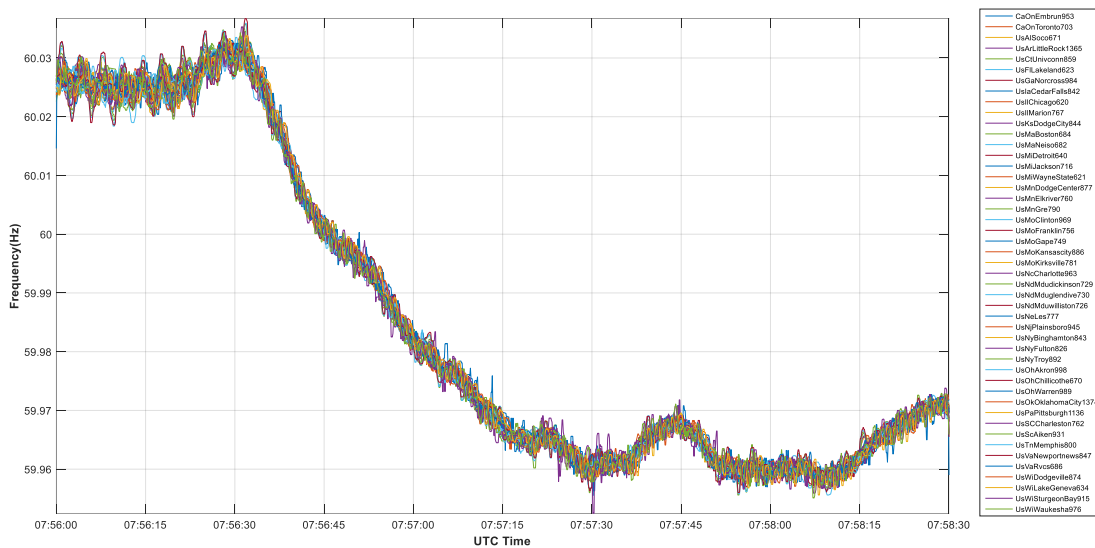


Figure 6-1. Frequency response to the unit trip.

In Figure 6-1, each curve is made from the measurements of an individual FDR installed in Eastern Interconnection. Because of the synchronism of system frequency, and there are over 100 available FDRs in this figure, the curves are tangled together. Even though, it is noticed that, around 07:56:32 UTC time, the frequency started to decline quickly, which represents the occurrence of the unit trip. Moreover, there are oscillations on several FDRs ahead of the unit trip. Therefore, the FDRs frequency measurements before this unit trip are analyzed, and several

sustained oscillations are discovered. Their frequency responses are shown in Figure 6-2 to Figure 6-4, where the same FDRs as in Figure 6-1 frequency measurements are displayed.

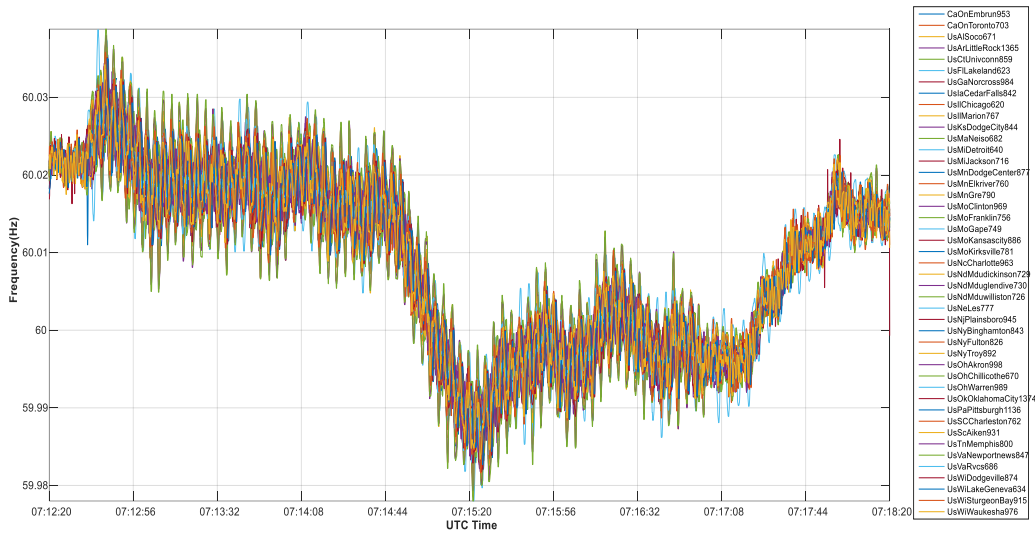


Figure 6-2. Sustained oscillation predominant mode @ 0.2739 Hz.

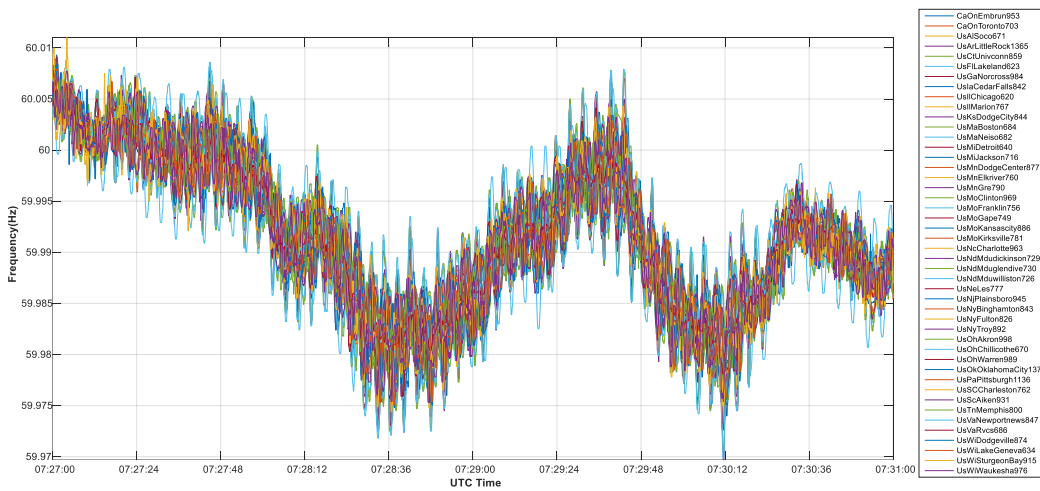


Figure 6-3. Sustained oscillation predominant mode @ 0.2524 Hz.

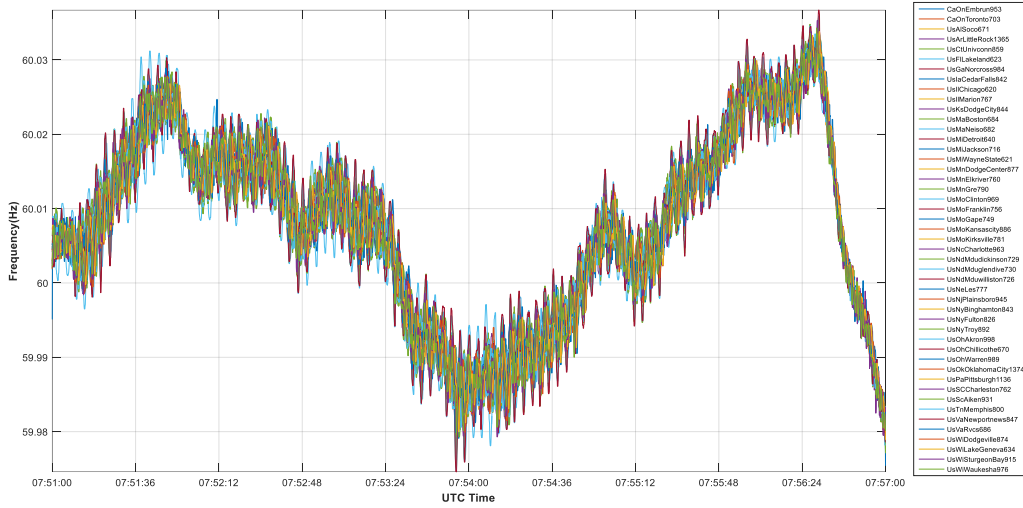


Figure 6-4. Sustained oscillation predominant mode @ 0.2695 Hz.

It can be seen from Figure 6-2, a large magnitude and poor-damping oscillation was initiated at 07:12:40, and lasted about 5 minutes. By mode analysis on this period of frequency using Matrix Pencil method, which is a typical method for oscillation mode analysis, the dominant oscillations mode is 0.2739 Hz. In Figure 6-3 and Figure 6-4, the long-term, large magnitude and weekly damping sustained oscillations are noticeable in the modes of 0.2524 Hz and 0.2695 Hz. It demonstrates in real synchrophasor monitoring, the frequency response to sustained oscillations performs the same three characteristics as in simulations: 1) large magnitude; 2) poor damping; and 3) long duration. Therefore, the application is proposed to detect sustained oscillations according to these characteristics.

6.5 Detection of sustained oscillation

From the perspective of wide-area monitoring, some of the oscillations are negligible in magnitude and submerged by white noise exhibiting a very clear sinusoidal waveform in

synchrophasor. According to the theoretical background and examples of simulation and real measurement, sustained oscillation exhibits a very clear sinusoidal waveform in both angle and frequency signals. Since phase angle is the integration of frequency deviation from the nominal value (60Hz) over time, the angle data also demonstrates dynamic behaviors before and after disturbance. As the integral of frequency deviation over time, a small change in frequency will cause relatively large changes in angle measurement, a better signal-to-noise ratio (SNR) will be obtained on angle measurement. A better performance is expected for angle-based event search. Therefore, the application proposed in this project selects to use the voltage angle measurement. In the context of sustained oscillation signatures concluded above, Figure 6-5 explains the criteria of the sustained oscillation detection schema based on the phasor angle.

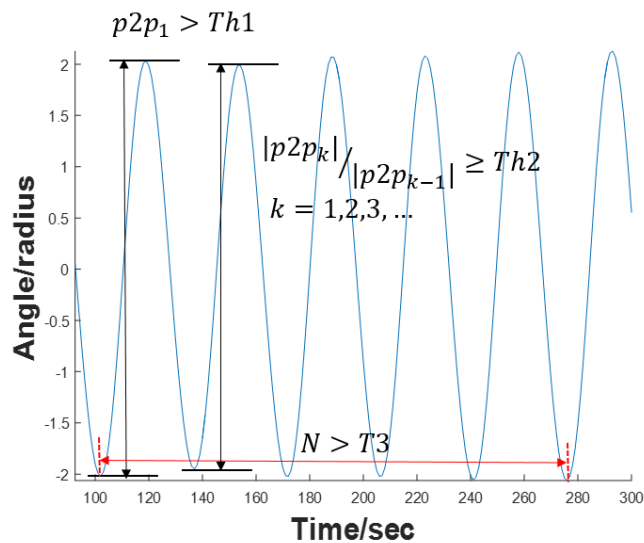


Figure 6-5. Sustained oscillation detection criteria.

First, the peak-to-peak value higher than a predefined threshold represents a distinct magnitude of paramount. The second criterion is the poor damping ratio. Typical mode analysis

is able to conclude the damping ratio. However, the mode analysis takes computing resources and time to be executed and results in delay. Therefore a phase angle envelope approach is proposed to catch low damping ratio oscillations. The third criterion is long-lasting of the poorly damped wavelet. An envelope band is applied to the angle data stream, as shown in Figure 6-6 to get the upper and lower envelopes by connecting local maxima/minima of the data stream. The bandwidth is then calculated to estimate the oscillation magnitude. By setting an appropriate time interval for envelope computation, the damping ratio will be considered as poor if the envelopes show that the bandwidth of current cycle versus the previous cycle is high.

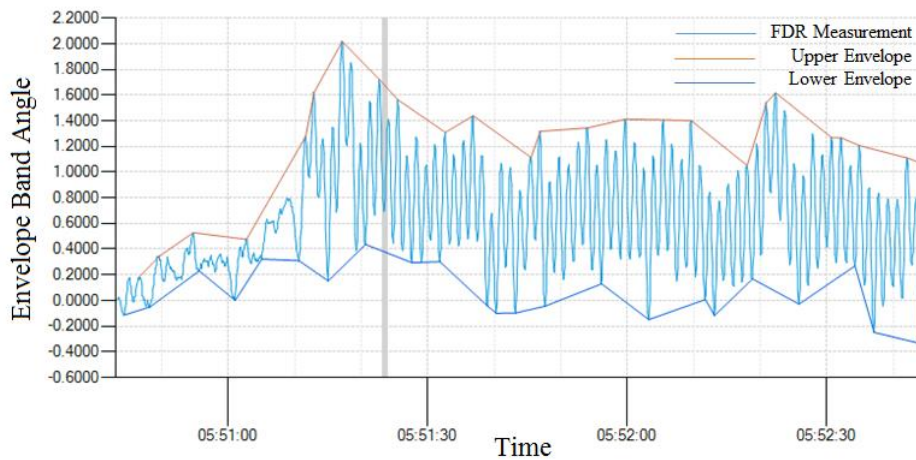


Figure 6-6. Envelope band of phase angle measurements.

Considering the propagation of electromagnetic wavelet, the oscillation magnitude varies in different areas. To determine a proper threshold for a specific area, a real-time statistics algorithm is applied to the data stream of each area to dynamically get the probability distribution of the angle envelope bandwidth. Then the threshold is set to a value such that the probability of envelope bandwidth larger than the value is 0.005, as shown in Figure 6-7. If the

envelope bandwidth keeps larger than the threshold for a while long enough, which satisfies the third property, the signal may sense a sustained oscillation. Further confirmation will be made by PSD analysis, which typically shows a clear peak at a certain frequency as shown in Figure 6-8.

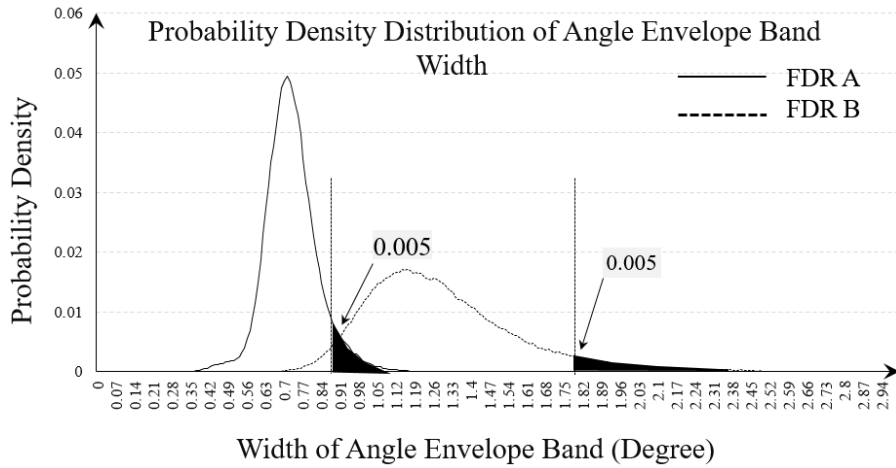


Figure 6-7. Calculation of threshold based on statistics of angle envelope bandwidth.

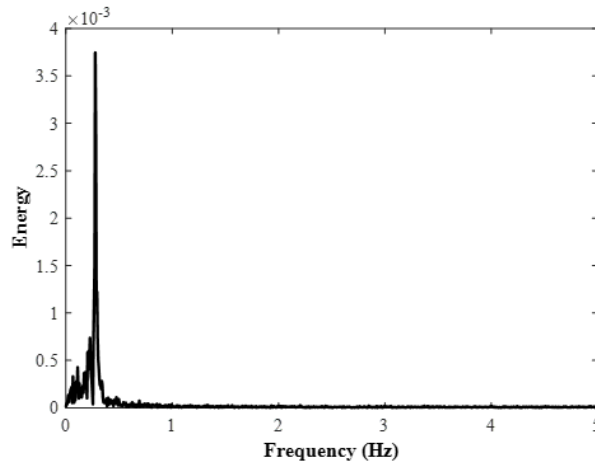


Figure 6-8. PSD of a sustained oscillation example.

The flowchart of the application is presented in Figure 6-9. In the raw data conditioning, a couple of filters are utilized for data conditioning [97]. One is a moving median filter to remove the white noises in the raw data. The second one is a moving mean filter to get the data trend. By eliminating the data trend, the rest of the signal becomes zero-mean. The deviation becomes distinct when the oscillation is formed. The signal of interest is the sustained oscillation, so de-trending is necessary to remove the effects of the data trend and maintain the oscillatory part at the same time.

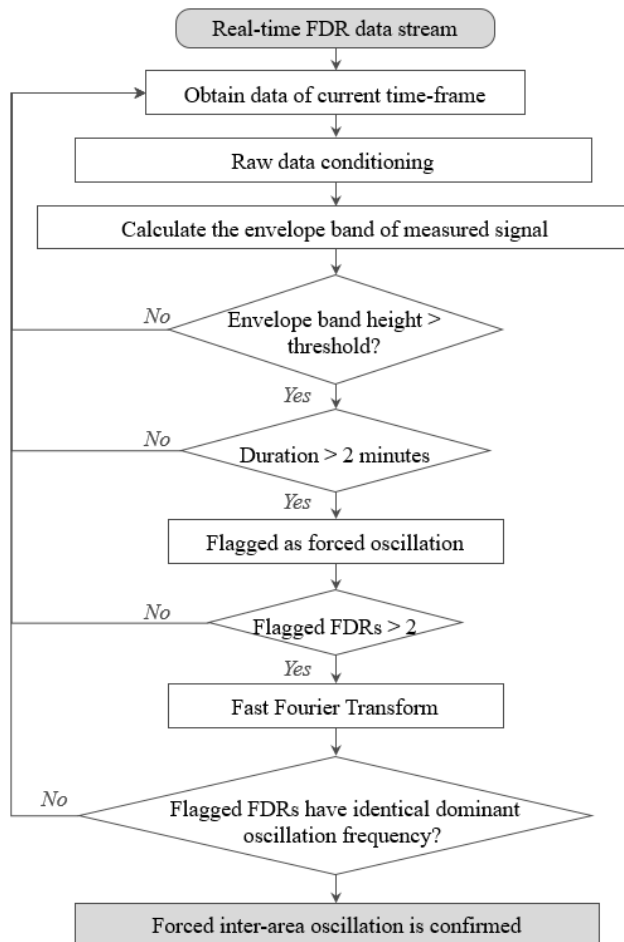


Figure 6-9. Flowchart of the sustained oscillation detection at FNET/GridEye.

Figure 6-10 displays an observed sustained oscillation disturbance happened in EI system. The raw measurements are smoothed via the moving median filter, and the moving mean filter extracts the trend of frequency. The de-trended measurements are all added with 60 Hz in order to show the variations along with others curves in the same chart. In the de-trended curve, the oscillation is conspicuous. Before the occurrence, the curve fluctuates randomly. After that point, a clear sinusoidal wavelet is formed with oscillation magnitude of each cycle above a certain value.

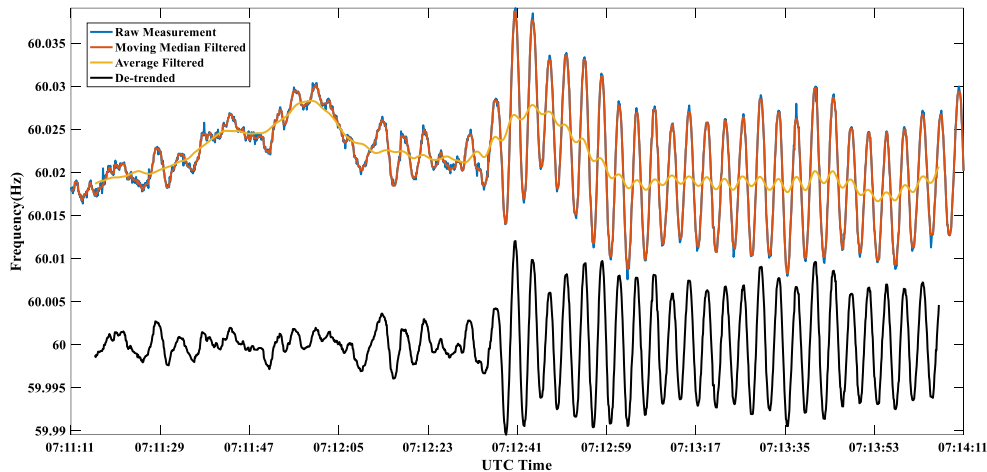


Figure 6-10. De-trending frequency of a sustained oscillation.

After data conditioning, the envelope band of each signal is calculated. If the bandwidth is above a predefined threshold, the first criterion is satisfied. If the duration of large bandwidth is longer than a threshold, it means the oscillation has lasted long with magnitude (envelope bandwidth high than the threshold). The second and third signature properties are both satisfied. An inter-area sustained oscillation often has influences on the grid in a large area. If the signature is found on only a single FDR, there is a possibility that it is caused by data quality issue or local

oscillation. However, if there are multiple FDRs observing the sustained oscillation almost at the same time, it would be more confident to make a decision of a sustained oscillation. Therefore, a voting scheme is used in this application. At the end, Fast Fourier Transform (FFT) is conducted for PSD analysis, which is able to confirm the sustained oscillation mode.

6.7 Verification of sustained oscillation detection

According to the approach described above, an offline application coded in Matlab is developed to test historical sustained oscillations. An individual real-time application coded in C# is being developed to detect sustained oscillations on openPDC platform. Because the occurrence of sustained oscillations is not often, here in this section, the offline Matlab application is introduced. Based on the historical measurements, parameters and thresholds are decided. The median window size is set to be 7 points, while the size of the average filter is set to be 100, the minimum peak-to-peak magnitude is set to be, the ratio between adjacent cycles is set to be, the minimum oscillation lasting time is set to be. The highest PSD energy is at least. This group of setting succeed to detect a sustained oscillations occurred in Eastern Interconnection.

The detected sustained oscillation happened on December 27, 2016. The frequency measurements from all FDRs installed in Eastern Interconnection are displayed in Figure 6-11. It is noticeable around 05:51:12, an oscillation was initiated and its amplitude is barely damped. It can be seen that a sustained oscillation in wide-area is able to be observed at different locations.

Figure 6-12 shows the raw measurements, the measurements after moving median filter, average filter, and the de-trended measurements of one FDR installed in Oak Ridge, Tennessee. Similarly, the de-trended measurements are all added with 60Hz in order to be displayed in the chart. It clearly indicates the formation of the oscillation. Apparently, the de-trended curve becomes zero-mean variations and the peaks of sustained oscillation are evenly distributed above

and below 60Hz as the black curve shown in Figure 6-12. The PSD of the de-trended frequency in

Figure 6-13 indicates significantly high energy at 0.70Hz.

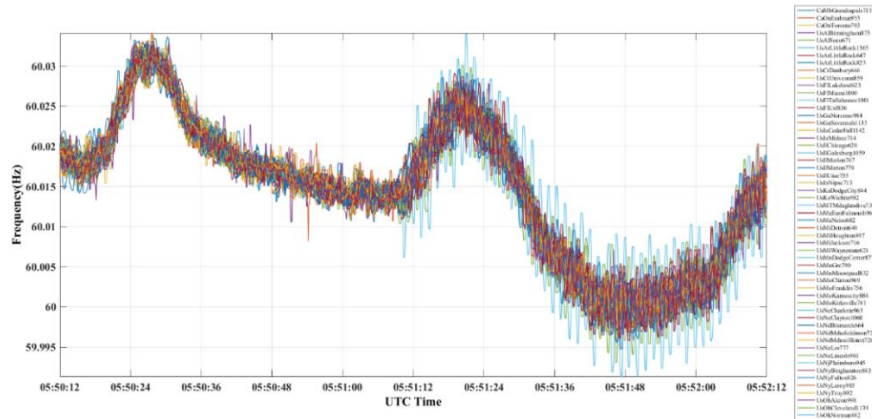


Figure 6-11. Raw frequency measurements from all FDRs for the testing case.

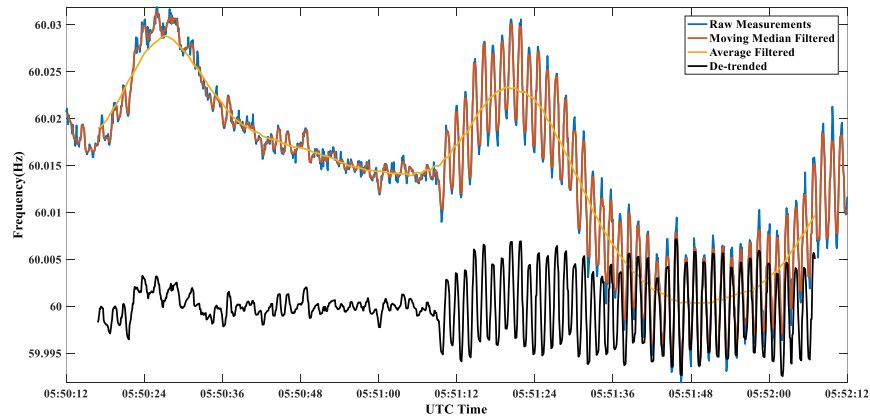


Figure 6-12. Processed frequency of the testing sustained oscillation.

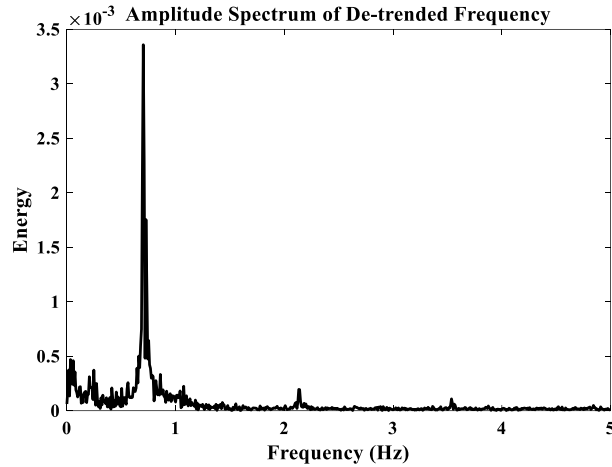


Figure 6-13. Periodogram analysis of the testing sustained oscillation.

6.8 Conclusion

This project proposed an algorithm for detecting sustained oscillations using FNET/GridEye synchrophasor measurements and the implementation of a real-time frequency-based application on the basis of openPDC platform. Based on the simulation results and real measurements, three principle characteristics are concluded as the signatures of sustained oscillations. The application searches for synchrophasor dynamics which contains the three characteristics at the same time. Testing results show effective detections of sustained oscillations. The voltage angle measurements are the integration of frequency deviation from the nominal value. Theoretically, the angle measurements are able to be used in the application as well.

CHAPTER 7 ELECTRIC CLOCKS TIME SYNCHRONIZATION BASED ON GRID FREQUENCY

7.1 Introduction

Self-driving vehicles have become a popular technique in modern life. It sets drivers free from the exhaustion of long-term high concentration in driving and allows them to enjoy the road view without much attention on the traffic. Besides, it benefits saving the gasoline to some extent by automatic stop and restart the engine according to the predictable traffic signal. One of the critical techniques is the prediction of the traffic signal, which tells how many seconds left the signal turns green. The traffic signal schedule can be told by a solid communication infrastructure between the auto smart system and the city traffic signal control center. Audi's cars are now able to indicate the status of next coming traffic signal. It's the first commercial offering of vehicle-to-infrastructure communication in the United States. However, accurate prediction is of the utmost significance in this technique. Even though there is just one-second error, it still risks human life. One of the error comes from the power grid that the traffic signal controller is particularly connecting to.

7.2 Electric Clocks

Typically the traffic signals are powered by the local electricity lines, which provide energy to light up the signals and its control and communication systems. Regarding the clocks counting second in the control systems, there might be thousands of types of clocks in millions of traffic signals. Here the most typical ones depending on the electricity are discussed because it is the most simple, easy and cheap way. There are generally 3 types of counting schemas applied in electric clocks.

1) Frequency divider [98]:

By applying frequency divider, the AC power frequency is reduced from 60/50 Hz to 0.5 Hz. The block diagram of this type of synchronous clock is shown in Figure 7-1. Every time the AC current/voltage waves across zero, it adds 1 second. For clocks connecting with US grid, every time adding one second, the actual second is $(f/60)$ seconds.

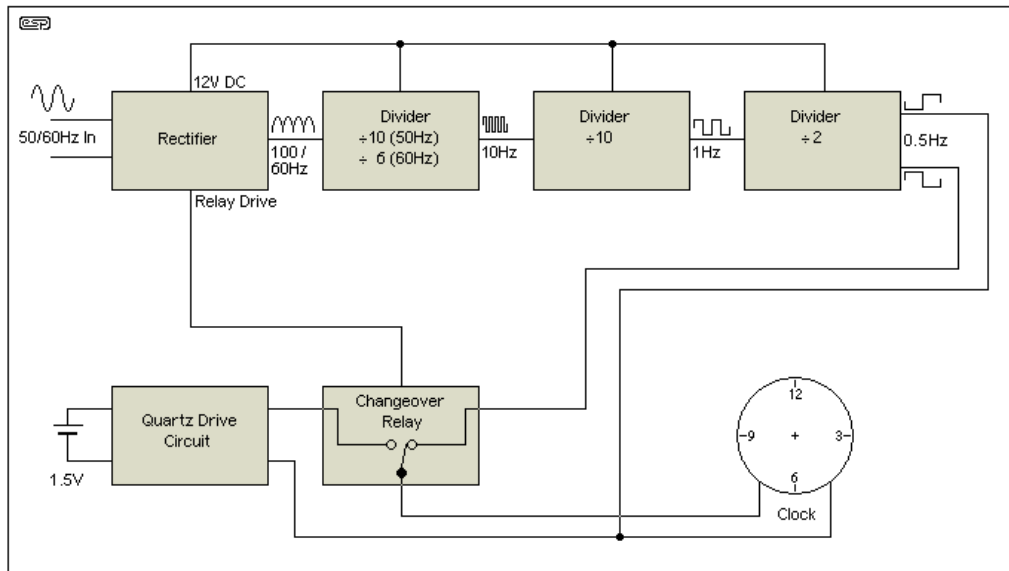


Figure 7-1. Block diagram of the synchronous clock.

2) Cycles counting: The second schema is to count AC current across zero accumulatively. Every continuously across zero twice, it is counted as 1 cycle. Every continuous 60/50 cycles are recognized as 1 second forward, then the clock is added one second. In this case, for clocks connecting with US grid, the actual time for adding one second is $(f/60)$ second.

3) Small size of synchronous rotating motor [99]. Driven by AC power, the rotation of the shaft is synchronized with the frequency of the supply current. The rotation period is exactly equal to an integral number of AC cycles. The stator of the synchronous motor creates a

magnetic field which rotates in time with the oscillations of the line current. The rotor with permanent magnet or electromagnet turns in step with the stator field at the same rate and as a result, provides the second synchronized rotating magnet field of an AC motor. The Figure 7-2 is the typical synchronous motor from a microwave oven.



Figure 7-2. Small synchronous motor from microwave ovens.

The rotating speed of the synchronous motor is synchronized with the power grid frequency. It is given as equation 7-1.

$$N = 120 * \frac{f}{p} \quad \text{Equation 7-1}$$

where f is the power frequency. N represents the rotation speed in rpm, and p stands for the number of pole per phase. The rotation speed designed by the manufactures is displayed on the surface of the motor. Applied in electric clocks, it counts the rotation and adds one second when the rotation cycles reach the amount as designed. Eventually, the motor recognizes $f/60$ as one second.

Although there are multiple mechanical schemas of electric clocks, the basic principle associated with electricity frequency is that $f/60$ is recognized as 1 second in the clock. If the frequency is ideally stable at 60 Hz, the clock is working on time. If the frequency is higher than 60 Hz, which means there would be more cycles in one second. However, the schema of clock can't recognize the change. The clock would be faster than the correct clock. Vice versa, if the frequency is lower than 60 Hz, there would be less than 60 cycles in one second. The clock would wait until the cycles reach 60 to add one. So the clock would be slower than correct clock.

7.3 Time drift caused by power frequency

According to above discussion of electric clocks in traffic signal systems, the counting seconds are influenced by the accumulative frequency deviation. Because of the frequency fluctuation around the nominal frequency value, the clock does not run at exactly the same rate as a reference clock [100]. After a period of time, the clock drifts apart or gradually desynchronizes from the others. The drift caused by frequency fluctuation is invisible. Here is this chapter, it is proposed to estimate the time drift by using FDR frequency measurements at FNET/GridEye.

7.3.1 Time drift calculation

Based on the discussion of the electric clock schemas above, the time of the electric clocks can be calculated according to equation 7-2.

$$t = T_0 * f/f_0 \quad \text{Equation 7-2}$$

where T_0 is the interval of the measurement samples. The FDRs collect phasor measurements at a rate of ten points per second, T_0 is 0.1 second here. f is the measurement frequency, and f_0 is the nominal value of frequency. Therefore, t is the clock time corresponding to the given time interval T_0 . Assuming the frequency between each measurement sample is stable, the duration of

each one hundred millisecond is recognized as $(f/60) * 0.1$ seconds for electric clocks. Because the frequency is not constant, the drift is accumulated as time goes by. Setting up a start time as zero drift reference, and an end time as analyzed object, it estimates the time difference between GPS time and the electric clock during the given time period.

7.3.2 Analysis of FDR measurements

Using the frequency measurement at FNET/GridEye, a tool is developed to estimate the time drift from a given time reference at which point the time has zero drift. The time drift analyzer is programmed in C# language in Visual Studio. The GUI is shown in Figure 7-3.

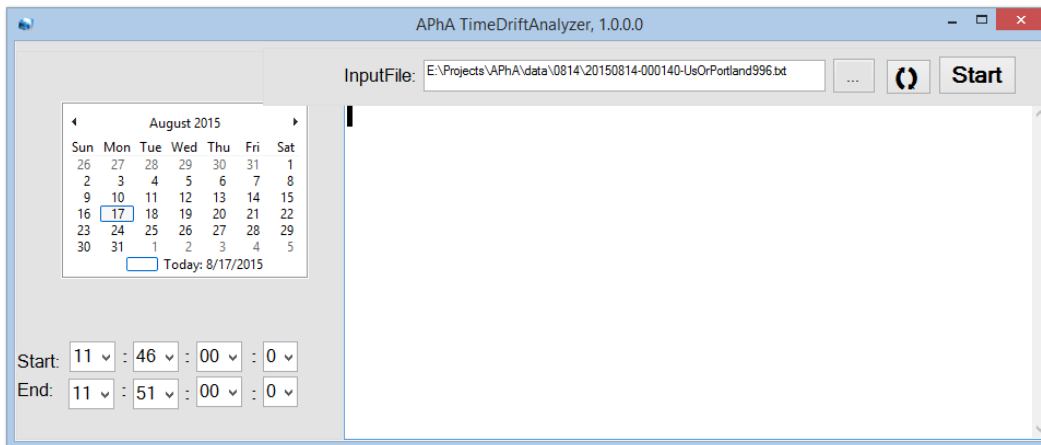


Figure 7-3. Time drift analyzer implementation.



In the form, clients can select the date through the calendar, pick the start time and end time on the left part of the form, then load FDR data file by clicking load button . By clicking "Start" button , the data would be loaded and analyzed. The time drift estimation result of the duration selected by the user would be displayed in the window below the input file dialog.

Figure 7-4 shows an example of time drift estimation. It estimates the time drift from 02:00:00.0 Aug 13 to 12:00:00.0 August 13th. By analyzing the FDRs measurements, the result in the window shows the start time and end time when the drift is up to plus or minus 1 second, and the total drift at the end. In this example, the clock is drifted about 3.127 seconds during the 10 hours.

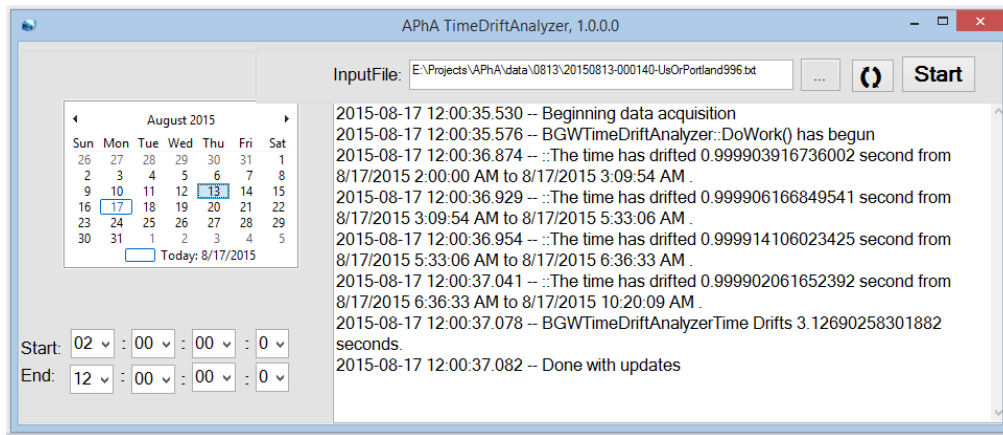


Figure 7-4. Time drift analyzer example.

7.4 Time drift verification

By analyzing the electricity frequency measured by FDR device, the estimation of time drift can be obtained by the tool. It needs solid verification that the drift calculated by the tool is consistent with the true time drift in traffic signal controllers. If the time drift estimation is proved to be close to the real drift, it is believed that the power frequency can be used to estimate time drift in electric clocks, not limited to traffic signals.

According to the National Transportation Communications for Intelligent Transportation System Protocol (NTCIP), the internal information of the traffic signal controller, which is in compliance with the protocol, is able to be queried by successful connection and queries. By

creating a correct Management Information Base (MIB) with a specific object ID for targeting information, the device recognizes the query and replies with corresponding information. Figure 7-5 indicates the connection and communication schematic diagram of the platform in order to export the true electric clocks and their estimates.

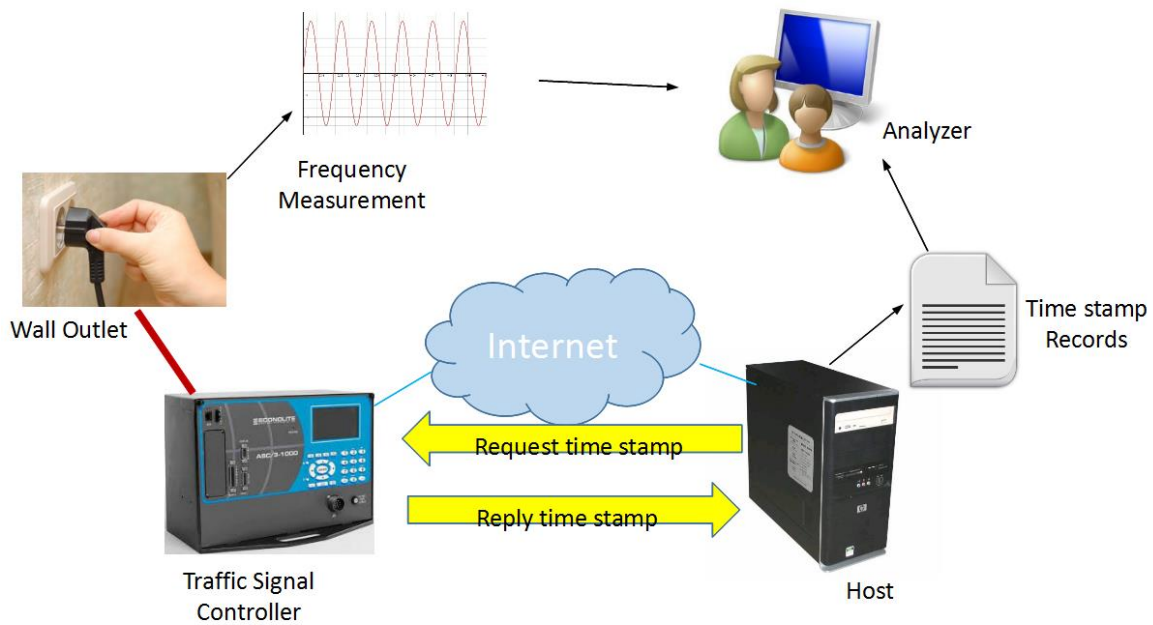


Figure 7-5. Connection and communication schematic diagram.

The traffic signal controller is connected to the host computer. Their communication is established via Ethernet. Firstly the host sends a request to the device querying internal clock time. The device receives the query, returns with the current time of the internal clock. Assuming the communication speed of double directions are identical, the host estimates the local time, which complies with Network Time Protocol (NTP), as the moment the device makes answer counting in the double-directional communication time, Eventually, both the device internal time

and the local host time at the same moment are obtained and recorded in the host. In order to be able to monitor the drift continuously, the request is sent every second.

A tool shown in Figure 7-6 is used to initialize the query and display the query log in the window. By clicking "Start" button, the communication is established, and the host starts to send queries continuously to the controller. The communication log is displayed in the window.

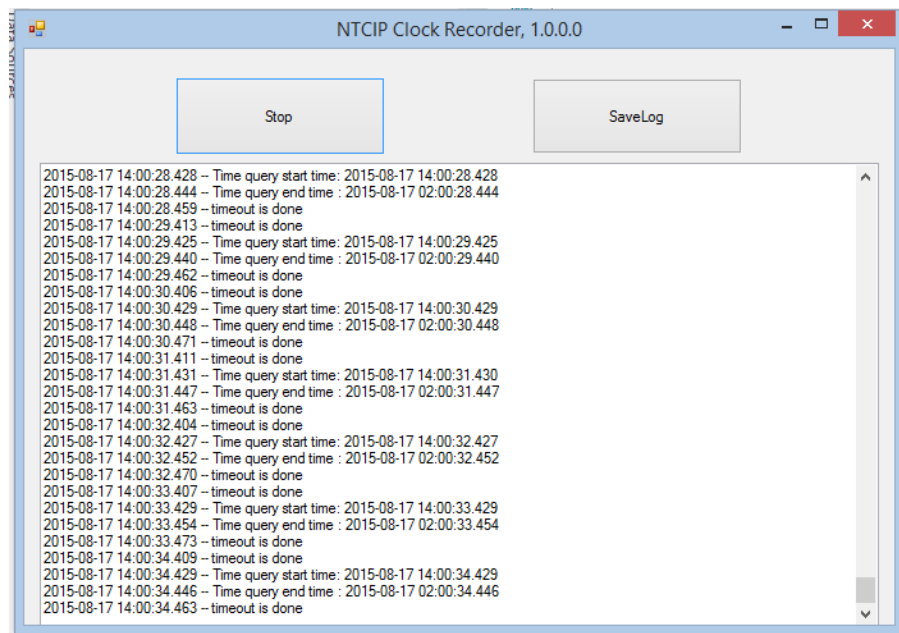


Figure 7-6. Example of implementation of querying device internal clock.

The query result can be exported in a text file, as shown in Figure 7-7. There are two columns in the file. The left column represents the time stamps of the internet clock UTC time. The right column shows the timestamps of the internal clock installed in the controller. It is set up to be local time (PST). Each row stands for the timestamps from different clocks at the same moment. From the query result, it is noticed that the controller's internal clock doesn't have milliseconds, which is consistent with the fundamental that electric clock counts second as discussed.

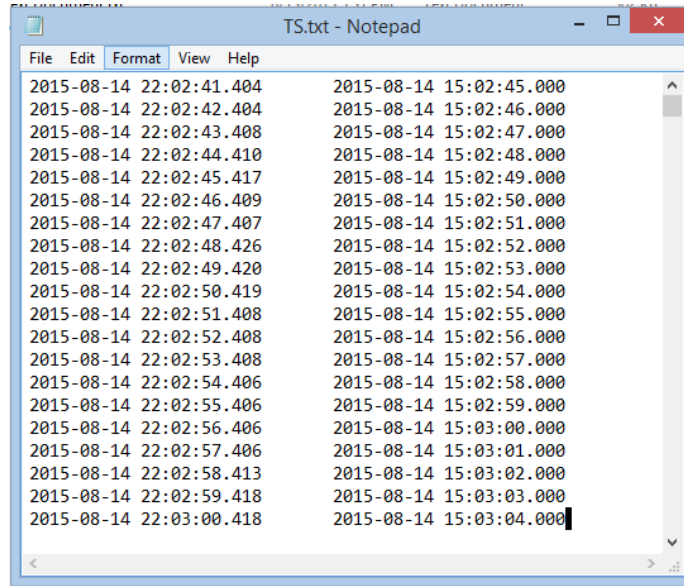


Figure 7-7. Query result example.

Since the timestamps of the local controller clock are considered as the real applied electric clock in the field. The query result can be utilized to verify the time drift estimation proposed. The implementation of the comparison purposes to show the drifts for identical duration simultaneously. An example of the comparison result is shown in Figure 7-8.

In this tool, users can select the start time and end time (UTC time) for comparison. The start time is default as the reference with zero drift. It is designed to load the query result of signal controller time stamp record file by clicking the upper load button and compute the actual time drift by clicking the corresponding start button. For the same time duration, the user needs to load FDR data by clicking the lower load button and compute the estimation by clicking the corresponding start button. As shown in Figure 7-8, when the time duration is set to be from 01:57:02.000 Aug. 14 to 09:02:03.100 Aug. 14, the actual time drift is shown in the right upper window as 8.862 seconds, and the estimation is displayed in the right lower window as 8.061

seconds. The estimation is close to the actual drift read from the local controller with an error less than 1 second.

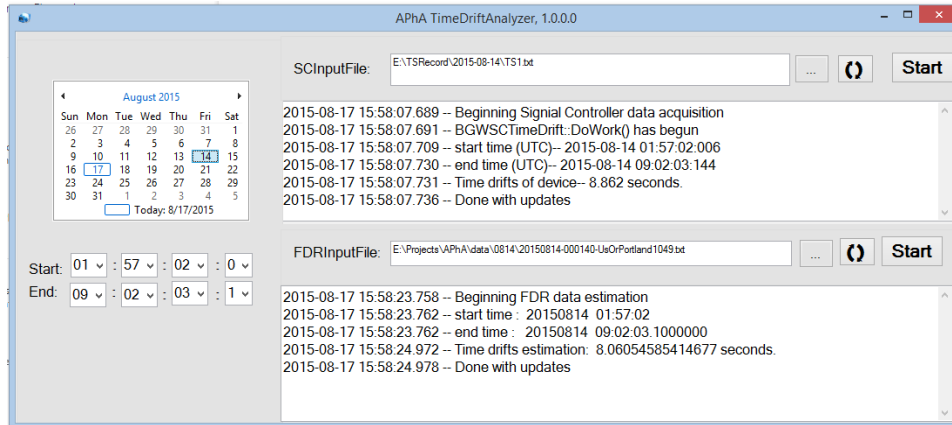


Figure 7-8. Time drift comparison implementation.

The time resolution of FDR is limited to be 100 milliseconds, but the controller time stamp record provides the NTP time at a certain millisecond. It brings in error, slightly. Considering the testing device is installed in Portland, the test uses the data of FDR installed in Oregon.

However, the differences due to FDRs in other locations are unclear for now.

7.5 Experiments

7.5.1 Continuous time drift estimation

In order to continuously observe the electric clocks time drift and validate the capability of estimating time drift of electric clock utilizing power frequency measurement, it is expected to do the estimation continuously for a long duration. The comparison of estimation and measurement of time drift can be done in time-serial to show the error in a certain interval. The same approach above is used to compute the estimation of electric clock time drift caused by power frequency fluctuation, and compare it with the actual drift obtained from a local installed

signal controller. In this application, the start time is set to be the unique zero time drift reference; the end time is set to be the final time expected to observe. Then it is designed to compute the time drifts every 10 minutes till the final end time. Therefore, it is available to see how the time drift changes in the process. This application is implemented in C#. The GUI is designed as shown in Figure 7-9.

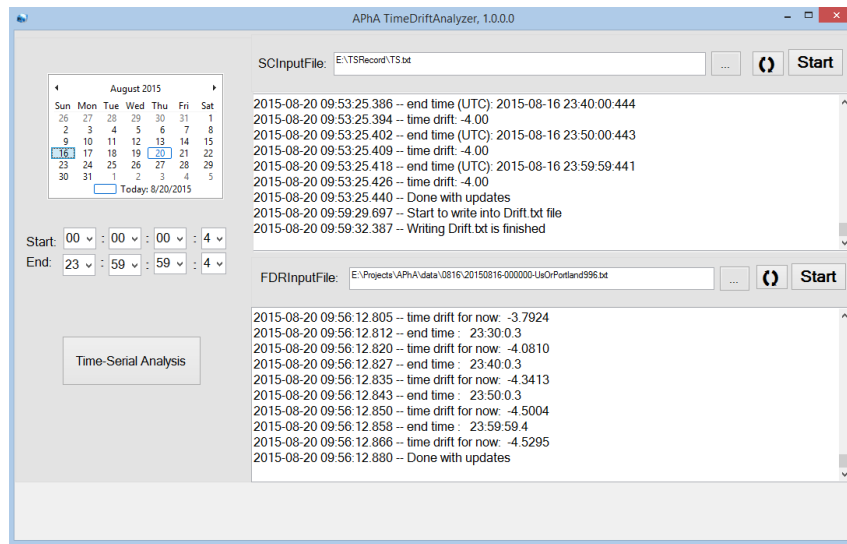
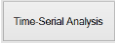


Figure 7-9. Long-term time drift comparison tool.

Compared with Figure 7-8, there is one more button in the lower left area. It is used to combine the time drift results from both estimation and actual measurement record and write the comparison result into a local text file. As an example in Figure 7-9, the time duration is selected from midnight of Aug. 16 to the last second of the day. By loading the recorded time stamps of the internal clock in the signal controller, and then clicking the start button on the top, the real-time drifts of every 10 minutes from the start time will be computed and the result would be shown in the upper window. By loading the measurement of certain FDR (It is selected as the one of the FDRs located in Portland), and then clicking the start button in the middle, the

estimation of time drifts of every 10 minutes from the start time is computed, and the results are shown in the lower window. At the end, the user can click the "Time-Serial Analysis" button as

 The results of both estimation and measurement would be combined and written into a local text file. When the writing process is over, there would be messages displayed in the upper dialog indicating that the process is done. The following Figure 7-10 shows the corresponding content written in a text file.

6:0:0.410	2.0310	1.8700	-0.1610
6:10:0.408	2.0330	1.5690	-0.4640
6:20:0.406	2.0350	1.4220	-0.6130
6:30:0.436	2.0050	1.5410	-0.4640
6:40:0.473	1.9680	1.8010	-0.1670
6:50:0.432	2.0090	1.9080	-0.1010
7:0:0.462	1.9790	1.6300	-0.3490
7:10:0.452	1.9890	1.4160	-0.5730
7:20:0.443	1.9980	1.4560	-0.5420
7:30:0.441	2.0000	1.5370	-0.4630
7:40:0.439	2.0020	1.6810	-0.3210
7:50:0.453	1.9880	1.7900	-0.1980
8:0:0.436	2.0050	1.7780	-0.2270
8:10:0.450	1.9910	1.4920	-0.4990
8:20:0.448	1.9930	1.4580	-0.5350
8:30:0.446	1.9950	1.5610	-0.4340
8:40:0.444	1.9970	1.6800	-0.3170
8:50:0.443	2.9980	1.8860	-1.1120
9:0:0.425	3.0160	2.0690	-0.9470
9:10:0.424	3.0170	2.0760	-0.9410
9:20:0.430	3.0110	2.1510	-0.8600
9:30:0.436	3.0050	2.3210	-0.6840
9:40:0.450	2.9910	2.5030	-0.4880
9:50:0.440	3.0010	2.6330	-0.3680
10:0:0.446	2.9950	2.6860	-0.3090
10:10:0.437	3.0040	2.5800	-0.4240
10:20:0.435	3.0060	2.5500	-0.4560
10:30:0.425	3.0160	2.4260	-0.5900
10:40:0.432	3.0090	2.3710	-0.6380
10:50:0.422	3.0190	2.3090	-0.7100
11:0:0.420	3.0210	2.4330	-0.5880

Figure 7-10. Output of time drift comparison.

There are four columns in the file representing the time stamp, the real-time drift of the internal clock in the signal controller, the corresponding time drift estimation computing based on FDR power frequency measurement, and the difference between the real drift and the estimation respectively. For each row, the time stamp is set as the present end time. The time drift results in the second and third columns are the corresponding drifts from the unique start time (00:00:00.4 am, August 16th in the example shown in Figure 7-9) to the present end time as

indicated in the first column. The result in the last column equals to the measured drift subtracting from estimated drift. It can be easily seen from the last column of this short time analysis that, the errors are mostly within 1 second. However, such a short time performance is not sufficient. Based on this tool, a series of study and testing are conducted in order to verify the performance of different PMUs and long durations.

7.5.2 Comparison of different FDR input signal performances

The time drift estimation based on power grid frequency measurement is demonstrated to be capable of estimating the real-time drift which is collected from a local traffic signal controller. There are multiple FDRs available in a specific power grid. Using different input signals produces different estimation results. Therefore, in this project, it is firstly compared the drift estimation results using different frequency measurement in WECC for the same day (August 19th, 2015 as an example).

The Figure 7-11 shows the estimations of time drifts based on measurements from different FDRs in WECC on Aug. 19. Some of them deviate from the actual drift significantly. On the other hand, different FDRs estimations diverge obviously at the end of the day.

The same result appears on the comparison of the FDRs located in Oregon, as shown in Figure 7-12. There are two FDRs installed in Portland, and one in Eugene. In Figure 7-12, it presents the divergence of time drift estimation based on these three FDRs during the late hours of the day. Moreover, the estimation result from the FDRs installed in Portland performs inferior to that from FDR in Eugene, even though the source of electric clock drift measurement is from a building located in Portland. Therefore, it can conclude that the estimation of time drift from an individual frequency signal is not able to track the drift stably. Same tests on other days, August 20th and August 21st present the similar estimation results.

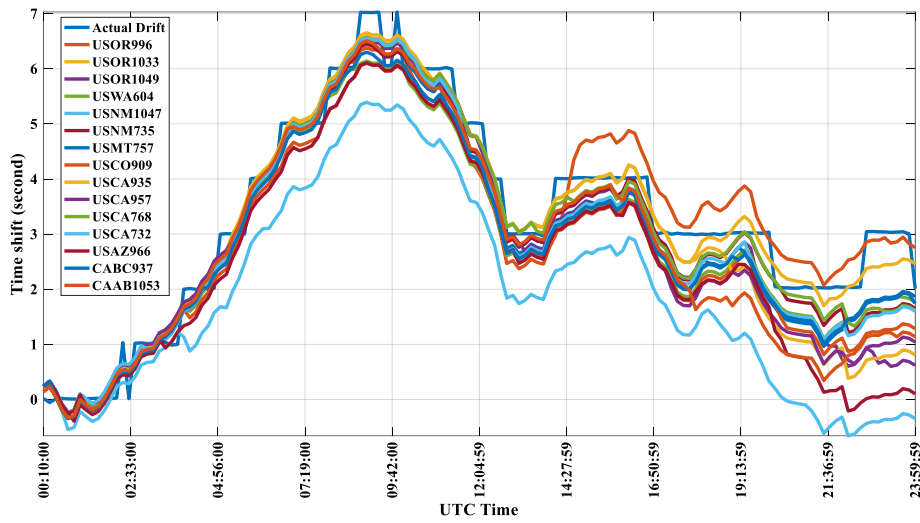


Figure 7-11. Time drift estimations based on FDRs from different states in WECC.

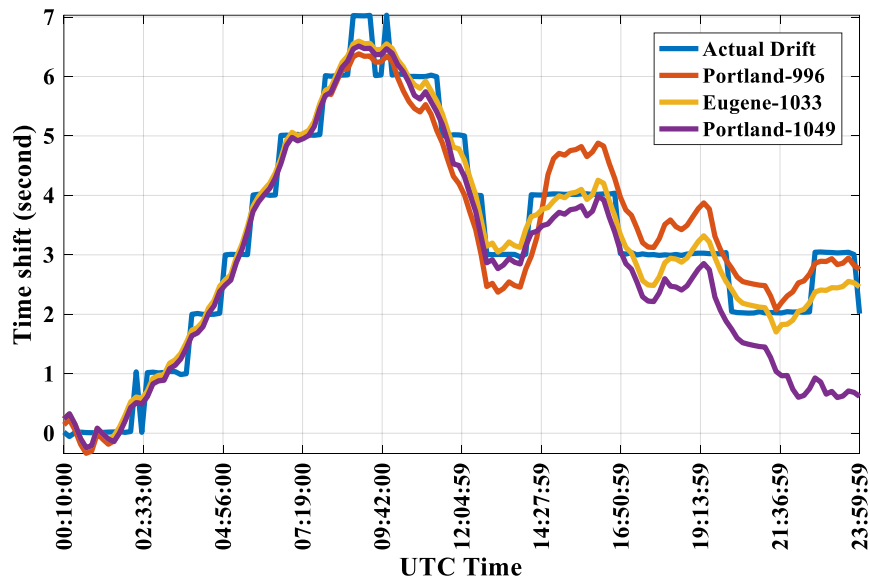


Figure 7-12. Time drift estimations based on FDRs in Oregon.

By combining individual FDRs measurements, we can get the average frequency over the WECC power grid. The estimation of time drift based on the average frequency is compared. The average frequency processing is also applied to the frequency measurement of FDRs located in Oregon. Figure 7-13 presents the corresponding comparison of actual time drift, the estimation by average frequency of all FDRs in WECC and the average frequency of FDRs in Oregon for the same day.

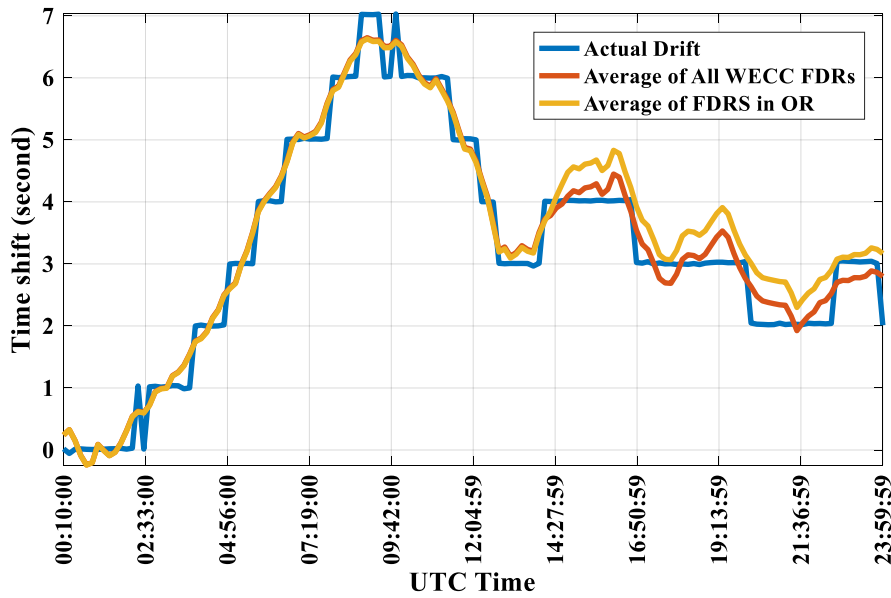


Figure 7-13. Time drift estimation based on average frequency.

In Figure 7-13, it is noticeable that the result matches the actual drift better than the result of individual frequency. The blue stepwise curve is the actual time drift. The others are the estimates using different FDR signals. It can be seen the result of the average frequency of all FDRs installed in WECC is more consistent with the actual drift than the result of the average frequency of FDRs in Oregon. This demonstration is a 24-hour continuous estimation. For those daily self-synchronized controllers, which are set to be self-time-corrected regularly at midnight

or sometime during a day, the performance proves the capability of daily electric clocks time drift estimations within an error less than 1 second.

7.5.3 Long-term performance

This tool is further validated its long-term performance. The reason is many old traffic signal controllers in old cities are not reset regularly. Since the time drift is an accumulative variable, the estimation is required to invulnerable to the accumulative error.

For long duration analysis, there are a few differences from the previous analysis for a single day. First, multiple data files are imported. Because the frequency data of the same day is in an individual text file. Second, the selection date and time of the zero-drift reference, and end time as customer required. It is necessary to clean memory garbage on account of millions of computation, and copy-paste operations.

The analysis platform for long time duration is implemented in C#. The GUI is shown in Figure 7-14. For now, the program is able to successfully process FNET record for continuous days in the same month.

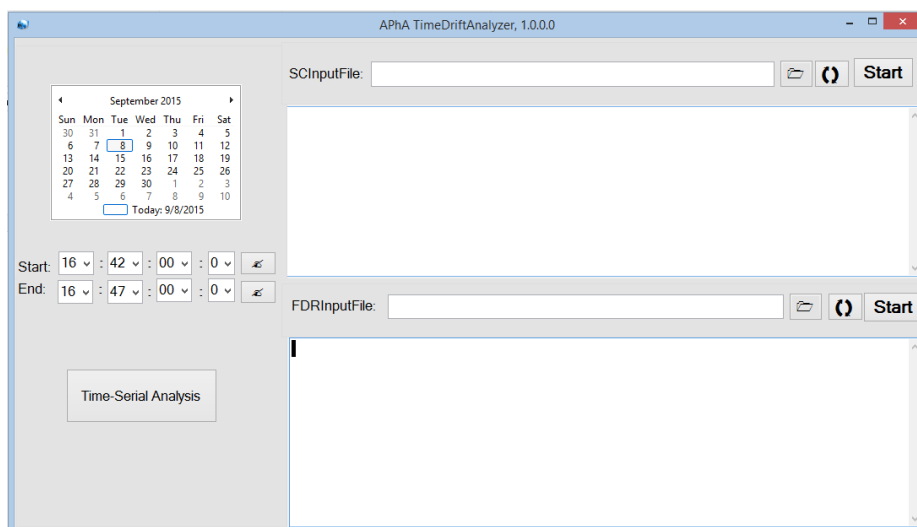



Figure 7-14. Screenshot of time drift analyzer.

From the screenshot, there isn't too much difference compared to the previous analysis interface. Since the main function doesn't change dramatically. The major obstacle is the background computation processing a large amount of data. For the record of frequency, daily data source contains 864,000 pairs of record including frequency and timestamp. Weekly analysis deals with 6,048,000 pairs, and monthly computation constitutes over 25 million records. The code is required to work efficiently for any amount of days' data. There are some modifications on the computation part of the background worker. On the interface, the only difference is the check buttons  beside the start time and end time selection dialogs. Because the analyzed data time duration is expected to span multiple days. Users can choose the date and time of zero-drift reference moment through the calendar, time selection dialogs, then click the check button beside start time. The next step is to choose the end time and confirm it by clicking the check button following the end time.

By accomplishing the tool using C# programming language in Visual Studio, it is able to analyze the time drift from a given start and terminal moment within the same month at 10 minutes interval. Based on the available data record, the time drift from 12:00:00 AM September 1st to 23:59:59 PM September 7th (UTC time) is estimated, and the result is compared with time drift measurement shown in Figure 7-15.

In Figure 7-15, the black stepwise curve is the actual time drift from the controller. The red curve is the estimation of time drift based on frequency measurement from FNET/GridEye. From the long time duration analysis, it is noticeable that the estimation follows the actual time drift well in these continuous multiple days. It doesn't show any increasing error as time goes. The estimation error at every point stays within 1 second.

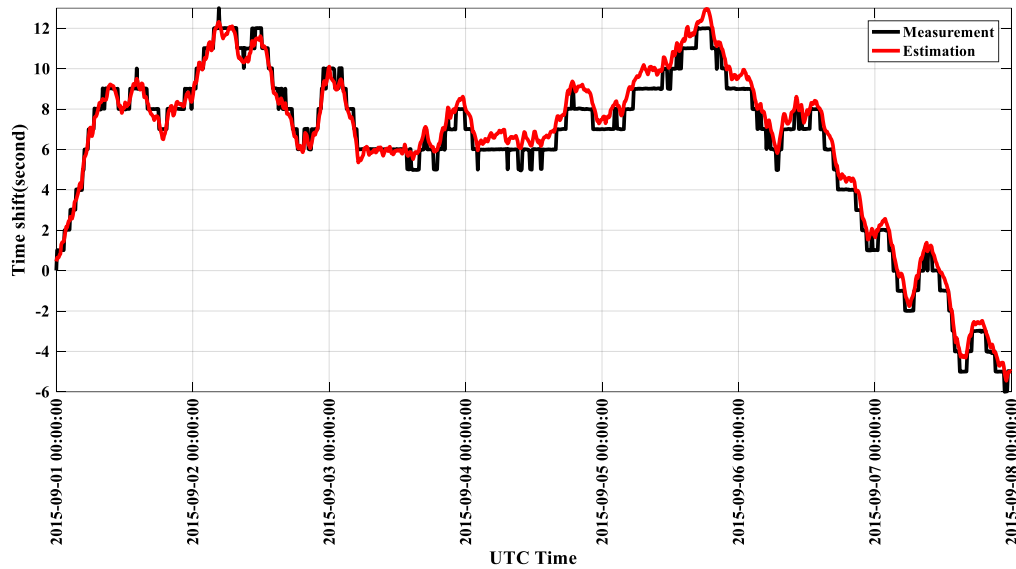


Figure 7-15. 09/01-09/07, 2015 weekly time drift analysis.

7.6 Conclusion

The accuracy of traffic signal prediction plays an essential role in self-driving auto techniques. Even one-second error risks human lives. Because of the economic and popular electric clocks installed in most of the traditional traffic signal controllers, the time shift is ubiquitous in all cities and rural areas. This project discloses the relationship between electricity frequency and electric clock time drift, which is demonstrated to depend on the accumulative frequency deviations from the nominal value. It is validated that the time shift in electric clocks can be effectively estimated using FNET/GridEye frequency measurements. By using the too developed, the estimation error is kept within 1 second.

CHAPTER 8 CONCLUSIONS AND FUTURE WORK

8.1 Conclusions

The dissertation achieves a series of situational awareness application developments and power system disturbance analysis. Especially, this dissertation further explores the potentials of synchrophasor measurements at FNET/GridEye.

A fine-tuned indicator based on the rate of frequency drop during the inertial response is proposed to interpret system low inertia status. Analysis of historical generation trip events in North America illustrates the correlations of ROCOF vs. amount of power loss and the percentage of power loss. It discovers that the same percentage of generation imbalance would influence the ROCOF in different power systems similarly. Inspired by this correlation, higher than expected standard ROCOF can be used as a performance indicator, which is directly associated with low system inertia.

The frequency responses analysis is expanded on bulk power systems over the world. The North American grids analysis demonstrates that in a smaller power grid, the general ROCOFs are more scattered in a larger range with higher median value. Combining the analysis of the historical events in oversea power grids with different capacity sizes, it is disclosed that the median ROCOF is approximately inversely proportional to the grid size. With the understanding of the relation, the general ROCOFs for unobservable power grids can be roughly estimated.

An adaptive approach is proposed here to estimate the magnitude of power imbalance using multiple linear regression methods on the basis of dynamic phasor measurements with improved estimation accuracy. According to the analysis of sufficient actual generation trip disturbances happened in large power systems, it extracts significant variables which are strongly

associated with the magnitude of power imbalance. Eventually, the adaptive estimations are verified to reduce the estimation errors effectively.

Statistical analysis on the inter-area oscillations in EI system is conducted. It discovered significant changes that probably due to network reconstruction or high penetration of renewables took place in EI during 2013. The strong association between the inter-area oscillation and the system load is discovered that the system running with a light load is more vulnerable to inter-area oscillation than under high load conditions. Two most often dominate modes in EI are found around 0.16~0.17Hz and 0.22~0.23 Hz, and they have been gradually increasing in recent years.

The real-time forced oscillation detection approach is demonstrated to be capable of detecting forced oscillations in bulk power systems. It is implemented in openPDC as an individual action adaptor for real-time monitoring the systems and detecting the disturbances.

The application of power system frequency is further explored in traffic light system. It is demonstrated herein this project that the time shift in electric clocks can be emulated using FNET frequency measurements of the power grid. Specifically, in the traffic light system, the time shift depends on the accumulative deviations of the power system frequency from the nominal value. Also, in practice, the discovery would contribute to the accurate prediction of traffic light change.

8.2 Future Work

This dissertation presented some explorations regarding power system synchronous frequency measurements, including several informative data analytics, and promising situational awareness applications. A lot of interesting research can be done in the future.

Based on the frequency measurement, the sustained oscillations are detected. Further research can be conducted to localize the source and test the robustness of the application.

The event detection application for PMU measurements is quite welcomed by utilities. During the future implementation work, it may encounter new challenges and opportunities.

It is discovered in this dissertation that the time drift in electric clocks is associated with the grid frequency, therefore, further investigations should be executed on the time error correction operations in different power grids.

LIST OF REFERENCES

- [1] N. W. Miller, M. Shao, R. D'Aquila, *et. al.* 'Frequency Response of the US Eastern Interconnection Under Conditions of High Wind and Solar Generation'. *2015 Seventh Annual IEEE Green Technologies Conference (GreenTech)*, 2015, pp. 21–28.
- [2] M. Shamirzaee, H. Ayoubzadeh, D. Farokhzad, *et. al.* 'An improved method for estimation of inertia constant of power system based on polynomial approximation'. *Smart Grid Conference (SGC), 2014*, 2014, pp. 1–7.
- [3] P. Kundar, "Power System Stability and Control," The EPRI Power System Engineering Series, McGraw-Hill, 1994. Section 11.1.
- [4] N. W. Miller, M. Shao, S. Venkataraman, *et. al.* 'Frequency response of California and WECC under high wind and solar conditions'. *2012 IEEE Power and Energy Society General Meeting*, 2012, pp. 1–8. P.
- [5] E. Muljadi, V. Gevorgian, M. Singh, *et. al.* 'Understanding inertial and frequency response of wind power plants'. *2012 IEEE Power Electronics and Machines in Wind Applications (PEMWA)*, 2012, pp. 1–8.
- [6] J. D. Lara-Jimenez and J. M. Ramirez. 'Inertial frequency response estimation in a power system with high wind energy penetration'. *PowerTech, 2015 IEEE Eindhoven*, 2015, pp. 1–6.
- [7] I. M. Dudurych, 'Statistical analysis of frequency response of island power system under increasing wind penetration'. *2010 IEEE Power and Energy Society General Meeting*, 2010, pp. 1–6.
- [8] A. Mullane, G. Bryans, and M. O'Malley. 'Kinetic energy and frequency response comparison for renewable generation systems'. *2005 International Conference on Future Power Systems*, 2005, p. 6 pp.-pp.6.
- [9] P. M. Ashton, G. A. Taylor, A. M. Carter, *et. al.* 'Application of phasor measurement units to estimate power system inertial frequency response'. *2013 IEEE Power and Energy Society General Meeting (PES)*, 2013, pp. 1–5.
- [10] S. Sharma, S.-H. Huang, and N. D. R. Sarma. 'System Inertial Frequency Response estimation and impact of renewable resources in ERCOT interconnection'. *2011 IEEE Power and Energy Society General Meeting*, 2011, pp. 1–6.

- [11] D. P. Chassin, Z. Huang, M. K. Donnelly *et. al.* ‘Estimation of WECC system inertia using observed frequency transients’. *IEEE Transactions on Power Systems*, vol. 20, no. 2, pp. 1190–1192, May 2005.
- [12] S. You, D. Zhou, L. Wu, and Y. Liu, Power System Disturbance Location Determination Based on Rate of Change of Frequency. US Patent Application No. 15/353,341.
- [13] Y. Liu, W. Yao, D. Zhou, *et. al.* ‘Recent developments of FNET/GridEye: A situational awareness tool for smart grid’. *CSEE Journal of Power and Energy Systems*, vol. 2, no. 3, pp. 19–27, Sep. 2016.
- [14] Y. Ye and Y. Liu. ‘Monitoring power system disturbances based on distribution-level phasor measurements’. *Proc. of 2012 IEEE PES Innovative Smart Grid Technologies (ISGT)*, pp. 1–8.
- [15] S. You., L. Zhu., Y. Liu, *et. al.* ‘A survey on next-generation power grid data architecture’. *2015 IEEE Power & Energy Society General Meeting*, pp. 1-5. IEEE. 2015.
- [16] L. Wu, Y. Liu, D. Zhou, J. Guo, Y. Liu, “Observation of Inertial Frequency Response of Main Power Grids Worldwide Using FNET/GridEye,” in *2016 IEEE PES General Meeting*, July 17-21, 2016.
- [17] ‘FNET/GridEye Web Display’. <http://fnetpublic.utk.edu/>.
- [18] ‘FNET/GridEye Youtube Channel’.
https://www.youtube.com/channel/UC40n2KTjwRhC9_CvtIasaWA.
- [19] ‘ERSTF Framework Report’
<http://www.nerc.com/comm/Other/essntlrbltysrvdstskfrDL/ERSTF%20%20Framework%20for%20Measures%20Report%20January%202015%20-%20Final.pdf>.
- [20] Kay, S. M. (1993). ‘Fundamentals of Statistical Signal Processing’. Upper Side River, New Jersey: Prentice Hall PTR.
- [21] J. Chai, Y. Liu, J. Guo, *et. al.* ‘Wide-area measurement data analytics using FNET/GridEye: A review’. *2016 Power Systems Computation Conference (PSCC)*, 2016, pp. 1–6.
- [22] ‘Public events confirmed by NERC’
<http://www.nerc.com/comm/OC/Pages/RS/Resources-Subcommittee.aspx>

- [23] Y. Ye, J. Dong, and Y. Liu. ‘Analysis of power system disturbances based on distribution-level phasor measurements’. *2011 IEEE Power and Energy Society General Meeting*, 2011, pp. 1–7.
- [24] C. L. DeMarco, C. A. Baone, Y. Han, B. Lesieutre, “Primary and secondary control for high penetration renewables.” White Paper May 2012, Prepared for the Paper “The Future Grid to Enable Sustainable Energy Systems”.
- [25] NERC, “Frequency Response Initiative Rreport”, Oct.30, 2012.
- [26] ORNL, “Frequency Control Concerns in the North American Electric Power System”, December 2002.
- [27] M. Albu, A.-M. Dumitrescu, and R. Popovici, “Rate of change of frequency-a power quality descriptor,” in *Proc. of 2014 IEEE 16th International Conference on Harmonics and Quality of Power (ICHQP)*, pp. 312–316.
- [28] L. Wu, K. Thomas, R. Orndorff, S. Willis, “Evaluation of openXDA for Automatic Fault Analysis,” *2015 Georgia Tech Fault and Disturbance Analysis Conference*, April 27-28, 2015.
- [29] H. Saadat, “Power System Analysis (3rd Edition)”, McGraw-Hill, 2010
- [30] A. Mullane, G. Bryans, and M. O’Malley, “Kinetic energy and frequency response comparison for renewable generation systems,” in *2005 International Conference on Future Power Systems*, 2005, p. 6 pp.-6.
- [31] M. Swierczynski, D.-I. Stroe, A.-I. Stan, R. Teodorescu, R. Laerke, and P. C. Kjaer, “Field tests experience from 1.6MW/400kWh Li-ion battery energy storage system providing primary frequency regulation service,” in *Innovative Smart Grid Technologies Europe (ISGT EUROPE), 2013 4th IEEE/PES*, 2013, pp. 1–5.
- [32] X. Li *et al.*, “Modeling and control strategy of battery energy storage system for primary frequency regulation,” in *2014 International Conference on Power System Technology (POWERCON)*, 2014, pp. 543–549.
- [33] M. Swierczynski, D. I. Stroe, A. I. Stan, and R. Teodorescu, “Primary frequency regulation with Li-ion battery energy storage system: A case study for Denmark,” in *2013 IEEE ECCE Asia Downunder (ECCE Asia)*, 2013, pp. 487–492.

- [34] S.-C. Wang, S.-C. Lee, Y.-T. Wu, and C.-J. Wu, "Analysis of load characteristics in power systems based on fuzzy modeling," in *2012 Proceedings of SICE Annual Conference (SICE)*, 2012, pp. 1067–1070.
- [35] G. Zheng, Y. Liu, and G. Radman, "Wide area frequency based generation trip event location estimation," in *2012 IEEE Power and Energy Society General Meeting*, 2012, pp. 1–6.
- [36] M. Cheng, J. Wu, S. Galsworthy, N. Jenkins, and W. Hung, "Availability of load to provide frequency response in the Great Britain power system," in *Power Systems Computation Conference (PSCC), 2014*, 2014, pp. 1–7.
- [37] C. Zhao, U. Topcu, N. Li, and S. Low, "Design and Stability of Load-Side Primary Frequency Control in Power Systems," *IEEE Transactions on Automatic Control*, vol. 59, no. 5, pp. 1177–1189, May 2014.
- [38] H. Chen, R. Ye, X. Wang, and R. Lu, "Cooperative Control of Power System Load and Frequency by Using Differential Games," *IEEE Transactions on Control Systems Technology*, vol. 23, no. 3, pp. 882–897, May 2015.
- [39] L. J. Thomas, J. Wu, J. B. Ekanayake, and N. Jenkins, "Enabling distributed frequency response using smart meters," in *2012 3rd IEEE PES International Conference and Exhibition on Innovative Smart Grid Technologies (ISGT Europe)*, 2012, pp. 1–5.
- [40] K. Samarakoon, J. Ekanayake and N. Jenkins, "Investigation of domestic load control to provide primary frequency response using smart meters." *IEEE Transaction Smart Grid*, vol. 3, pp. 282-292, March. 2012.
- [41] C. Zhao, U. Topcu, and S. H. Low, "Frequency-based load control in power systems," in *American Control Conference (ACC), 2012*, 2012, pp. 4423–4430.
- [42] P. Wall, F. Gonzalez-Longatt, and V. Terzija, "Estimation of generator inertia available during a disturbance," in *2012 IEEE Power and Energy Society General Meeting*, 2012, pp. 1–8.
- [43] Theodore Wildi, "Electrical Machines, Drives, and Power Systems (6th Edition)", 2005.
- [44] V. V. Vadlamudi, O. Gjerde, and G. Kjolle, "Dependability and security-based failure considerations in protection system reliability studies," in *Innovative Smart Grid Technologies Europe (ISGT EUROPE), 2013 4th IEEE/PES*, 2013, pp. 1–5.

- [45] Z. Liu, Z. Chen, H. Sun, and Y. Hu, "Multi agent system based process control in wide area protection against cascading events," in *PowerTech (POWERTECH), 2013 IEEE Grenoble*, 2013, pp. 1–6.
- [46] S. You, Y. Liu, L. Wu, D. Zhou, Y. Su, X. Zhang, and Y. Liu, " 'Disturbance Location Determination Based on Electromechanical Wave Propagation in FNET/GridEye -- a Distribution-Level Wide-Area Measurement System'," *IET Generation, Transmission & Distribution*, 2017.
- [47] V. Chuvychin and V. Strelkovs, "Frequency and active power control in islanded power systems based on the magnitude of the disturbance estimation," in *PowerTech, 2009 IEEE Bucharest*, 2009, pp. 1–6.
- [48] S.-J. Lee, "Calculation of optimal generation for system loss minimization using loss sensitivities derived by angle reference transposition," *IEEE Transactions on Power Systems*, vol. 18, no. 3, pp. 1216–1217, Aug. 2003.
- [49] V. V. Terzija, "Adaptive underfrequency load shedding based on the magnitude of the disturbance estimation," *IEEE Transactions on Power Systems*, vol. 21, no. 3, pp. 1260–1266, Aug. 2006.
- [50] L. R. Chang-Chien, L. N. An, and T.-W. Lin, "Demand response plan considering available spinning reserve for system frequency restoration," in *2012 IEEE International Conference on Power System Technology (POWERCON)*, 2012, pp. 1–6.
- [51] C. M. Laffoon and J. F. Calvert, "Abridgment of additional losses of synchronous machines," *Journal of the A.I.E.E.*, vol. 46, no. 6, pp. 573–582, Jun. 1927.
- [52] H.-S. Park and K.-J. Kim, "A study on AGC scheme based on real time frequency characteristics," in *Universities Power Engineering Conference, 2008. UPEC 2008. 43rd International*, 2008, pp. 1–5.
- [53] M. Kayri, I. Kayri, and M. T. Gencoglu, "The performance comparison of Multiple Linear Regression, Random Forest and Artificial Neural Network by using photovoltaic and atmospheric data," in *2017 14th International Conference on Engineering of Modern Electric Systems (EMES)*, 2017, pp. 1–4.
- [54] J. Guo, S. You, C. Huang, H. Liu, D. Zhou, J. Chai, L. Wu, Y. Liu, J. Glass, M. Gardner, C. Black. "An Ensemble Solar Power Output Forecasting Model through Statistical Learning of Historical Weather Dataset", *2016 IEEE PES General Meeting*, July 17-21, 2016.

- [55] D. Huang and W. T. M. Dunsmuir, "Computing joint distributions of 2D moving median filters with applications to detection of edges," *IEEE Transactions on Pattern Analysis and Machine Intelligence*, vol. 20, no. 3, pp. 340–343, Mar. 1998.
- [56] E. Ela, V. Gevorgian, et, "Active power Controls from Wind Power: Bridging the Gaps," NREL, Technical Report, Golden, CO, Jan. 2014, NREL/TP-5D00-60574, [Online]. Available: <http://www.nrel.gov/docs/fy14osti/60574.pdf>.
- [57] Alan Agresti, "An Introduction to Categorical Data Analysis", 2nd edition Wiley, March 2007 [Online]. Available: <https://mregression.files.wordpress.com/2012/08/agresti-introduction-to-categorical-data.pdf>
- [58] R. M. Gardner, Z. Zhong, Y. Liu "Location determination of power system disturbances based on frequency responses of the system", U. S. Patent 7 765 034. July 27, 2010.
- [59] Y. Cui, F. Bai, W. Yao, Y. Liu, L. Wu, Y. Liu, Power Disturbance Localization Based on Hybrid Computational Intelligence Techniques. US Patent Application No. 15/609,861.
- [60] L. Wu, S. Murphy, "Real-time Detection of Power System Transmission Line Switching Operations Based on Synchrophasor Measurements", Submitted for *2018 IEEE PES General Meeting / Conference Exposition*.
- [61] S. You, S. W. Hadley, M. Shankar, and Y. Liu, "Co-optimizing generation and transmission expansion with wind power in large-scale power grids—Implementation in the US Eastern Interconnection," *Electric Power Systems Research*, vol. 133, pp. 209-218, 2016.
- [62] S. Hadley, S. You, M. Shankar, and Y. Liu, "Electric Grid Expansion Planning with High Levels of Variable Generation," *ORNL/TM-2015/515, Oak Ridge National Laboratory*, 2015.
- [63] M. H. Nguyen, T. K. Saha, and M. Eghbal, "Impact of high level of renewable energy penetration on inter-area oscillation," in *Universities Power Engineering Conference (AUPEC), 2011 21st Australasian*, 2011, pp. 1–6.
- [64] R. Elliott, R. Byrne, A. Ellis, and L. Grant, "Impact of increased photovoltaic generation on inter-area oscillations in the Western North American power system," in *2014 IEEE PES General Meeting / Conference Exposition*, 2014, pp. 1–5.
- [65] S. You, J. Guo, G. Kou, Y. Liu, and Y. Liu. "Oscillation mode identification based on wide-area ambient measurements using multivariate empirical mode decomposition." *Electric Power Systems Research*, 134. pp.158-166. 2016.

- [66] S. You, J. Guo, W. Yao, S. Wang, Y. Liu, and Y. Liu. "Ring-down oscillation mode identification using multivariate empirical mode decomposition." In *Proc. 2016 IEEE Power and Energy Society General Meeting*, pp. 1-5. 2016.
- [67] Y. Liu, S. You, and Y. Liu. "Smart Transmission & Wide Area Monitoring System". *Communication, Control and Security for the Smart Grid*. IET.
- [68] Y. Liu, S. You, W. Yao, Y. Cui, L. Wu, D. Zhou, *et al.*, "A Distribution Level Wide Area Monitoring System for the Electric Power Grid - FNET/GridEye," *IEEE Access*, vol. 5, pp. 2329-2338, 2017.
- [69] K. Zhang, Y. Ye, L. Chen, Y. Zhang, R. M. Gardner, and Y. Liu, "FNET observations of low frequency oscillations in the eastern interconnection and their correlation with system events," in *2011 IEEE Power and Energy Society General Meeting*, 2011, pp. 1–8.
- [70] J. Zhao, J. Tan, L. Wu, L. Zhan, W. Yao, Y. Liu, J. Gracia, P. Ewing, "Impact of Measurement Errors on Synchrophasor Applications" . *2017 IEEE PES General Meeting*, July 2017.
- [71] W. Yao, L. Zhan, Y. Liu, M. Till , J. Zhao, L. Wu, Z. Teng, Y. Liu, W. yao. " A Novel Method for Phasor Measurement Unit Sampling Time Error Compensation," in *2017 IEEE PES General Meeting*, 2016, July 16-20, 2017.
- [72] W. Yao, L. Zhan, Y. Liu, M. Till, J. Zhao, L. Wu, Z. Teng, Y. Liu, , "A Novel Method for Phasor Measurement Unit Sampling Time Error Compensation," *IEEE Transactions on Smart Grid*, vol. PP, no. 99, pp. 1–1, 2016.
- [73] S. You, Y. Liu, X. Zhang, Y. Su, L. Wu, Y. Liu, S. Hadley, "Impact of High PV Penetration on U.S. Eastern Interconnection Frequency Response". *2017 IEEE PES General Meeting*, July 2017.
- [74] S. You, L. Zhu, Y. Liu, M. Shankar, R. Robertson, T. King, *et al.*, "Data Architecture for the Next-Generation Power Grid: Concept, Framework, and Use Case," in *Information Science and Control Engineering (ICISCE), 2015 2nd International Conference on*, 2015, pp. 679-682.
- [75] L. Wu, S. You, *et. al.*, "Statistical Analysis of the FNET/GridEye-detected Inter-area Oscillations in Eastern Interconnection (EI)". *2017 IEEE PES General Meeting*, July 2017.

- [76] Y. Cui, L. Wu, W. Yu, Y. Liu, W. Yao, D. Zhou, Y. Liu, "Inter-area Oscillation Statistical Analysis of the U.S. Eastern Interconnection," in *the Journal of Engineering*, 2017, pp:11.
- [77] J. N. Bank, O. A. Omitaomu, S. J. Fernandez, and Y. Liu, "Extraction and visualization of power system interarea oscillatory modes," in *IEEE PES General Meeting*, 2010, pp. 1–7.
- [78] S. You, L. Zhu, Y. Liu, H. Liu, Y. Liu, M. Shankar, *et al.*, "A survey on next-generation power grid data architecture," in *2015 IEEE Power & Energy Society General Meeting*, 2015, pp. 1-5.
- [79] J. K. Wang, R. M. Gardner, and Y. Liu, "Analysis of system oscillations using wide-area measurements," in *2006 IEEE Power Engineering Society General Meeting*, 2006.
- [80] R. M. Gardner, W. Li, J. West, J. Dong, Y. Liu, and G. Zhang, "Power system frequency oscillation characteristics," in *2008 IEEE Power and Energy Society General Meeting - Conversion and Delivery of Electrical Energy in the 21st Century*, 2008, pp. 1–7.
- [81] T. Xia *et al.*, "Phase angle-based power system inter-area oscillation detection and modal analysis," in *European Transactions on Electrical Power*, vol. 21, no. 4, pp. 1629–1639, May 2011.
- [82] Y. Chen, J. Fuller, R. Diao, N. Zhou, Z. Huang, and F. Tuffner, "The influence of topology changes on inter-area oscillation modes and mode shapes," in *2011 IEEE Power and Energy Society General Meeting*, 2011, pp. 1–7.
- [83] C. Gavin, "Seasonal variations in electricity demand," March 2014, [Online]. Available: https://www.gov.uk/government/uploads/system/uploads/attachment_data/file/295225/Seasonal_variations_in_electricity_demand.pdf.
- [84] M. Ghorbaniparvar, "Survey on forced oscillations in power system," *J. Mod. Power Syst. Clean Energy*, vol. 5, no. 5, pp. 671–682, Sep. 2017.
- [85] H. Ye, Y. Liu, P. Zhang, and Z. Du, "Analysis and Detection of Forced Oscillation in Power System," *IEEE Transactions on Power Systems*, vol. PP, no. 99, pp. 1–1, 2016.
- [86] D. Trudnowski, R. Xie, and I. West, "Shape properties of forced oscillations," in *2016 North American Power Symposium (NAPS)*, 2016, pp. 1–5.
- [87] R. Xie and D. Trudnowski, "Distinguishing features of natural and forced oscillations," in *2015 IEEE Power Energy Society General Meeting*, 2015, pp. 1–5.

- [88] L. Vanfretti, S. Bengtsson, V. S. Perić, and J. O. Gjerde, "Effects of forced oscillations in power system damping estimation," in *2012 IEEE International Workshop on Applied Measurements for Power Systems (AMPS) Proceedings*, 2012, pp. 1–6.
- [89] D. Yang, L. Xing, L. Wang, H. Ye, and Y. Liu, "Response analysis and type discrimination of power system forced oscillation," in *2015 5th International Conference on Electric Utility Deregulation and Restructuring and Power Technologies (DRPT)*, 2015, pp. 1346–1350.
- [90] S. A. N. Sarmadi and V. Venkatasubramanian, "Inter-Area Resonance in Power Systems From Forced Oscillations," *IEEE Transactions on Power Systems*, vol. 31, no. 1, pp. 378–386, Jan. 2016.
- [91] J. Follum and J. W. Pierre, "Initial results in the detection and estimation of forced oscillations in power systems," in *North American Power Symposium (NAPS), 2013*, 2013, pp. 1–6.
- [92] L. Kumar, N. Kishor, and Shweta, "Frequency monitoring of forced oscillation in PMU's data from NASPI," in *2016 18th Mediterranean Electrotechnical Conference (MELECON)*, 2016, pp. 1–6.
- [93] N. Zhou, M. Ghorbaniparvar, and S. Akhlaghi, "Locating sources of forced oscillations using transfer functions," in *2017 IEEE Power and Energy Conference at Illinois (PECI)*, 2017, pp. 1–8.
- [94] N. Zhou, "A coherence method for detecting and analyzing oscillations," in *2013 IEEE Power Energy Society General Meeting*, 2013, pp. 1–5.
- [95] S. Maslennikov, B. Wang, Q. Zhang, F. Ma, X. Luo, K. Sun, E. Litvinov. "A test cases library for methods locating the sources of sustained oscillations", *2016 IEEE Power and Energy Society General Meeting (PESGM)*, 2016
- [96] 'Test Cases Library of Power System Sustained Oscillations', [online] Available: [Http://web.eecs.utk.edu/~kaisun/Oscillation/](http://web.eecs.utk.edu/~kaisun/Oscillation/)
- [97] Z. Dao, Y. Liu, and J. Dong. "Frequencybased real-time line trip detection and alarm trigger development", *2014 IEEE PES General Meeting Conference & Exposition*, 2014
- [98] 'Elliott Sound Products Build a Synchronous Clock` [Online]. Available: <http://sound.whsites.net/clocks/sync.html>

- [99] 'Electric Motor', Wikipedia [Online]. Available:
https://en.wikipedia.org/wiki/Synchronous_motor
- [100] Y. Zhang, W. Yao, S. You, W. Yu, L. Wu, Y. Cui, Y. Liu. Impacts of Power Grid Frequency Deviation on Time Error of Synchronous Electric Clock and Worldwide Power System Practices on Time Error Correction. *Energies*. 2017.

VITA

Ling Wu was born in Guizhou, China. She got her B.S. and M.S. degrees in Department of Electrical Engineering from Xi'an Jiaotong University, Xian, China, in 2008 and 2011, respectively. She worked for Shaanxi Power Grid Company, Xian, Shaanxi, China, from 2011 to 2013. Currently, she is working toward her Ph.D. degree in the Department of Electrical Engineering and Computer Science, University of Tennessee, Knoxville, with anticipated graduation in May 2018.

Her research interests include wide-area power system monitoring and dynamics analysis, power system synchrophasors application, and big data analysis for power systems.